UNIVERSITY OF CALIFORNIA
RIVERSIDE

Investigation of Anode Materials for Lithium Ion Batteries

A Dissertation submitted in partial satisfaction
of the requirements for the degree of

Doctor of Philosophy

in

Materials Science and Engineering

by

Lanlan Zhong

March 2016

Dissertation Committee:

Dr. Lorenzo Mangolini, Chairperson
Dr. Juchen Guo
Dr. David Kisailus

The Dissertation of Lanlan Zhong is approved:

_____

_____

_____

Committee Chairperson

University of California, Riverside

ACKNOWLEDGEMENTS

I would like to express my deepest appreciation to my advisor Professor Lorenzo Mangolini for his consistent help and guidance. I appreciate all his contributions of time, innovative ideas and funding during my Ph.D. study. I want to express gratitude to my committee members Professor Juchen Guo and Professor David Kisailus for their valuable advices and the profound discussions upon my dissertation.

Collaboration with Professor Juchen Guo's group is gratefully acknowledged. I would like to express my sincere thanks to Professor Guo for his training on battery fabrication and characterization, and helpful discussions. I am also thankful for him allowing me to use VMP3 potentiostat and probe sonicator in his lab. It was treasured experiences to work with him. I want to thank Professor Guo's students, Chengying Fu, Linxiao Gen and Norm Hart for their generous help. I would also like to thank Professor Valentine Vullev for letting me use Fluorometer, Dr. Bozhilov for helping to train me on SEM and EDS.

In addition, many thanks to my labmates, Tom Lopez, Ozgul Yasar, Patrick Davis, Michael Riekie, Alexis Penaloza, Andi Xie, Vicki Chen, Jesus Hernandez, Tim Kwork, Alejandro Alvarez, Devin Coleman, Stephen Exarhos, Chad Beaudette, for their help in lab and their friendship.

I thank my dear friends Xiao Wang, Lei Guo, Yuanrui Li, Xiaojing Shao for their genius friendship. Thank you all for being there for me when I call you. It doesn't matter where we are in our lives, I know you will always pick up.

Also, I am lucky and grateful to have the love and continuous support from my boyfriend Xuezhi Ma.

At last, I thank my family, especially my mother for her caring and endless love. Her encouragement and love has always been one of my most important driving forces.

COPYRIGHT ACKNOWLEDGEMENTS

ABSTRACT OF THE DISSERTATION

Investigation of Anode Materials for Lithium Ion Batteries

by

Lanlan Zhong

Doctor of Philosophy, Graduate Program in Materials Science and Engineering
University of California, Riverside, March 2016
Dr. Lorenzo Mangolini, Chairperson

Lithium ion batteries, Lithium ion batteries (LIBs) have for several years dominated the market for cell phones, laptops, and several other portable electronic devices. In order to match the necessity of increasing need for higher energy density storage devices, for example, hybrid/electric vehicles. Higher energy density lithium ion batteries have to be investigated. Anode as one of the most important components of in LIBs has been intensively studied in recent years. Silicon, tin and metal oxide etc. based materials are very promising high energy density candidates for anode active materials. Yet, silicon/tin suffer from volume expansion during lithium ions insertion and lead to fast capacity fading upon cycling. This hinders the them from commercialization.

We synthesized and fabricated silicon/tin based nanostructure, and studied their electrochemical performance as anode materials in LIBs. Engineering empty space on the nanometer scale can be one solution for silicon based anode materials. We demonstrate the synthesis of yolk (SiNPs)–shell (NiO) particles using spray-pyrolysis, a technique with proven scalability to industrial production level. After coating and annealing in the presence of polyvinylpyrrolidone, the nickel oxide shell is converted into a porous nickel cage enclosing the silicon particles. The polymer decomposition leads to the formation of an amorphous carbon layer surrounding the nickel cage, the SiNPs-aC-Ni york-shell structure were achieved. This structure maintains a high specific discharge capacity after more than 100 cycles (~ 1400 mAh/g at the 110th cycle with a 0.5 C discharge rate, on a silicon basis) when used as anode for lithium-ion batteries.

Additionally, instead of compositing with carbon, SnNPs was used as conductive materials in silicon based anode materials. The uniformly dispersed tin nanoparticles provide an electronic conductivity in the active materials, which facilitates conduction of electrons in the system. Beside conductive, tin also has a high theoretical energy capacity. Thus, this SiNPs-SnNPs electrode exhibits a stable storage capacity exceeding 1100mAh/g with ~80% first cycle coulombic efficiency. This performance is superior to that of the control samples produced using silicon nanoparticles alone and tin nanoparticles alone.

Furthermore, uniform dispersion of small silicon nanoparticles in electric conductive matrix, which can accommodate silicon volume expansion were fabricated. For the first time, silicon quantum dots synthesized using non-thermal plasma CVD have been utilized as anode materials. SiQDs were successfully synthesized using non-thermal PECVD and surface functionalized. These quantum dots, after specific structure engineering, formed uniform SiQDs-aC agglomerations mixed with carbon nanotubes. This structure has good electrical conductivity and has a carbon-based coating preventing the direct contact between the silicon particles and the electrolyte. This structure maintains a specific charge capacity of approximately 1000 mAh/g^{-1} for 200 cycles and reaches a coulombic efficiency of 99.8%. The proposed process is based on commercially available carbon nanotubes, on silicon quantum dots which are produced using a scalable plasma-enhanced chemical vapor deposition technique, and is compatible with large area coating and processing techniques. The fabrication protocol described in thesis represents a step towards the successful commercial utilization of silicon-based nanomaterials for energy storage applications.

Table of Contents

List of Figures

List of Tables

Chapter 1. Introduction

1.1 Background

There are growing concerns over the environmental and climate impacts caused by using fossil fuels and coals, air pollution and global warming etc. The utilization of renewable energy, solar and wind power, is believed to be one of the most promising solutions. Hence, the need for higher energy density storage device is becoming more and more apparent as the energy demand is increasingly supplied by renewable sources. For instance, in the last decade we have observed a rapid decrease in the cost of electrical power produced using photovoltaic (PV) panels [1], a trend largely induced by the scaling up of production capabilities. As a result, PV-produced electrical power can now compete with grid-supplied energy on a dollar-per-watt basis at peak production conditions. Similar arguments hold for other forms of renewable energy sources, such as wind power [2]. Unfortunately the intermittent nature of this energy sources poses the next roadblock to their large scale utilization. Hence the need to economically viable, safe and reliable energy storage technologies [3].

Another great need for improved storage solutions in the automotive sector. The large-scale utilization of electric vehicle would be highly beneficial from many points of view (reduced dependence on fossil fuels, largely improved air quality in

highly populated areas). For example, if 30% of the vehicles are changed to using green energy, then 22% oil demand in the world can be reduced [4]. At the present, the electrical vehicles have short driving range and high cost prevents them from growing their share of the market. Rechargeable batteries, which are one of the key components in hybrid/electrical vehicles, have drawn enormous attentions. The most common rechargeable batteries are Lead acid batteries, Nickel-cadmium batteries, Nickel-metal-hybride batteries and Lithium-ion batteries. Figure 1.1 depicts the energy density comparison for the four types of rechargeable batteries, and Table 1.1 gives more characteristics of the four types of batteries.

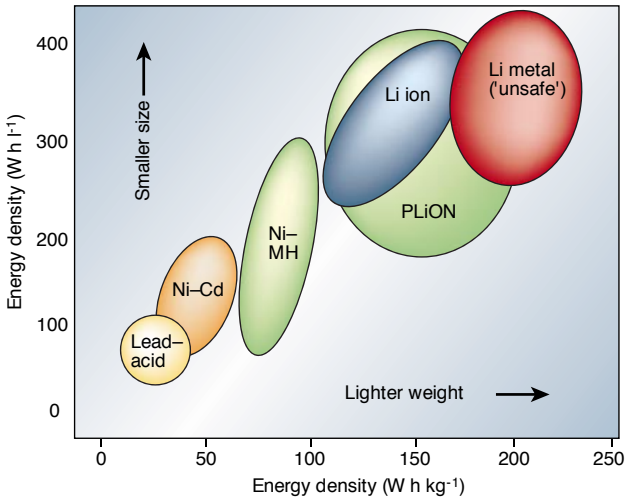

Figure 1.1 diagram of rechargeable batteries gravimetric and volumetric energy density. [5]

Table 1.1 comparison of four types of most common secondary batteries [6]

	Lead Acid	NiCd	NiMH	Li-ion
Toxicity	Very high	Very high	Low	Low
Specific Energy (Wh/kg)	30-50	45-80	60-120	100-250
Cycle life	200-300	1000	300-500	500-1000
Self-discharge/month	5%	20%	30%	<5%
Cell voltage/ Volt	2	1.2	1.2	3.7
Charge time	8-16h	1-2h	2-4	2-4

Among them, lithium ion batteries (LIBs) can play a very significant role. LIBs have been used for portable electronic devices such as cell phone, tablet, PC etc. since the 1990's. Recently LIBs has been started to use for electric vehicle applications. Lithium ion batteries clearly are the primary choice for hybrid/electric vehicles applications due to their higher specific energy, long cycle life, low self-discharge and environmental friendly. Yet, hybrid/electric vehicles require very high energy and low cost to compete with the traditional gas-powered car. Table.1.2 depicts the requirement of batteries energy for hybrid/electric vehicles. The energy density of LIBs has to be increased to ensure long range of the vehicle, and fabrication cost needs to be reduced to increase market penetration. These considerations explain why lithium ion batteries have attracted such interest from many academic and governmental research groups.

Table 1.2 Requirements of batteries' power and energy for hybrid/electric vehicles. [7]

	Hybrid	Plug-in Hybrid	Electric Vehicle
Power	20-60kW	40-80kW	15-150kW
Energy	0.6-1.8kWh	5-15kWh	>15kWh
Cell size	5Ah	20-40Ah	40-66Ah

In this dissertation, we will focus on lithium ion batteries. In the following, we will start introducing the battery in details.

1.2 Lithium Ion Batteries

Figure 1.2 depicts the schematic illustration of a typical lithium ion battery cell. The main components are: anode, cathode, separator and electrolyte. During

charging, lithium ions from the cathode pass through the separator to the anode; for discharging process, lithium ions travel though the separator back to the cathode.

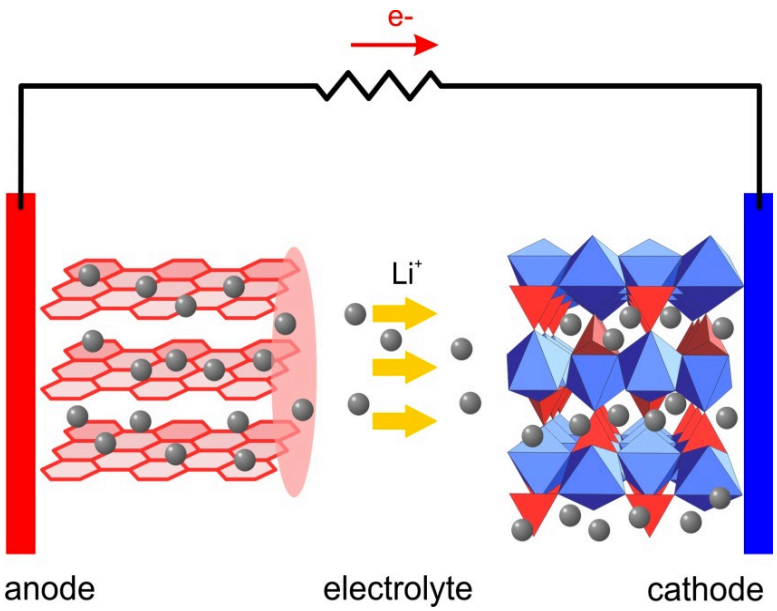

Figure 1.2 Schematic presentation of lithium ion battery (discharge) [8]

The materials used for the anode and cathode can severely affect the battery's performance. The separator is a micro-porous membrane separates the positive and negative electrodes while allowing electrolyte and lithium ions to pass through during charging/discharging. The cathode materials can be categorized by structure. The layered compounds $LiMO_2$ (M=Co, Mn, Ni), the olivine compounds $LiMPO_4$(M=Fe, Mn, Ni, Co) and spinel compounds $LiMn_2O_4$. Graphite, which has a specific capacity of 372mAh/g, is most commonly used for the anode, and $LiCoO_2$, discovered by Goodenough and his coworker [9], is a common commercial cathode material. In this case the cathode and anode reactions are:

Cathode side: $LiCoO_2 \leftrightarrow xLi^+ + xe^- + Li_{1-x}CoO_2$

Anode side: $6C + xLi^+ + xe^- \leftrightarrow Li_xC_6$

All Li ions are in the cathode side initially. The electric energy is stored in the form of electrochemical energy.

1.3 Improving Lithium Ion Battery Energy Density

In order to increase the energy density of lithium ion batteries to match the requirements for applications like hybrid/electric vehicles. The widely used cathode (eg. $LiCoO_2$) and anode (eg. graphite) have to be replaced with higher energy density materials. Thus, developing alternative anode/cathode materials with high energy density have been growing interests. Before we moving to discuss next generation higher energy anode materials, we want to clarify that: currently, the specific energy capacity of LIBs is mainly determined by the cathode materials. In general, the total specific energy capacity of LIBs can be expressed as follow [67]:

$$\textit{Energy of total cell} = \frac{1}{1/C_A + 1/C_C + 1/Q_M} \quad \text{(mAh/g)}$$

Where the C_A and C_C are the theoretical specific capacity of anode and cathode materials, $1/Q_M$ is the specific mass of other cell components (separator, current collectors, case, *etc.*) take Sony18650G8 cell for example, Q_M is ~130.4 mAh/g [67]. Assuming the current cathode materials specific capacity is 140mAh/g or 200mAh/g, by varying anode materials' specific capacity, the overall specific energy of the cell is described in Figure 1.3 [67], where the black dots represents Cc = 140mAh/g, the circle represents Cc = 200mAh/g

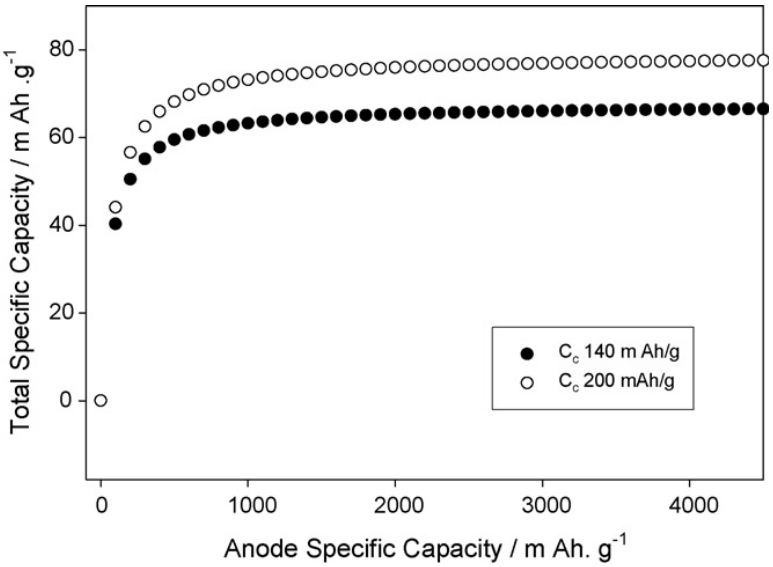

Figure 1.3 Total capacity of 18650 Li-ion cell as a function of anode capacity (C_A). Reprinted with permission from ref [67]. Copyright (2007) Elsevier.

From Figure 1.3, we conclude for given cathode materials, to obtain a noticeable improvement of the total energy capacity, the anode materials has to reach a specific capacity of ~ 1000mAh/g. Once reach that number, the improvement will be minor. There is a huge amount of studying on higher energy cathode material. In this dissertation we will focus on the other important half – anode materials.

1.4 High Energy Density Anode Materials

Graphitic carbon was the first used in commercialized anode material for LIBs and is still dominating the market today. The reasons are: 1) carbon structure is stable upon lithiation/delithiation. They show long cycle life. The reaction between lithium ions and carbon is reversible by forming lithium-carbon intercalation compound. Graphite anode has long cycle life, abundant material

supply and low cost. However, specific capacity of graphite is only 372mAh/g. And graphite anode have safety issues related to lithium deposition [10]. Thus, developing alternative anode materials with high energy density have been a growing interests. There are vast of research about higher energy density anode materials. For instance, the number of publications related to the development of silicon-based anode materials for lithium ion batteries have grown from less than 100 in the year 2000 to almost 700 in the year 2014. The number of related citations has grown almost 200 in the year 2000 to nearly 20,000 in the year 2014 [11]. It is extremely important to review this field and have a clear idea about the issues and possible solutions. Here, we are going to focus on the most promising materials: silicon based anode materials, tin based anode materials and metal oxide anode materials. We focus on the development and design of these materials and structures for use in anodes of lithium-ion batteries.

The next part of the **Chapter 1** is organized as following: in the first section we focus on the use of silicon as anode material. We then focus on tin and on other potential materials such as various metal oxides (tin oxide, titanium dioxide and transition metal oxides). While several other materials have been investigated for as next generation anode materials (metal silicide, alloys in which all components or possibly only one of the components has storage capability, etc.), we choose to focus on the list above since we have found that they have been the focus of the majority of the research efforts in this area. At the end of this chapter we

provide an overall assessment of the field in which we identify the most promising approaches described in the literature, while at the same time identifying the areas which require further investigations.

1.4.1 Silicon

Silicon has been by far the most investigated alternative materials for anode applications in the last few years. Compared to the commercially utilized graphite, for which the intercalation process leads to a capacity of 372 mAh/g, silicon forms a stable alloy with lithium and reaches a gravimetric capacity of 3,579 mAh/g. This is the highest gravimetric capacity among the alternative anode materials [12-14]. The delithiation peak of silicon at ~0.5 V is also relatively low [15], leading to high energy capacity. Moreover, silicon is considered to be environmentally friendly and relatively inexpensive. It is the second most abundant element on Earth after oxygen, eliminating any concern related to manufacturing sustainability. Despite these advantageous properties, there are many problems associated with the use of silicon in lithium ion batteries:

1. Silicon has a low electrical conductivity compared to graphite [13], which implies that it needs to be integrated with conductive additives to provide reasonable functionality.

2. The insertion of lithium ions in the silicon lattice leads to a large volume expansion. The build-up of stress during the lithiation process can lead to the mechanical failure of the silicon structure (see Figure 1.4), resulting in pulverization, loss of electrical contact and irreversible capacity loss [16].

3. The decomposition of the electrolyte on the silicon surface during cycling does not lead to the formation of a stable solid electrolyte interphase (SEI), in contrast to the case of graphite. The ideal SEI layer is permeable to lithium ions and structurally stable.

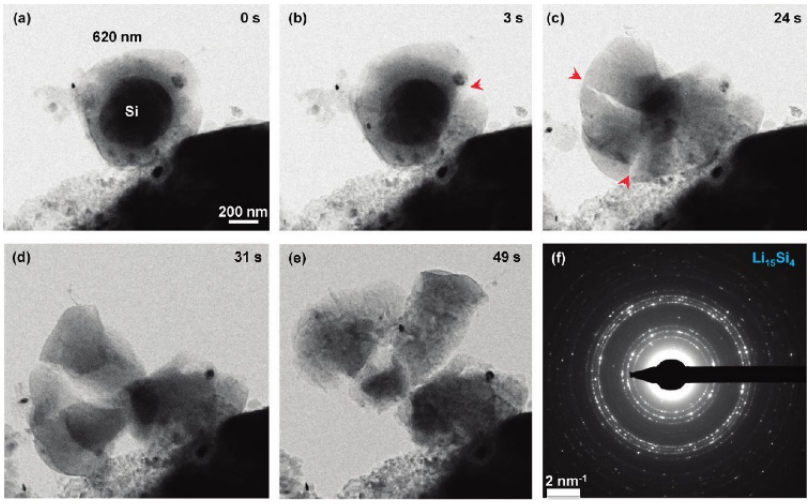

Figure 1.4 In-situ TEM showing the fracture of a free-standing 600 nm SiNP during chemical lithiation over a time length of one minute. (a-e) Time sequence of crack initiation and growth (f) Electron diffraction pattern indicating formation of polycrystalline $Li_{15}Si_4$ as the fully lithiated phase. Reproduced with permission from ref. [16]. Copyright (2012) American Chemical Society.

For the case of silicon, the continuous volume expansion-contraction upon cycling causes new surface to be exposed to the electrolyte, leading to the continuous formation of the SEI. This can also lead to the formation of a thick, poorly conductive SEI layer.

The following strategies, and their combination, have been proposed to overcome these limitations. Reducing the size of the silicon structure to the nanoscale has proven to be effective at accommodating the large volume change and at mitigating, if not completely eliminating, the issue of pulverization during cycling [13-15]. Nanostructuring offers the additional advantage of reducing the lithium ion diffusion lengths, increasing charging and discharging rate [17, 18]. Mixing and composing silicon with conductive additives, in particular carbon-based additives such as carbon black, fibers and nanotubes, can alleviate the issues related to silicon's poor electrical transport properties [19-22] and even accommodate for the large volume change of the active material during cycling [20, 23]. The development of binders specifically designed for silicon has shown great promise [24-28]. Finally, the use of additives such as vinylene carbonate (VC) and fluorethylene carbonate (FEC) leads to the formation of a thinner SEI layer [29-32], alleviating the issue of its stability and poor transport properties when it grows to large thicknesses on the silicon surface. From a material design point of view, it is appropriate in our opinion to categorize the contributions in the area of silicon for anodes according to the geometry of the proposed structure, i.e. nanoparticles (0D), nanowires and nanotubes (1D), and thin films (2D).

1.4.1.1 Silicon Nanoparticles

Reducing particle size increases the surface to volume ratio, releases the stress build-up during lithiation, and effectively prevents the pulverization of the active material during cycling. From a thermodynamic point of view, fracturing involves the formation of new free energy as a path to release strain energy (Griffith criterion). This process becomes less favorable if the surface to volume ratio is already high. For the case of silicon in lithium-ion batteries, several reports have provided convincing evidence that the use of nanoparticles can stabilize the anode structure and improve cycling stability. Huang et al. [16] performed in-situ TEM lithiation studies and showed that silicon particles below 150 nm in diameter undergo lithiation without crack formation. Similar findings have been reported by other groups as well [33, 34]. As an additional benefit, a reduction in silicon diameter shortens the lithium ion diffusion length and increases the diffusion rate [15], allowing for faster charging and discharging in a full cell.

The utilization of silicon nanoparticles (SiNPs) as the electrochemically active component of an anode presents many challenges. First of all, it is not trivial to ensure good electrical conductivity through a network of small particles. Moreover, any contact with the current-carrying component of the anode must be sufficiently robust to survive the lithiation-delithiation cycle. While the reduction in size prevents cracking and pulverization, it does not prevent the volume expansion and the continuous breaking-and-reforming of the SEI layer [35, 36].

This process leads to low coulombic efficiency and poor cycle stability. High specific surface area of any nanoparticle-based anode also leads to high capacity loss on the first cycle, when significant SEI formation occurs.

A large number of silicon-carbon heterostructures have been proposed with the goal of realizing an optimal nanoparticle-based anode [22, 37-51]. Carbon in its many forms, such as graphite, graphene, nanotubes and as amorphous layer, has good electrical conductivity and excellent compatibility with the lithium-ion chemistry. Carbon is lightweight and abundant. Lee et al. [47] embedded <30 nm silicon nanoparticles in graphene oxide sheets by mixing the two components in solution followed by filtering and thermal annealing. The resulting electrode, shown in Figure 1.5, exhibited a storage capacity exceeding 2,200 mAh/g after 50 cycles and exceeding 1,500 mAh/g after 200 cycles. While a clear improvement compared to the pure silicon nanoparticle case was demonstrated, the decay in capacity was noticeable. Similar studies [45-47, 49, 52] attribute the capacity fading to particle agglomeration which prevents the direct contact between each nanoparticle and the graphene support. The lack of good electrical contact renders a significant fraction of the material inactive.

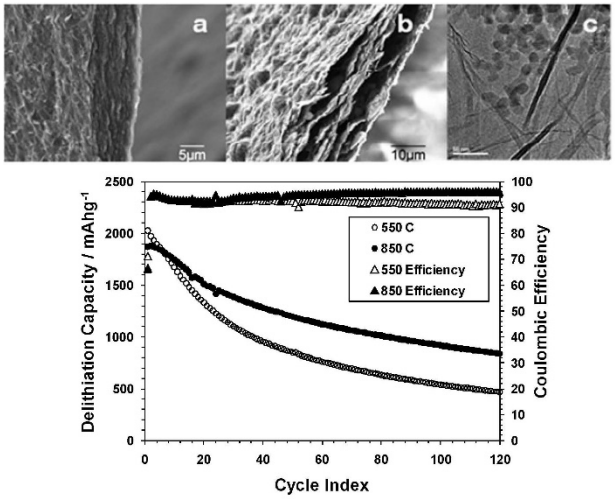

Figure 1.5 (Upper) edge view SEM images of, (a) Silicon graphene oxide paper; (b) silicon graphene (SG) paper; (c) TEM image of SG paper, (bottom) delithiation capacitiesand coulombic efficiencies of SG samples reduced at 550 or 850 °C. Reproduced with permission from ref. [47]. Copyright (2010) Royal Society of Chemistry.

Other strategies have been proposed to create a direct and robust bond between silicon nanoparticles and the conductive material [46, 48, 53, 54]. Martin et al. [53] developed a wet-chemistry protocol to achieve a molecular link between silicon nanoparticles and multi-walled carbon nanotubes (MWCNTs). The process is based on the functionalization of the MWCNT surface with aminophenyl groups, followed by reaction with silicon particles. The resulting electrode was stable for 30 cycles with a capacity of 1,000 mAh/g, roughly a factor of two higher compared to the control structure based on the simple mixing of silicon particles and nanotubes. Gohier et al. [55] used chemical vapor deposition to decorate vertically aligned carbon nanotubes with silicon particles. This approach allows achieving the direct binding of silicon to the nanotube backbone, which is expected to be a nearly ideal bond with respect of electrical

conductivity and mechanical stability. The resulting electrode maintained a capacity of 1,000 mAh/g after 100 cycles at a 10C discharge rate.

Several approaches are available to create a stable contact between silicon nanoparticles and the current-carrying additive, but the reports listed above do not address the formation of an unstable SEI layer onto the silicon surfaces. It is therefore important to control the nature of the interface between the silicon particles and the electrolyte. Coating of the silicon surface with carbon-based layers has been achieved via chemical vapor deposition [13], using wet-chemistry techniques [54] or by embedding silicon particles in electro-spun carbon fibers [56-59]. Guo et al. [60] achieved a uniform dispersion of silicon particles in a carbon matrix via surface-initiated polymerization method. The polyacrylonitrile (PAN) coating was then converted to amorphous carbon after thermal annealing. The weight loading of the prepared electrode was in the 0.85÷1.1 mg/cm2 range. This structure showed a capacity of ~1,000 mAh/g for 120 cycles at a 200 mA/g discharge rate. Promising results were also reported by Jeong et al. [61] for a similar structure and processing protocol, confirming that embedding silicon particles in a carbon matrix is a promising approach. Jung et al. [62] also demonstrated that embedding silicon particles in a porous carbon matrix can lead to the synthesis of a promising structure. Porosity in the carbon matrix was achieved by adding silica particles to the precursor mixture, which was then spray-dried and further processed with hydrofluoric acid to remove the

silica nanoparticles from the resulting micron-sized particle. The fact that such structure can be achieved using spray pyrolisis is promising from the scale-up point of view.

Another report worth discussing in greater details is the one from Yang et al. [63], who use spray pyrolisis to form large (few hundreds of nm) particles showing a very uniform mixture of silicon and carbon. This was done by pyrolising dimethyldivinylsilane at 900°C through a tube furnace. The resulting material is amorphous and it is impossible to spatially distinguish silicon domains in the carbon matrix. This material maintains a capacity of ~1000 mAh/g for 160 cycles.

Magasinski et al. [13] reported the growth of silicon nanoparticles on a 3D micro-porous carbon sponge via chemical vapor deposition, followed by an additional CVD carbon coating step using propene as precursor. The structured exhibited a ~1,500 mAh/g capacity at 1C for more than 100 cycles. This report is interesting because it shows that it is also beneficial to engineer a structure that can accommodate for the large volume expansion of silicon during cycling. While embedding silicon particles within a carbon matrix is beneficial with respect of the device robustness, it does not seem to be sufficient to achieve the thousands-cycle stability needed in real-life applications. Engineering a buffer-space between the silicon and the surrounding carbon matrix is important to improve device performance, as confirmed by several reports. Liu et al. [23] have realized

yolk-shell silicon-carbon particles by a multi-step process which involved the coating of the silicon core with an oxide shell, its subsequent coating with an additional carbon layer, and treatment with hydrofluoric acid to remove the oxide buffer layer. Half-cells based on this particles achieved 1,500 mAh/g for 1000 cycles with coulombic efficiency exceeding 99%.

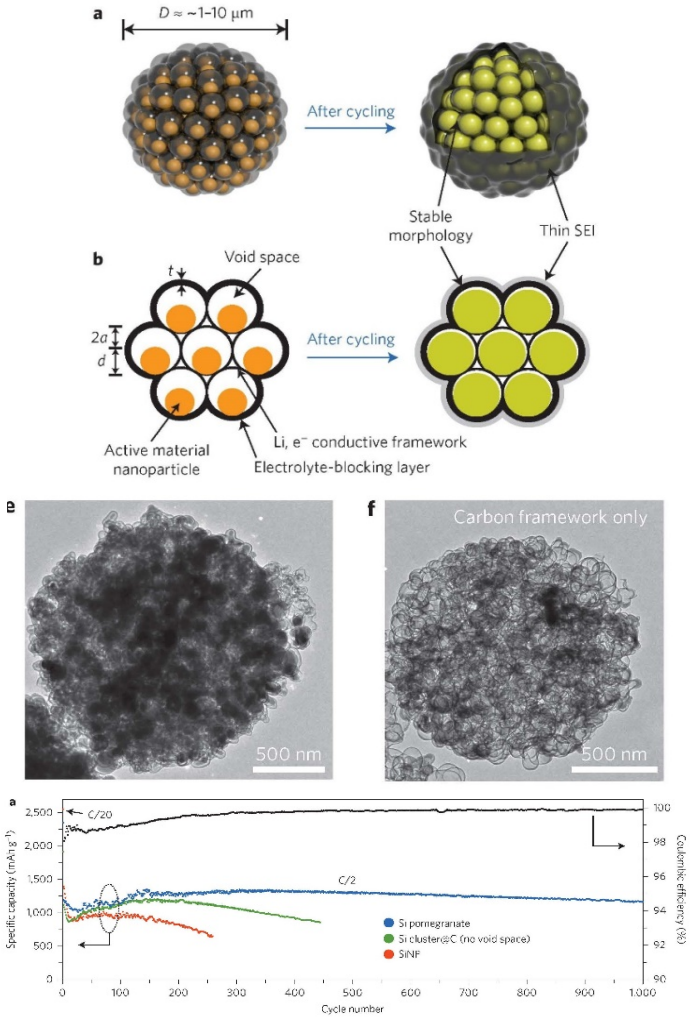

Figure 1.6 (a) the three dimensional view and (b) simplified two-dimensional cross-section view of one pomegranate microparticle before and after electrochemical cycling. (e) TEM image of one silicon pomegranate particle, (f) carbon framework after etching silicon away using NaOH. (Bottom) reversible delithiation capacity for the first 1000 galvanostatic cycles of the silicon pomegranate and other structures testing under the same conditions, coulombic efficiency was plotted for silicon pomegranate only. Reproduced with permission from ref. [64]. Copyright (2014) Nature publishing group.

In a follow-up contribution, Liu et al. [64] showed that by controlling the degree of agglomeration of the yolk-shell nanoparticles it is possible to reduce the specific surface area of the active material. An agglomerate of yolk-shell particles with a 100 nm diameter results in a ~2 μm “pomegranate” structure, see Figure 1.6. The resulting anode achieved a 1,000 mAh/g capacity for 1000 cycles with a 0.2 mg/cm^2 loading. More recently Lu et al. [65] have proposed another approach to engineering an empty buffer volume around silicon particles with the goal of accommodating for their expansion during lithiation. In this report, a connected framework of silicon nanoparticles were produced via thermal reduction of SiO powders in presence of a resorcinol. After reduction, micron-sized agglomerates of nanoparticles wrapped in an outer carbon shell were obtained. This synthesis route is simpler than that described by Liu and coworkers [23] and the resulting battery maintains a capacity of ~1,500 mAh/g for 1000 cycles when the weight loading is ~0.4 mg/cm2. The authors also reported that the same material allows for stable operation for up to 100 cycles when the weight loading was increased to 2 mg/cm2, corresponding to an areal capacity of almost 3 mAh/cm^2.

The development of binders specifically designed for silicon has also been the subject of important investigations. A porous sodium carboxymethyl cellulose (CMS) binder was proposed by Guo and Wang [24]. Self-healing polymers [25] and alginate [27] were also tested as binder. For the case of alginate, Kovolenko

et al. [27] measured a stable capacity of 1200 mAh/g for 1300 cycle for an electrode with a 3:1 silicon-to-carbon weight ratio (the weight loading was not specified). Liu et al. [43] developed a polypyrrole-based conducting polymer, which when mixed with silicon nanoparticles and carbon nanotubes enabled the fabrication of an anode which showed ~1,600 mAh/g capacity after 1000 cycles (weight loading 0.3-0.5 mg/cm2). More recently, Park et al. [66] produced and tested a conducting polymer named poly(1-pyrenemethyl methacrylate) (PPy) in combination with ~100 nm silicon nanoparticles. The electrode retained a 1,500 mAh/g after 1000 cycles with a silicon-to-polymer weight ratio of 2:1 and a total weight loading of 0.24 mg/cm2. The good performance was also attributed to the fact that the coverage of the silicon surface by PPy stabilized the SEI layer while providing electron and ion conductivity.

To summarize, the use of silicon nanoparticles alone is not sufficient at realizing an anode with satisfactory cycling stability. A careful design of the material structure and composition is necessary to obtain a good performance, especially with respect of binding silicon to a current-carrying additive (typically carbon based), and with respect of engineering a buffer volume to accommodate for the silicon expansion during cycling. Recent progress on new generation binders also shows great promise, and their use in combination with nanostructured silicon may push a silicon-based anode closer to the market.

1.4.1.2 Silicon Nanowires

The group of Yi Cui pioneered the investigations on the electrochemical properties of 1-D silicon nanostructures, i.e. nanowires. Chan et al. [7] described a template-free technique for the growth vapor-liquid-solid (VLS) growth of nanowires on a stainless steel substrate. The resulting electrode achieved a 4200 mAh/g first cycle capacity and a 3,500 mAh/g capacity after 20 cycles at 0.2C discharging rate. It should be noted that the first cycle coulombic efficiency was 73%, which is higher than what is typically reported for silicon nanoparticle – based electrodes [67]. In-situ TEM characterization confirmed the crystalline-to-amorphous transition after the first cycle [7]. This report clearly suggested that 1-D structures are promising candidates for the development of next-generation anodes for batteries. In particular, nanowires directly grown onto the desired substrate have (a) good electrical contact with the current collector, (b) can accommodate the large volume changes upon lithiation/delithiation because of their reduced size (similarly to the nanoparticle case) and (c) allow for fast lithium ion diffusion because of the high surface-to-volume ratio. Silicon nanowires also proved to be ideal structures for performing in-situ studies and for advancing the understanding of the lithiation process in silicon. Lee et al. [68] demonstrated that the lithiation of silicon nanowires is not isotropic (see figure 1.7), since lithium diffusion is faster in the <110> direction due to the lower silicon density in that direction.

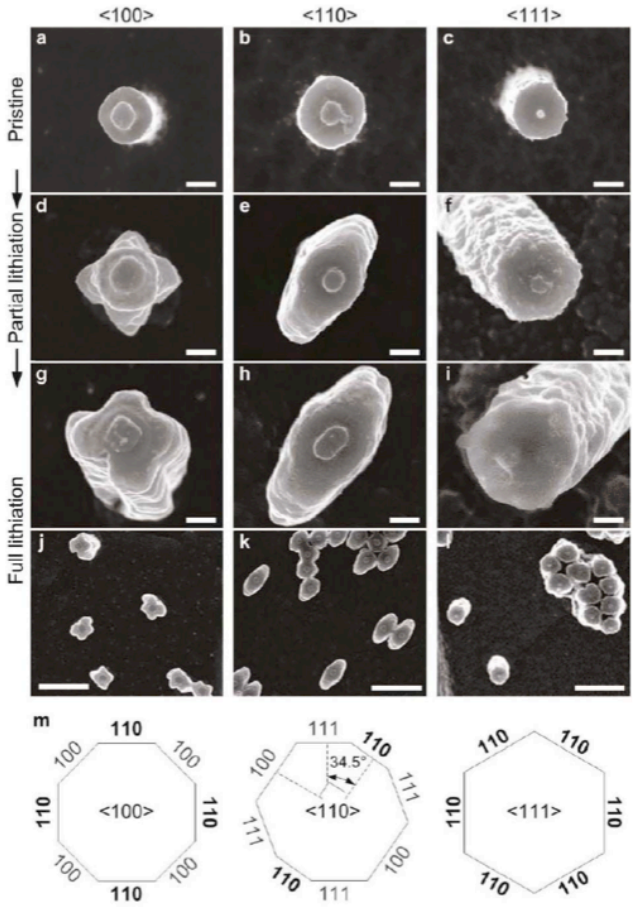

Figure 1.7 Anisotropic lateral expansion of crystalline Si nanopillars with three different axial orientations (<100>, <110> and <111>) upon lithiation. (a-l) Top-view SEM images of Si nanopillars of each crystal orientation and each lithiation state. The <100> axially oriented pillars are shown in the left column, <110> pillars are shown in the middle column, and <111> pillars are shown in the right column. The top row shows pristine pillars, the second row shows partially lithiated pillars held at 120 mV vs Li/Li^+, and the third row shows fully lithiated pillars held a 10 mV vs Li/Li^+. The images in the 4^{th} row show low-magnification views of fully lithiated pillars of each axial orientation. Scale bars from (a-i) are 200 nm and from (j-l) are 2 μm. (m) Schematic diagram of the crystallographic orientation of the facets on the sidewalls of each of the pillars. Lithiated silicon primarily expands along the <110> direction perpendicular to the nanopillar axis. Reproduced with permission from ref. [68]. Copyright (2011) American Chemical Society.

Following research on silicon nanowires focused on addressing the rapid capacity fading observed in anodes based on them. Fading is mainly due to increasing electron resistivity upon cycling [14], likely due to structural failure and breakage, and roughening of the surface during cycling which leads to significant

SEI formation and other irreversible reactions [69]. Coating with a carbon layer has beneficial effects, similarly to what is observed for the case of nanoparticles. Bogart et al. [70] demonstrated that carbon coating on SiNWs enhances the lithiation rate by about one order of magnitude while at the same time offering a clamping effect which prevents fracturing and improves stability. Huang et al. [71] fabricated carbon-coated SiNWs and observed a clear improved compared to the pristine control structure. The reported a first discharge capacity of ~3,300 mAh/g with a first cycle coulombic efficiency of 84%. TEM analysis of their structure confirmed that the nanowires remain continuous after lithiation-delithiation. Cho et al. [72] protected the silicon nanowires with a nitrogen-doped amorphous carbon layer grown by CVD (see Figure 1.8). They reported that an increase in the thickness of the graphitic layer from 20 nm to 50 nm lead to an increase in charge capacity from 800 to 1,000 mAh/g after 45 cycles. Zhu et al. [54] presented a unique strategy for fabricating graphene-wrapped silicon nanowires. The wires were first terminated with amino groups via functionalization with 3-aminopropyl-triethoxysilane. The functionalized nanowires were then wrapped in graphene oxide sheets by simply mixing them with a graphene oxide solution in water. Annealing at 950°C resulted in the formation of graphene-coated nanowires. The authors observed a capacity of ~1,300 mAh/g after 80 cycles with an initial coulombic efficiency of 80%, a significant improvement in device stability compared to the control, uncoated nanowires. They attributed the improvement to the high electron conductivity of the composite.

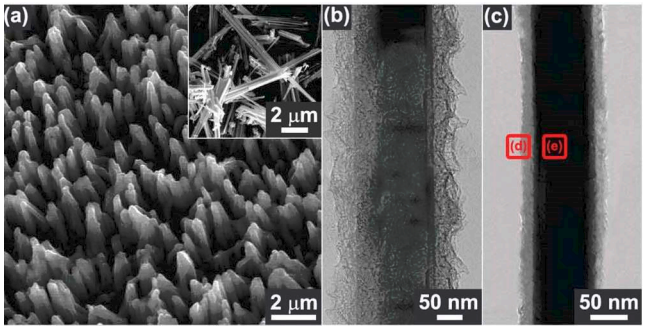

Figure 1.8 (a) SEM micrograph of the vertically aligned Si-C NW array synthesized on the Si substrates. The inset corresponds to the Si-C NWs separated from the substrates. HRTEM images showing Si-C NWs with (b) 50 and (c) 20 nm-thick shells. Reproduced with permission from ref. [72]. Copyright (2011) American Chemical Society.

Other groups tested alternative approaches with the goal of stabilizing the performance of 1-D silicon nanostructures. For instance, silicon nanotubes are potentially capable of accommodating the large volume expansion of the material during cycling [73, 74]. Song et al. [74] realized silicon nanotubes by first growing a zinc oxide nanowire array on a stainless steel substrate followed by CVD of silicon and selective etching of the zinc oxide template. This structure exhibited a capacity of more than 2,000 mAh/g for 50 cycles with a maximum coulombic efficiency of 90.5% at 0.2C cycling rate. Wu and coworkers [73] designed a double-walled Si-SiOx nanotube in which the SiOx protective layer allows for lithium ion diffusion while preventing outer expansion of the silicon core. They measured a capacity of 600 mAh/g for 6,000 cycles at a 12C rate.

Despite these excellent contributions, in the authors' opinion there are critical problems associated with the use of nanowire. First of all the typical loading weight for the nanowire-based structures listed above are generally low, such as 0.1-0.2 mg/cm2 [73], thus limiting the energy density achievable with such

structures (a commonly referred to value of volumetric capacity that is required for commercial applications is 2 mAh/cm^2 [75]). Moreover, large-scale and cost-effective synthesis techniques are needed to make the material compatible with commercial applications. This is a significant challenge for nanowire-based technologies, although promising reports can be found on the scalable production of silicon nanowires. Chan et al. [76] describe the growth of silicon nanowires via a supercritical solution-liquid-solid (SLS) which is capable of producing >45 mg/hour at the lab scale.

1.4.1.3 Silicon Thin Films

The first studies on the application of silicon in electrochemical energy storage were actually conducted using thin films grown onto conductive substrates using standard deposition techniques, such as sputtering, evaporation or chemical vapor deposition [77, 78]. Chen et al. [78] deposited thin amorphous silicon films on a rough copper substrate via sputtering and reported a capacity of ~1250 mAh/g for 500 cycles at a 0.5C discharge rate. They found that thermal annealing of the film after deposition led to an improvement in stability, likely because of the improved adhesion of silicon with the substrate. Kim and coworkers [77] fabricated silicon films on an iron substrate and observed a >3,000 mAh/g capacity for 300 cycles. The good performance is attributed to (a) a good adhesion between the silicon film and the current collector, which ensures

good electrical conductivity, (b) the absence of binders and other additives which reduce the effective weight loading and (c) the low thickness of the silicon films, which alleviates the problems associated with the silicon expansion. However, there are clear limitations to this technology when thicker films are targeted. It is reasonable to expect that thicker films may have limited performance because of the material poor electrical conductivity, because of the long lithium ion diffusion length, and because of their reduced mechanical stability. Maranchi et al. [155] found that 250 nm thick have stable capacities for 30 cycles, while 1000 nm thick films show dramatic decay in capacity after only 12 cycles. Analysis of these films confirms that severe cracking is present even for thin films, as shown in Figure 1.9.

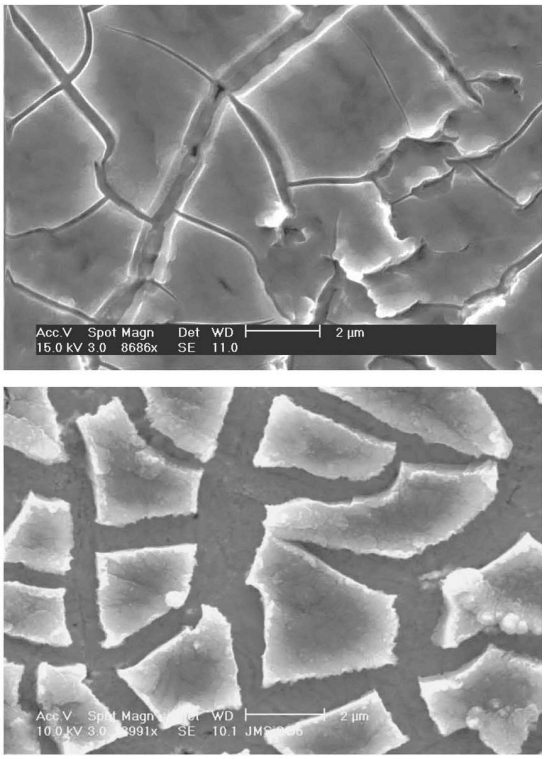

Figure 1.9 Plan-view SEM micrograph of 250 nm Si film cycled at ~ C/2.5 for (a) 1 cycle and (b) 30 cycles. Reprinted with permission from ref [155]. Copyright (2006) Electrochemical Society.

Few attempts have been made to improve the performance and stability of thin-film based silicon anodes [79-81]. Zhang et al. [81] developed a nanostructured substrate with nickel nanocones. After sputtering of the silicon layer, the structure showed a 2200 mAh/g capacity for 100 cycles at 0.2C rate. Arie et al. [82] investigated the role of doping onto the performance of silicon thin films. They found that n-type doping with phosphorous clearly improved the device stability and their investigation suggested that this is due to the formation of a more stable SEI layer on top of doped silicon.

To summarize, while there are clear limitation in the use of thin films with respect of their thickness and weight loading (typically lower than 0.1 mg/cm2) [77-79], the study of silicon thin films has played an important role in understanding the advantages and limitation of this material, in particular with respect of the solid electrolyte interphase formation [83, 84], in electrochemical energy storage applications.

1.4.2 Tin

Tin is another promising candidate for the development of the next generation anodes of lithium ion batteries. Tin and lithium forms a stable Li4.4Sn alloy, corresponding to a theoretical capacity of 994 mAh/g [85]. The operating voltage is higher than that of silicon [86]. This decreases the energy density of the

battery, but on the other hand ensures that it operates further away from a regime that can lead to lithium deposition onto the electrode surface. Many of the issues described earlier with respect of silicon are also present when working with tin. Tin undergoes a large volume expansion upon lithiation, which leads to material pulverization and to capacity fading. Similar strategies to those explored for silicon have also been applied to tin-based anodes. Nanostructuring helps preventing fracture , while mixing and composition with other current carrying materials such as carbon-based additives [87-96], metal oxides [97-99] and metals [100-102] improves the device stability.

The use of carbon-based structures is promising because of the good electrical transport properties of carbon, and because of its abundance and low-cost. There are reports of tin nanoparticles and nanowires supported by graphite [103, 104], graphene [105-107], amorphous carbon [96, 108] and carbon nanofibers/tubes [109-111]. All these reports demonstrated a clear improvement compared to pristine tin nanostructures.

For example, Chen et al. [106] reported the fabrication of Sn-graphene hybrid nanostructures via a multi-step process involving first the formation of a SnCl4 – graphene oxide aqueous mixture, followed by microwave annealing to give a SnO2-graphene oxide nanostructure. Annealing in H2 at 300° C for 2 hours is then sufficient to reduce the structure to a tin nanoparticle – graphene sheet

hybrid. The resulting anode showed an initial capacity of ~1,800 mAh/g and a capacity of 900 mAh/g after 30 cycles. It should be noted that the initial discharge capacity exceeded the theoretical maximum for tin. The authors attributed this behavior to the large surface area of the graphene sheets. Xu et al. [108] produced an amorphous carbon sponge – tin nanoparticle hybrid by a polymerization process around SnO_2 particles, followed by carbonization and thermal reduction. This material exhibited a ~1,300 mAh/g capacity of 400 cycles. The weight loading was 1.2 mg/cm2. The higher than theoretical capacity was also attributed to the defective nature of the amorphous carbon matrix, which can lead to storage of lithium ions. A similar approach was also explored by Xu et al. [91], who used spray pyrolysis to process a mixture of $SnCl_2$ and PVP in ethanol and produce in a single step agglomerates of tin nanocrystals embedded in a carbon matrix, shown in Figure 10. The resulting anode maintained a capacity of 700 mAh/g from more than 120 cycles.

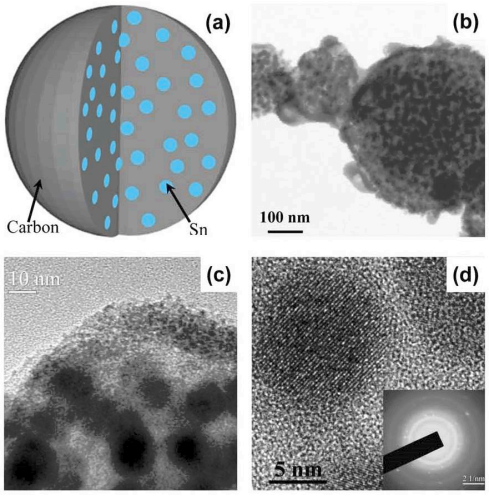

Figure 1.10 (a) Diagram of Sn−C composite particle, (b) TEM image, and (c, d) high-resolution images of the nano-Sn/C composite particles. Inset: SAED image. Reprinted with permission from ref [91]. Copyright (2013) American Chemical Society.

Carbon nanotubes have also been combined with tin nanostructures for energy storage applications. Wang et al. [110] used a template growth technique to produced carbon nanotubes with tin nanoparticles embedded within their walls. The resulting battery showed a ~1,000 mAh/g capacity for 80 cycles. The authors attributed the good performance to the good electrical contact between the tin and the carbon backbone and to the good structural stability of the electrode. Similar structures have also been realized using a potentially scalable technique such as electrospinning [109, 111]. Researchers active in this area also explored the viability of engineering a buffer space between the tin core and a carbon shell to accommodate the nanoparticle volume change during lithiation. This is analogous to the yolk-shell design already discussed for the case of silicon. Zhang et al. [89] realized such structures (see Figure 1.11), and the resulting battery presented a capacity of 800 mAh/g for the first ten cycles and maintained a capacity higher than 500 mAh/g after 100 cycles.

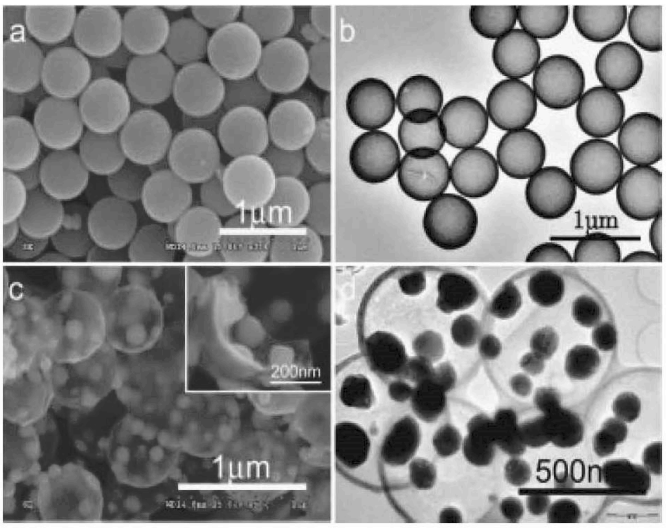

Figure 1.11 a) SEM image of SnO_2 coating SiO_2 sphere; b) TEM image of the hollow SnO_2 spheres; c) and d) SEM and TEM images of tin nanoparticles encapsulated in hollow carbon spheres, respectively. Reprinted with permission from ref [89]. Copyright (2008) John Wiley and Sons,

1.4.3. Metal oxides

A variety of metal oxides have been actively investigated as anodes for lithium ion batteries. The main motivation driving this area is the fact that these materials are abundant and generally inexpensive. Materials such as tin oxide [112, 113], nickel oxide [114, 115], iron oxide [116, 117], cobalt oxide [118-120] and titanium oxide [121, 122] have all been the subject of research efforts.

1.4.3.1 Tin Oxide

Tin oxide has received considerable attention because of its high theoretical capacity, equal to 780 mAh/g [123]. The lithiation mechanism proceeds via a two-steps process in which tin oxide is first reduced to tin, after which tin is lithiated to

the maximum theoretical form of Li4.4Sn. This mechanism also explains why tin oxide shows poor cycling stability: the expansion of tin during lithiation can induce fractures in the surrounding lithium oxide matrix, reducing the activity of the material [124, 125]. Proposed strategies to overcome this issue are nanostructuring of SnO2 to form nanowires [125], hollow nanoparticles [126, 127], binding with carbon [128], and hybrid SnO2/C hollow nanospheres [129]. Wu et al. [128] synthesized SnO2 nanosheets via an hydrothermal method and obtained a capacity of ~500 mAh/g after 50 cycles. Lou and coworkers [129] designed and fabricated hollow SnO2 nanospheres with an additional carbon coating. This structure showed a capacity of ~600 mAh/g after 80 cycles at 0.8C rate, and maintained a capacity of 500 mAh/g after 200 cycles. The outer carbon shell offers a mechanically robust electrical conduction pathway while the inner cavity provides buffer volume to accommodate for the expansion of the active material during lithiation.

1.4.3.2 Titanium Oxide

Titanium dioxide behaves quite differently than SnO2. Lithium intercalates in the TiO2 anatase structure to give a maximum theorethical capacity of 168 mAh/g [130, 131]. While this value is relatively low, TiO2 is an inexpensive and environmentally friendly material. The main issue limiting its application in batteries is its poor conductivity and slow lithium ion diffusion rate. Therefore

most of the efforts have focused on designing the material structure to overcome transport limitations. Fu et al. [132] synthesized core-shell TiO2/carbon nanoparticles by coating the TiO2 particles with polyacrylonitrile (PAN) followed by thermal annealing. The resulting structure showed good electrochemical properties. Wang et al. [133] produced TiO2 nanoparticle – decorated graphene flakes which exhibited a capacity of ~160 mAh/g for 100 cycles. Other groups tailored the morphology of the TiO2 structure to reduce the effective diffusion path, thus optimizing the material utilization. Wang and coworkers [134] used a Cu_2O template to grow the hollow TiO2 nanocages shown in Figure 1.12. After mixing with carbon black and a common binder (PVDF), the anode showed a capacity of 150 mAh/g for 200 cycles at 0.5C. The author attributed the good performance not only to the short diffusion length (equal to the thickness of the TiO2 wall, roughly 20 nm) but also to the capability of this structure to accommodate for volume changes. TiO2 nanowires have also been investigated as potential anode material. Liu et al. [135] reported the hydrothermal synthesis of anatase TiO2 wire arrays on titanium foil. The electrode exhibited a capacity of 250 mAh/g for 50 cycles.

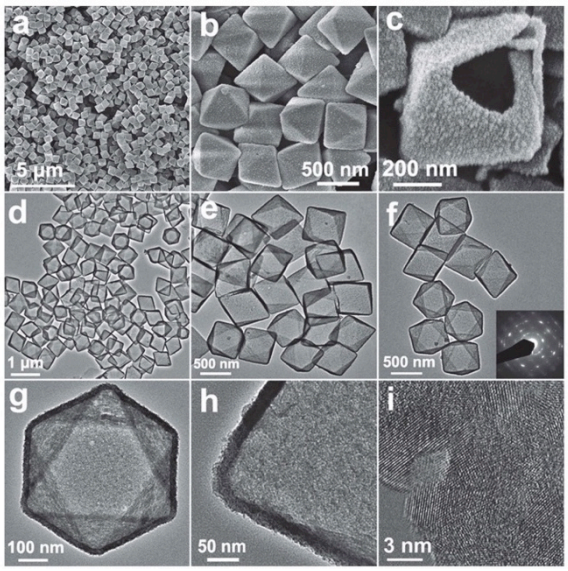

Figure 1.12 (a, b) SEM images of octahedral TiO2 nanocages with an average edge length of 500 nm; (c) a cracked nanocage; (d-f) TEM images of these nanocages; the inset in (f) is a SAED pattern; (g) a free-standing nanocage showing each plane is an equilateral triangle; (h) shell structure; (i) HRTEM image of a nanocage. Reprinted with permission from ref [134]. Copyright (2012) John Wiley and Sons, Inc.

1.4.3.3 Transition metal oxides

Poizot et al. [119] discovered that transition metal oxides such as cobalt oxide can be reversible reduced by lithium to metallic cobalt and lithium oxide: CoO + 2 Li → Co + Li_2O. More than one electron is involved in this reaction, and as a result high theoretical capacities are achievable using these oxides. For example these oxides have the corresponding maximum theoretical capacities: CoO ~715 mAh/g [136], CuO ~670 mAh/g [137], MoO3 ~830 mAh/g [138]. However, metal oxides suffer from poor electrical transport properties and from poor diffusion kinetics. The XRD and in-situ Raman studies performed by Lee et al. [139] for the case of MoO3 confirm that significant structural changes and volume expansion occur during lithiation-delithiation. Nanostructuring has been proposed

as a strategy to overcome these limitations. The case of iron (III) oxide is particularly interesting because of its obvious abundance and low-cost, and because the reaction with lithium involves six elementary charges leading to a theoretical capacity of 1,005 mAh/g ($Fe_2O_3 + 6Li^+ + 6e^- \rightarrow 2Fe + 3Li_2O$) [117]. The delithiation and lithiation peaks for Fe_2O_3 are at 1.6 V and 0.8 V respectively, compatible with its use as anode material [116, 140]. Various types of iron oxide structures have been studied to alleviate the transport limitations, including nanoparticles [117], mesoporous structures [141], nanorods [142] and particles coated with a carbon shell [143]. In our opinion, the work of Zhu et al. [117] is particularly interesting: Fe_2O_3 was uniformly decorated onto graphene sheets, and the resulting electrode has an initial discharge capacity of ~1,700 mAh/g and a capacity exceeding 1,000 mAh/g after 50 cycles. The excess initial capacity was attributed to lithium ion irreversibly reacting with the graphene sheet defects. The good stability was attributed to the intimate contact between the graphene support and the oxide particles which prevented their agglomeration and the subsequent deactivation of the material. The higher surface area, which increases the lithium ions diffusion rate, and the good structure stability of nanostructured transition metal oxide composites greatly improves their electrochemical performance as anode materials for lithium ion batteries.

1.4.4 Conclusion

Overall, it is undisputable that there has been terrific progress in the area of materials development for next generation anode technologies. It is also clear that silicon has attracted the vast majority of the attention from the academic community. While this is motivated primarily by its superior gravimetric capacity compared to other candidates, we should point out that from the application point of view the most important figure of merit is the volumetric capacity of the overall battery stack (Wh/L). On a volumetric basis, the advantage of silicon with respect of tin is smaller. Nevertheless, silicon is going to continue being actively investigated because of its other advantages, mainly its abundance and ease of processing. In our opinion, we can draw the following conclusions based on above discussions:

- The combination of silicon nanoparticles with an effective current-carrying additive is crucially important for device performance.
- Embedding silicon particles in a carbon matrix seems to be a very promising strategy [60-62, 144]. More detailed studies on the structure and chemistry of the carbon matrix are greatly needed to further optimize this approach.
- Engineering a buffer volume to accommodate for the volume expansion during lithiation is also promising [20, 23, 64], although it presents challenges from the point of view of processing scalability.

- Spray pyrolysis is establishing itself as a powerful technique for the production of powders with good control of structure and chemical composition [62, 63]. It is an inherently scalable technique therefore it holds great promise as scale-up issues become relevant.
- Additives such as fluoroethylene carbonate can improve the performance of Si-containing anodes significantly [29, 30]. This consideration raises questions whether additional improvements are possible by further investigation of the electrolyte chemistry.
- The lack of a binder that can maintain structural stability while accommodating for the volume change of a silicon particle is an unresolved problem, despite some recent promising attempts to address this issue [24, 25, 27, 66].

Researchers active in this area have successfully developed Si-containing structures that have excellent stability and now reach the long cycle barrier. It is also apparent that there seems to be a drawback between stability and capacity: structures that show higher capacity also show a reduced stability. This has to be expected, in light of the previous discussion on the problems associated with the large volume change in silicon during lithiation. Despite this tradeoff, the capability of achieving a 1000 cycle life with a material that undergoes a 280% volume expansion during cycling is remarkable.

We should also keep in mind that such reports focus on the correlation between electrochemical performance (capacity, stability) and the parameters of the

materials design (dimensionality, structure, composition etc.). The vast majority of the previous discussions draw conclusions based on an analysis of gravimetric capacity in a half-cell. While this may be appropriate for determining the potential quality of a particular nanostructure for energy storage applications, it is far from being meaningful in real-life applications. Moreover, for most of the reports cited in this chapter, the material weight loading onto the conductive substrate is low (<1 mg/cm2) which results in an energy density which is far from that utilized in commercial devices. Many of these structures have high porosity and still present significant irreversible capacity loss in the first cycle. As recently pointed out by Obrovac et al. [145], this severely limits or eliminates altogether any advantage offered by the use of a high-capacity material such as silicon when the overall stack volumetric energy density is calculated (see Figure 1.13).

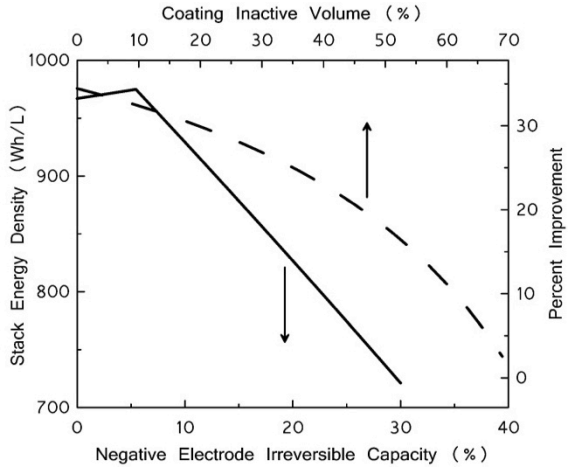

Figure 1.13 Stack energy density and the percent energy improvement (over a conventional graphite cell) as a function of anode inactive volume and irreversible capacity for a typical cell stack, using a silicon anode. Reprinted with permission from ref [145]. Copyright (2014) American Chemical Society.

In 2012, roughly 38,000 tons of materials have been processed for the manufacturing of the anodes for lithium-ion batteries [147]. More than 50% of the anode materials market is covered by natural graphite [147]. Producing a potentially complex nanostructure at the similar volume level, while maintaining economic feasibility, is a daunting task. The manufacturability of nanomaterials is an unresolved issue which is relevant not only for energy storage but for several other applications (in particular in the energy-related fields). There has been tremendous progress in the synthesis and processing of silicon nanostructures. For instance, a variety of techniques are capable of producing silicon nanoparticles at good production rate even in a lab scale setting. For instance, laser pyrolysis of silane [148] and non-thermal plasma synthesis techniques [149, 150] can produce ultrafine (<10 nm), high purity silicon nanocrystals with yields higher than 100 mg/hour. Alternatively, silicon nanopowders can be produced starting from silica using magnesiothermic reduction [151, 152]. Powders produced using magnesiothermic purification typically do not reach the purities required in electronic applications, but this requirement may be less stringent for battery applications. Silicon nanowires can also be produced in large batches using supercritical solution routes [76, 153, 154].

While researchers have made great progress in developing nanostructures that eliminate the issues introduced by the use of alternative materials such as silicon for electrochemical energy storage, there is still plenty of progress to be done

with respect of the processing science of such nanostructures. This is going to become a critical bottleneck that needs to be overcome to enable the use of next-generation battery materials in commercial applications.

1.5 Objective of This Study

The objective of this research is to investigate silicon-containing anode materials By synthesizing, characterizing and testing electrochemical performance of the silicon-based structures, we aim at understanding mechanism in silicon-containing anode materials and fabricating next generation anode materials with high energy capacity, long cycle life and low cost for LIBs that are superior when compare with current commercialized graphite anode.

Reference:

[1] Feldman, D., G. Barbose, R. Margolis, T. James, S. Weaver, N. Darghuth, R. Fu, C. Davidson, S. Booth, and R. Wiser, *Photovoltaic system pricing trends*, 2014, SunShot - U.S. Department of Energy.

[2] Mai, T., D. Sandor, R. Wiser, and T. Schneider, *Renewable electricity futures study*, 2012, National Renewable Energy Laboratory.

[3] Eyer, J.M., J.J. Iannucci, and G.P. Corey, *Energy storage benefits and market analysis handbook - A study for the DOE energy storage systems program*, 2004, Sandia National Laboratory.

[4] Johansson B. A broadened typology on energy and security. *Energy*,*53*, 2013, 199-205.

[5] Tarascon, J. M., & Armand, M. (2001). Issues and challenges facing rechargeable lithium batteries. *Nature*, *414*(6861), 359-367.

[6] http://batteryuniversity.com/learn/article/secondary_batteries.

[7] Stewart S., Christensen J., Chaturvedi N., Kojic A., Research and Technology Center North America, 2014.

[8] Molenda, J., & Molenda, M. (2011). INTECH Open Access Publisher.

[9] Mizushima, K., Jones, P. C., Wiseman, P. J., & Goodenough, J. B. LixCoO2 A new cathode material for batteries of high energy density (Materials Research Bulletin, 15(6), 783-789, 1980.

[10] Winter, M., Besenhard, J. O., Spahr, M. E., & Novak, P. (1998). Insertion electrode materials for rechargeable lithium batteries. *Advanced materials*,*10*(10), 725-763.

[11] as reported by the Web of Science, Thomson Reuters search engine.

[12] Obrovac, M.N. and L. Christensen, *Structural changes in silicon anodes during lithium insertion/extraction.* Electrochemical and Solid State Letters, 2004. **7**(5): p. A93-A96.

[13] Chan, C.K., H.L. Peng, G. Liu, K. McIlwrath, X.F. Zhang, R.A. Huggins, and Y. Cui, *High-performance lithium battery anodes using silicon nanowires.* Nature nanotechnology, 2008. **3**(1): p. 31-35.

[14] Teki, R., M.K. Datta, R. Krishnan, T.C. Parker, T.-M. Lu, P.N. Kumta, and N. Koratkar, *Nanostructured Silicon Anodes for Lithium Ion Rechargeable Batteries.* Small, 2009. **5**(20): p. 2236-2242.

[15] Green, M., E. Fielder, B. Scrosati, M. Wachtler, and J.S. Moreno, *Structured Silicon Anodes for Lithium Battery Applications.* Electrochemical and Solid-State Letters, 2003. **6**(5): p. A75-A79.

[16] Liu, X.H., L. Zhong, S. Huang, S.X. Mao, T. Zhu, and J.Y. Huang, *Size-Dependent Fracture of Silicon Nanoparticles During Lithiation.* Acs Nano, 2012. **6**(2): p. 1522-1531.

[17] Ruffo, R., S.S. Hong, C.K. Chan, R.A. Huggins, and Y. Cui, *Impedance Analysis of Silicon Nanowire Lithium Ion Battery Anodes.* The Journal of Physical Chemistry C, 2009. **113**(26): p. 11390-11398.

[18] Chan, T.L. and J.R. Chelikowsky, *Controlling Diffusion of Lithium in Silicon Nanostructures.* Nano Letters, 2010. **10**(3): p. 821-825.

[19] Evanoff, K., A. Magasinski, J.B. Yang, and G. Yushin, *Nanosilicon-Coated Graphene Granules as Anodes for Li-Ion Batteries.* Advanced Energy Materials, 2011. **1**(4): p. 495-498.

[20] Liu, Y., K. Hanai, J. Yang, N. Imanishi, A. Hirano, and Y. Takeda, *Silicon/Carbon Composites as Anode Materials for Li-Ion Batteries.* Electrochemical and Solid-State Letters, 2004. **7**(10): p. A369-A372.

[21] Zhang, Y., X.G. Zhang, H.L. Zhang, Z.G. Zhao, F. Li, C. Liu, and H.M. Cheng, *Composite anode material of silicon/graphite/carbon nanotubes for Li-ion batteries.* Electrochimica Acta, 2006. **51**(23): p. 4994-5000.

[22] Gao, P., J. Fu, J. Yang, R. Lv, J. Wang, Y. Nuli, and X. Tang, *Microporous carbon coated silicon core/shell nanocomposite via in situpolymerization for advanced Li-ion battery anode material.* Physical Chemistry Chemical Physics, 2009. **11**(47): p. 11101-11105.

[23] Liu, N., H. Wu, M.T. McDowell, Y. Yao, C.M. Wang, and Y. Cui, *A Yolk-Shell Design for Stabilized and Scalable Li-Ion Battery Alloy Anodes.* Nano Letters, 2012. **12**(6): p. 3315-3321.

[24] Guo, J. and C. Wang, *A polymer scaffold binder structure for high capacity silicon anode of lithium-ion battery.* Chemical Communications, 2010. **46**(9): p. 1428-1430.

[25] Wang, C., H. Wu, Z. Chen, M.T. McDowell, Y. Cui, and Z. Bao, *Self-healing chemistry enables the stable operation of silicon microparticle anodes for high-energy lithium-ion batteries.* Nat Chem, 2013. **5**(12): p. 1042-1048.

[26] Wu, M., X. Xiao, N. Vukmirovic, S. Xun, P.K. Das, X. Song, P. Olalde-Velasco, D. Wang, A.Z. Weber, L.-W. Wang, V.S. Battaglia, W. Yang, and G. Liu, *Toward an Ideal Polymer Binder Design for High-Capacity Battery Anodes.* Journal of the American Chemical Society, 2013. **135**(32): p. 12048-12056.

[27] Kovalenko, I., B. Zdyrko, A. Magasinski, B. Hertzberg, Z. Milicev, R. Burtovyy, I. Luzinov, and G. Yushin, *A Major Constituent of Brown Algae for Use in High-Capacity Li-Ion Batteries.* Science, 2011. **334**(6052): p. 75-79.

[28] Mazouzi, D., Z. Karkar, C. Reale Hernandez, P. Jimenez Manero, D. Guyomard, L. Roué, and B. Lestriez, *Critical roles of binders and formulation at multiscales of silicon-based composite electrodes.* Journal of Power Sources, 2015. **280**(0): p. 533-549.

[29] Choi, N.-S., K.H. Yew, K.Y. Lee, M. Sung, H. Kim, and S.-S. Kim, *Effect of fluoroethylene carbonate additive on interfacial properties of silicon thin-film electrode.* Journal of Power Sources, 2006. **161**(2): p. 1254-1259.

[30] Etacheri, V., O. Haik, Y. Goffer, G.A. Roberts, I.C. Stefan, R. Fasching, and D. Aurbach, *Effect of Fluoroethylene Carbonate (FEC) on the Performance and Surface Chemistry of Si-Nanowire Li-Ion Battery Anodes.* Langmuir, 2012. **28**(1): p. 965-976.

[31] Chen, L., K. Wang, X. Xie, and J. Xie, *Enhancing Electrochemical Performance of Silicon Film Anode by Vinylene Carbonate Electrolyte Additive.* Electrochemical and Solid-State Letters, 2006. **9**(11): p. A512-A515.

[32] Chen, L., K. Wang, X. Xie, and J. Xie, *Effect of vinylene carbonate (VC) as electrolyte additive on electrochemical performance of Si film anode for lithium ion batteries.* Journal of Power Sources, 2007. **174**(2): p. 538-543.

[33] Ryu, I., J.W. Choi, Y. Cui, and W.D. Nix, *Size-dependent fracture of Si nanowire battery anodes.* Journal of the Mechanics and Physics of Solids, 2011. **59**(9): p. 1717-1730.

[34] Kim, H., M. Seo, M.H. Park, and J. Cho, *A Critical Size of Silicon Nano-Anodes for Lithium Rechargeable Batteries.* Angewandte Chemie-International Edition, 2010. **49**(12): p. 2146-2149.

[35] Shkrob, I.A., Y. Zhu, T.W. Marin, and D. Abraham, *Reduction of Carbonate Electrolytes and the Formation of Solid-Electrolyte Interface (SEI) in Lithium-Ion Batteries. 1. Spectroscopic Observations of Radical Intermediates Generated in One-Electron Reduction of Carbonates.* The Journal of Physical Chemistry C, 2013. **117**(38): p. 19255-19269.

[36] Nie, M., D.P. Abraham, Y. Chen, A. Bose, and B.L. Lucht, *Silicon Solid Electrolyte Interphase (SEI) of Lithium Ion Battery Characterized by Microscopy and Spectroscopy.* The Journal of Physical Chemistry C, 2013. **117**(26): p. 13403-13412.

[37] Xu, Y., G. Yin, Y. Ma, P. Zuo, and X. Cheng, *Nanosized core/shell silicon@carbon anode material for lithium ion batteries with polyvinylidene fluoride as carbon source.* Journal of Materials Chemistry, 2010. **20**(16): p. 3216-3220.

[38] Guo, J.C., A. Sun, X.L. Chen, C.S. Wang, and A. Manivannan, *Cyclability study of silicon-carbon composite anodes for lithium-ion batteries using electrochemical impedance spectroscopy.* Electrochimica Acta, 2011. **56**(11): p. 3981-3987.

[39] Dimov, N., K. Fukuda, T. Umeno, S. Kugino, and M. Yoshio, *Characterization of carbon-coated silicon: Structural evolution and possible limitations.* Journal of Power Sources, 2003. **114**(1): p. 88-95.

[40] Ng, S.H., J. Wang, K. Konstantinov, D. Wexler, S.Y. Chew, Z. Guo, and H.K. Liu, *Spray-pyrolyzed silicon/disordered carbon nanocomposites for lithium-ion battery anodes.* Journal of Power Sources, 2007. **174**(2): p. 823-827.

[41] Ng, S.H., J. Wang, D. Wexler, S.Y. Chew, and H.K. Liu, *Amorphous Carbon-Coated Silicon Nanocomposites: A Low-Temperature Synthesis via Spray Pyrolysis and Their Application as High-Capacity Anodes for Lithium-Ion Batteries.* The Journal of Physical Chemistry C, 2007. **111**(29): p. 11131-11138.

[42] Holzapfel, M., H. Buqa, W. Scheifele, P. Novak, and F.-M. Petrat, *A new type of nano-sized silicon/carbon composite electrode for reversible lithium insertion.* Chemical Communications, 2005(12): p. 1566-1568.

[43] Liu, B., P. Soares, C. Checkles, Y. Zhao, and G. Yu, *Three-Dimensional Hierarchical Ternary Nanostructures for High-Performance Li-Ion Battery Anodes.* Nano Letters, 2013. **13**(7): p. 3414-3419.

[44] Shu, J., H. Li, R. Yang, Y. Shi, and X. Huang, *Cage-like carbon nanotubes/Si composite as anode material for lithium ion batteries.* Electrochemistry Communications, 2006. **8**(1): p. 51-54.

[45] Martin, C., M. Alias, F. Christien, O. Crosnier, D. Belanger, and T. Brousse, *Graphite-grafted silicon nanocomposite as a negative electrode for lithium-ion batteris.* Advanced Materials, 2009. **21**: p. 1-7.

[46] Zhao, X., C.M. Hayner, M.C. Kung, and H.H. Kung, *In-Plane Vacancy-Enabled High-Power Si-Graphene Composite Electrode for Lithium-Ion Batteries.* Advanced Energy Materials, 2011. **1**(6): p. 1079-1084.

[47] Lee, J.K., K.B. Smith, C.M. Hayner, and H.H. Kung, *Silicon nanoparticles-graphene paper composites for Li ion battery anodes.* Chemical Communications, 2010. **46**(12): p. 2025-2027.

[48] Wen, Y., Y. Zhu, A. Langrock, A. Manivannan, S.H. Ehrman, and C. Wang, *Graphene-Bonded and -Encapsulated Si Nanoparticles for Lithium Ion Battery Anodes.* Small, 2013. **9**(16): p. 2810-2816.

[49] Du, Z., R.A. Dunlap, and M.N. Obrovac, *High Energy Density Calendered Si Alloy/Graphite Anodes.* Journal of the Electrochemical Society, 2014. **161**(10): p. A1698-A1705.

[50] Datta, M.K. and P.N. Kumta, *Silicon and carbon based composite anodes for lithium ion batteries.* Journal of Power Sources, 2006. **158**(1): p. 557-563.

[51] Jo, Y.N., Y. Kim, J.S. Kim, J.H. Song, K.J. Kim, C.Y. Kwag, D.J. Lee, C.W. Park, and Y.J. Kim, *Si-graphite composites as anode materials for lithium secondary batteries.* Journal of Power Sources, 2010. **195**(18): p. 6031-6036.

[52] Wen, Y., Y.J. Zhu, A. Langrock, A. Manivannan, S.H. Ehrman, and C.S. Wang, *Graphene-Bonded and -Encapsulated Si Nanoparticles for Lithium Ion Battery Anodes.* Small, 2013. **9**(16): p. 2810-2816.

[53] Martin, C., O. Crosnier, R. Retoux, D. Belanger, D.M. Schleich, and T. Brousse, *Chemical Coupling of Carbon Nanotubes and Silicon Nanoparticles for Improved Negative Electrode Performance in Lithium-Ion Batteries.* Advanced Functional Materials, 2011. **21**(18): p. 3524-3530.

[54] Zhu, Y., W. Liu, X. Zhang, J. He, J. Chen, Y. Wang, and T. Cao, *Directing Silicon–Graphene Self-Assembly as a Core/Shell Anode for High-Performance Lithium-Ion Batteries.* Langmuir, 2013. **29**(2): p. 744-749.

[55] Gohier, A., B. Laïk, K.-H. Kim, J.-L. Maurice, J.-P. Pereira-Ramos, C.S. Cojocaru, and P.T. Van, *High-Rate Capability Silicon Decorated Vertically Aligned Carbon Nanotubes for Li-Ion Batteries.* Advanced Materials, 2012. **24**(19): p. 2592-2597.

[56] Zhou, X., L.-J. Wan, and Y.-G. Guo, *Electrospun Silicon Nanoparticle/Porous Carbon Hybrid Nanofibers for Lithium-Ion Batteries.* Small, 2013. **9**(16): p. 2684-2688.

[57] Li, Y., G. Xu, L. Xue, S. Zhang, Y. Yao, Y. Lu, O. Toprakci, and X. Zhang, *Enhanced Rate Capability by Employing Carbon Nanotube-Loaded Electrospun Si/C Composite Nanofibers As Binder-Free Anodes.* Journal of the Electrochemical Society, 2013. **160**(3): p. A528-A534.

[58] Hwang, T.H., Y.M. Lee, B.-S. Kong, J.-S. Seo, and J.W. Choi, *Electrospun Core–Shell Fibers for Robust Silicon Nanoparticle-Based Lithium Ion Battery Anodes.* Nano Letters, 2012. **12**(2): p. 802-807.

[59] Ji, L. and X. Zhang, *Electrospun carbon nanofibers containing silicon particles as an energy-storage medium.* Carbon, 2009. **47**(14): p. 3219-3226.

[60] Guo, J., Z. Yang, and L.A. Archer, *Mesoporous silicon@carbon composites via nanoparticle-seeded dispersion polymerization and their application as lithium-ion battery anode materials.* Journal of Materials Chemistry A, 2013. **1**(18): p. 5709-5714.

[61] Jeong, H.M., S.Y. Lee, W.H. Shin, J.H. Kwon, A. Shakoor, T.H. Hwang, S.Y. Kim, B.-S. Kong, J.-S. Seo, Y.M. Lee, J.K. Kang, and J.W. Choi, *Silicon@porous nitrogen-doped carbon spheres through a bottom-up approach are highly robust lithium-ion battery anodes.* RSC Advances, 2012. **2**(10): p. 4311-4317.

[62] Jung, D.S., T.H. Hwang, S.B. Park, and J.W. Choi, *Spray Drying Method for Large-Scale and High-Performance Silicon Negative Electrodes in Li-Ion Batteries.* Nano Letters, 2013. **13**(5): p. 2092-2097.

[63] Yang, Z., J. Guo, S. Xu, Y. Yu, H.D. Abruña, and L.A. Archer, *Interdispersed silicon–carbon nanocomposites and their application as anode materials for lithium-ion batteries.* Electrochemistry Communications, 2013. **28**(0): p. 40-43.

[64] Liu, N., Z. Lu, J. Zhao, M.T. McDowell, H.-W. Lee, W. Zhao, and Y. Cui, *A pomegranate-inspired nanoscale design for large-volume-change lithium battery anodes.* Nat Nano, 2014. **9**(3): p. 187-192.

[65] Lu, Z., N. Liu, H.-W. Lee, J. Zhao, W. Li, Y. Li, and Y. Cui, *Nonfilling Carbon Coating of Porous Silicon Micrometer-Sized Particles for High-Performance Lithium Battery Anodes.* Acs Nano, 2015. **9**(3): p. 2540-2547.

[66] Park, S.-J., H. Zhao, G. Ai, C. Wang, X. Song, N. Yuca, V.S. Battaglia, W. Yang, and G. Liu, *Side-Chain Conducting and Phase-Separated Polymeric Binders for High-Performance Silicon Anodes in Lithium-Ion Batteries.* Journal of the American Chemical Society, 2015. **137**(7): p. 2565-2571.

[67] Kasavajjula, U., C.S. Wang, and A.J. Appleby, *Nano- and bulk-silicon-based insertion anodes for lithium-ion secondary cells.* Journal of Power Sources, 2007. **163**(2): p. 1003-1039.

[68] Lee, S.W., M.T. McDowell, J.W. Choi, and Y. Cui, *Anomalous Shape Changes of Silicon Nanopillars by Electrochemical Lithiation.* Nano Letters, 2011. **11**(7): p. 3034-3039.

[69] Yao, Y., N. Liu, M.T. McDowell, M. Pasta, and Y. Cui, *Improving the cycling stability of silicon nanowire anodes with conducting polymer coatings.* Energy & Environmental Science, 2012. **5**(7): p. 7927-7930.

[70] Bogart, T.D., D. Oka, X.T. Lu, M. Gu, C.M. Wang, and B.A. Korgel, *Lithium Ion Battery Peformance of Silicon Nanowires with Carbon Skin.* Acs Nano, 2014. **8**(1): p. 915-922.

[71] Huang, R., X. Fan, W. Shen, and J. Zhu, *Carbon-coated silicon nanowire array films for high-performance lithium-ion battery anodes.* Applied Physics Letters, 2009. **95**(13): p. 133119.

[72] Cho, Y.J., H.S. Kim, H. Im, Y. Myung, G.B. Jung, C.W. Lee, J. Park, M.-H. Park, J. Cho, and H.S. Kang, *Nitrogen-Doped Graphitic Layers Deposited on Silicon Nanowires for Efficient Lithium-Ion Battery Anodes.* The Journal of Physical Chemistry C, 2011. **115**(19): p. 9451-9457.

[73] Wu, H., G. Chan, J.W. Choi, I. Ryu, Y. Yao, M.T. McDowell, S.W. Lee, A. Jackson, Y. Yang, L.B. Hu, and Y. Cui, *Stable cycling of double-walled silicon nanotube battery anodes through solid-electrolyte interphase control.* Nature Nanotechnology, 2012. **7**(5): p. 309-314.

[74] Song, T., J. Xia, J.-H. Lee, D.H. Lee, M.-S. Kwon, J.-M. Choi, J. Wu, S.K. Doo, H. Chang, W.I. Park, D.S. Zang, H. Kim, Y. Huang, K.-C. Hwang, J.A. Rogers, and U. Paik, *Arrays of*

Sealed Silicon Nanotubes As Anodes for Lithium Ion Batteries. Nano Letters, 2010. **10**(5): p. 1710-1716.

[75] Chevrier, V.L., L. Liu, D.B. Le, J. Lund, B. Molla, K. Reimer, L.J. Krause, L.D. Jensen, E. Figgemeier, and K.W. Eberman, *Evaluating Si-Based Materials for Li-Ion Batteries in Commercially Relevant Negative Electrodes.* Journal of the Electrochemical Society, 2014. **161**(5): p. A783-A791.

[76] Chan, C.K., R.N. Patel, M.J. O'Connell, B.A. Korgel, and Y. Cui, *Solution-Grown Silicon Nanowires for Lithium-Ion Battery Anodes.* Acs Nano, 2010. **4**(3): p. 1443-1450.

[77] Kim, J.-B., H.-Y. Lee, K.-S. Lee, S.-H. Lim, and S.-M. Lee, *Fe/Si multi-layer thin film anodes for lithium rechargeable thin film batteries.* Electrochemistry Communications, 2003. **5**(7): p. 544-548.

[78] Chen, L.B., J.Y. Xie, H.C. Yu, and T.H. Wang, *An amorphous Si thin film anode with high capacity and long cycling life for lithium ion batteries.* Journal of Applied Electrochemistry, 2009. **39**(8): p. 1157-1162.

[79] Liu, H., L. Hu, Y.S. Meng, and Q. Li, *Electrodeposited three-dimensional Ni-Si nanocable arrays as high performance anodes for lithium ion batteries.* Nanoscale, 2013. **5**(21): p. 10376-10383.

[80] Zhang, H. and P.V. Braun, *Three-Dimensional Metal Scaffold Supported Bicontinuous Silicon Battery Anodes.* Nano Letters, 2012. **12**(6): p. 2778-2783.

[81] Zhang, S., Z. Du, R. Lin, T. Jiang, G. Liu, X. Wu, and D. Weng, *Nickel Nanocone-Array Supported Silicon Anode for High-Performance Lithium-Ion Batteries.* Advanced Materials, 2010. **22**(47): p. 5378-5382.

[82] Andreas Arie, A., W. Chang, and J. Kee Lee, *Electrochemical characteristics of semi conductive silicon anode for lithium polymer batteries.* Journal of Electroceramics, 2010. **24**(4): p. 308-312.

[83] Song, S.-W. and S.-W. Baek, *Silane-Derived SEI Stabilization on Thin-Film Electrodes of Nanocrystalline Si for Lithium Batteries.* Electrochemical and Solid-State Letters, 2009. **12**(2): p. A23-A27.

[84] Arreaga-Salas, D.E., A.K. Sra, K. Roodenko, Y.J. Chabal, and C.L. Hinkle, *Progression of Solid Electrolyte Interphase Formation on Hydrogenated Amorphous Silicon Anodes for Lithium-Ion Batteries.* The Journal of Physical Chemistry C, 2012. **116**(16): p. 9072-9077.

[85] Courtney, I.A. and J.R. Dahn, *Electrochemical and In Situ X-Ray Diffraction Studies of the Reaction of Lithium with Tin Oxide Composites.* Journal of the Electrochemical Society, 1997. 144(6): p. 2045-2052.

[86] Winter, M. and J.O. Besenhard, *Electrochemical lithiation of tin and tin-based intermetallics and composites.* Electrochimica Acta, 1999. **45**(1–2): p. 31-50.

87] Kim, I.-S. and P.N. Kumta, *High capacity Si/C nanocomposite anodes for Li-ion batteries.* Journal of Power Sources, 2004. **136**(1): p. 145-149.

[88] Idota, Y., T. Kubota, A. Matsufuji, Y. Maekawa, and T. Miyasaka, *Tin-Based Amorphous Oxide: A High-Capacity Lithium-Ion-Storage Material.* Science, 1997. **276**(5317): p. 1395-1397.

[89] Zhang, W.-M., J.-S. Hu, Y.-G. Guo, S.-F. Zheng, L.-S. Zhong, W.-G. Song, and L.-J. Wan, *Tin-Nanoparticles Encapsulated in Elastic Hollow Carbon Spheres for High-Performance Anode Material in Lithium-Ion Batteries.* Advanced Materials, 2008. **20**(6): p. 1160-1165.

[90] Lee, K.T., Y.S. Jung, and S.M. Oh, *Synthesis of Tin-Encapsulated Spherical Hollow Carbon for Anode Material in Lithium Secondary Batteries.* Journal of the American Chemical Society, 2003. **125**(19): p. 5652-5653.

[91] Xu, Y., Q. Liu, Y. Zhu, Y. Liu, A. Langrock, M.R. Zachariah, and C. Wang, *Uniform Nano-Sn/C Composite Anodes for Lithium Ion Batteries.* Nano Letters, 2013. **13**(2): p. 470-474.

[92] Morishita, T., T. Hirabayashi, T. Okuni, N. Ota, and M. Inagaki, *Preparation of carbon-coated Sn powders and their loading onto graphite flakes for lithium ion secondary battery.* Journal of Power Sources, 2006. **160**(1): p. 638-644.

[93] Marcinek, M., L.J. Hardwick, T.J. Richardson, X. Song, and R. Kostecki, *Microwave plasma chemical vapor deposition of nano-structured Sn/C composite thin-film anodes for Li-ion batteries.* Journal of Power Sources, 2007. **173**(2): p. 965-971.

[94] Egashira, M., H. Takatsuji, S. Okada, and J.-i. Yamaki, *Properties of containing Sn nanoparticles activated carbon fiber for a negative electrode in lithium batteries.* Journal of Power Sources, 2002. **107**(1): p. 56-60.

[95] Cui, G., Y.-S. Hu, L. Zhi, D. Wu, I. Lieberwirth, J. Maier, and K. Müllen, *A One-Step Approach Towards Carbon-Encapsulated Hollow Tin Nanoparticles and Their Application in Lithium Batteries.* Small, 2007. **3**(12): p. 2066-2069.

[96] Noh, M., Y. Kwon, H. Lee, J. Cho, Y. Kim, and M.G. Kim, *Amorphous Carbon-Coated Tin Anode Material for Lithium Secondary Battery.* Chemistry of Materials, 2005. **17**(8): p. 1926-1929.

[97] Kim, H.S., S.H. Kang, and Y.-H. Chung, *Nanophase Sn with High Capacity and Long Cycle Life on Self-supported TiO2 Nanotube for Li-ion Batteries.* Meeting Abstracts, 2009. MA2009-01(3): p. 183.

[98] Kim, H., M.G. Kim, T.J. Shin, H.-J. Shin, and J. Cho, *Tio2@Sn core–shell nanotubes for fast and high density Li-ion storage material.* Electrochemistry Communications, 2008. **10**(11): p. 1669-1672.

[99] Wang, X.-L., M. Feygenson, M.C. Aronson, and W.-Q. Han, *Sn/SnOx Core−Shell Nanospheres: Synthesis, Anode Performance in Li Ion Batteries, and Superconductivity.* The Journal of Physical Chemistry C, 2010. **114**(35): p. 14697-14703.

[100] Bazin, L., S. Mitra, P.L. Taberna, P. Poizot, M. Gressier, M.J. Menu, A. Barnabé, P. Simon, and J.M. Tarascon, *High rate capability pure Sn-based nano-architectured electrode assembly for rechargeable lithium batteries.* Journal of Power Sources, 2009. **188**(2): p. 578-582.

[101] Ren, J., X. He, L. Wang, W. Pu, C. Jiang, and C. Wan, *Nanometer copper–tin alloy anode material for lithium-ion batteries.* Electrochimica Acta, 2007. **52**(7): p. 2447-2452.

[102] Zhang, S., Y. Xing, T. Jiang, Z. Du, F. Li, L. He, and W. Liu, *A three-dimensional tin-coated nanoporous copper for lithium-ion battery anodes.* Journal of Power Sources, 2011. **196**(16): p. 6915-6919.

[103] Wang, G.X., J.-H. Ahn, M.J. Lindsay, L. Sun, D.H. Bradhurst, S.X. Dou, and H.K. Liu, *Graphite–Tin composites as anode materials for lithium-ion batteries.* Journal of Power Sources, 2001. **97–98**(0): p. 211-215.

[104] Wang, Y., J.Y. Lee, and T.C. Deivaraj, *Tin Nanoparticle Loaded Graphite Anodes for Li-Ion Battery Applications.* Journal of the Electrochemical Society, 2004. **151**(11): p. A1804-A1809.

[105] Luo, B., B. Wang, M. Liang, J. Ning, X. Li, and L. Zhi, *Reduced Graphene Oxide-Mediated Growth of Uniform Tin-Core/Carbon-Sheath Coaxial Nanocables with Enhanced Lithium Ion Storage Properties.* Advanced Materials, 2012. **24**(11): p. 1405-1409.

[106] Chen, S., Y. Wang, H. Ahn, and G. Wang, *Microwave hydrothermal synthesis of high performance tin–graphene nanocomposites for lithium ion batteries.* Journal of Power Sources, 2012. **216**(0): p. 22-27.

[107] Luo, B., B. Wang, X. Li, Y. Jia, M. Liang, and L. Zhi, *Graphene-Confined Sn Nanosheets with Enhanced Lithium Storage Capability.* Advanced Materials, 2012. **24**(26): p. 3538-3543.

[108] Xu, Y., J. Guo, and C. Wang, *Sponge-like porous carbon/tin composite anode materials for lithium ion batteries.* Journal of Materials Chemistry, 2012. **22**(19): p. 9562-9567.

[109] Prem Kumar, T., R. Ramesh, Y.Y. Lin, and G.T.-K. Fey, *Tin-filled carbon nanotubes as insertion anode materials for lithium-ion batteries.* Electrochemistry Communications, 2004. **6**(6): p. 520-525.

[110] Wang, Y., M. Wu, Z. Jiao, and J.Y. Lee, *Sn@CNT and Sn@C@CNT nanostructures for superior reversible lithium ion storage.* Chemistry of Materials, 2009. **21**(14): p. 3210-3215.

[111] Yu, Y., Q. Yang, D. Teng, X. Yang, and S. Ryu, *Reticular Sn nanoparticle-dispersed PAN-based carbon nanofibers for anode material in rechargeable lithium-ion batteries.* Electrochemistry Communications, 2010. **12**(9): p. 1187-1190.

[112] Lian, P., X. Zhu, S. Liang, Z. Li, W. Yang, and H. Wang, *High reversible capacity of SnO2/graphene nanocomposite as an anode material for lithium-ion batteries.* Electrochimica Acta, 2011. **56**(12): p. 4532-4539.

[113] Aurbach, D., A. Nimberger, B. Markovsky, E. Levi, E. Sominski, and A. Gedanken, *Nanoparticles of SnO Produced by Sonochemistry as Anode Materials for Rechargeable Lithium Batteries.* Chemistry of Materials, 2002. **14**(10): p. 4155-4163.

[114] Liu, H., G. Wang, J. Liu, S. Qiao, and H. Ahn, *Highly ordered mesoporous NiO anode material for lithium ion batteries with an excellent electrochemical performance.* Journal of Materials Chemistry, 2011. **21**(9): p. 3046-3052.

[115] Huang, X.H., J.P. Tu, X.H. Xia, X.L. Wang, J.Y. Xiang, L. Zhang, and Y. Zhou, *Morphology effect on the electrochemical performance of NiO films as anodes for lithium ion batteries.* Journal of Power Sources, 2009. **188**(2): p. 588-591.

[116] Zhang, W.-M., X.-L. Wu, J.-S. Hu, Y.-G. Guo, and L.-J. Wan, *Carbon Coated Fe3O4 Nanospindles as a Superior Anode Material for Lithium-Ion Batteries.* Advanced Functional Materials, 2008. **18**(24): p. 3941-3946.

[117] Zhu, X., Y. Zhu, S. Murali, M.D. Stoller, and R.S. Ruoff, *Nanostructured Reduced Graphene Oxide/Fe2O3 Composite As a High-Performance Anode Material for Lithium Ion Batteries.* Acs Nano, 2011. **5**(4): p. 3333-3338.

[118] Yu, Y., C.-H. Chen, J.-L. Shui, and S. Xie, *Nickel-Foam-Supported Reticular CoO–Li2O Composite Anode Materials for Lithium Ion Batteries.* Angewandte Chemie International Edition, 2005. **44**(43): p. 7085-7089.

[119] Poizot, P., S. Laruelle, S. Grugeon, L. Dupont, and J.M. Tarascon, *Nano-sized transition-metal oxides as negative-electrode materials for lithium-ion batteries.* Nature, 2000. **407**(6803): p. 496-499.

[120] Peng, C., B. Chen, Y. Qin, S. Yang, C. Li, Y. Zuo, S. Liu, and J. Yang, *Facile Ultrasonic Synthesis of CoO Quantum Dot/Graphene Nanosheet Composites with High Lithium Storage Capacity.* Acs Nano, 2012. **6**(2): p. 1074-1081.

[121] Koudriachova, M.V., N.M. Harrison, and S.W. de Leeuw, *Effect of Diffusion on Lithium Intercalation in Titanium Dioxide.* Physical Review Letters, 2001. **86**(7): p. 1275-1278.

[122] Wagemaker, M., A.P.M. Kentgens, and F.M. Mulder, *Equilibrium lithium transport between nanocrystalline phases in intercalated TiO2 anatase.* Nature, 2002. **418**(6896): p. 397-399.

[123] Ji, L., Z. Lin, M. Alcoutlabi, and X. Zhang, *Recent developments in nanostructured anode materials for rechargeable lithium-ion batteries.* Energy & Environmental Science, 2011. **4**(8): p. 2682-2699.

[124] Park, M.-S., G.-X. Wang, Y.-M. Kang, D. Wexler, S.-X. Dou, and H.-K. Liu, *Preparation and Electrochemical Properties of SnO2 Nanowires for Application in Lithium-Ion Batteries.* Angewandte Chemie, 2007. **119**(5): p. 764-767.

[125] Kim, H. and J. Cho, *Hard templating synthesis of mesoporous and nanowire SnO2lithium battery anode materials.* Journal of Materials Chemistry, 2008. **18**(7): p. 771-775.

[126] Han, S., B. Jang, T. Kim, S.M. Oh, and T. Hyeon, *Simple Synthesis of Hollow Tin Dioxide*

Microspheres and Their Application to Lithium-Ion Battery Anodes. Advanced Functional Materials, 2005. **15**(11): p. 1845-1850.

[127] Lou, X.W., Y. Wang, C. Yuan, J.Y. Lee, and L.A. Archer, *Template-Free Synthesis of SnO2 Hollow Nanostructures with High Lithium Storage Capacity.* Advanced Materials, 2006. **18**(17): p. 2325-2329.

[128] Wu, H.B., J.S. Chen, X.W. Lou, and H.H. Hng, *Synthesis of SnO2 Hierarchical Structures Assembled from Nanosheets and Their Lithium Storage Properties.* The Journal of Physical Chemistry C, 2011. **115**(50): p. 24605-24610.

[129] Lou, X.W., C.M. Li, and L.A. Archer, *Designed Synthesis of Coaxial SnO2@carbon Hollow Nanospheres for Highly Reversible Lithium Storage.* Advanced Materials, 2009. **21**(24): p. 2536-2539.

[130] Yang, Z., D. Choi, S. Kerisit, K.M. Rosso, D. Wang, J. Zhang, G. Graff, and J. Liu, *Nanostructures and lithium electrochemical reactivity of lithium titanites and titanium oxides: A review.* Journal of Power Sources, 2009. **192**(2): p. 588-598.

[131] Kavan, L., J. Rathouský, M. Grätzel, V. Shklover, and A. Zukal, *Surfactant-Templated TiO2 (Anatase): Characteristic Features of Lithium Insertion Electrochemistry in Organized Nanostructures.* The Journal of Physical Chemistry B, 2000. **104**(50): p. 12012-12020.

[132] Fu, L.J., H. Liu, H.P. Zhang, C. Li, T. Zhang, Y.P. Wu, and H.Q. Wu, *Novel TiO2/C nanocomposites for anode materials of lithium ion batteries.* Journal of Power Sources, 2006. **159**(1): p. 219-222.

[133] Wang, D., D. Choi, J. Li, Z. Yang, Z. Nie, R. Kou, D. Hu, C. Wang, L.V. Saraf, J. Zhang, I.A. Aksay, and J. Liu, *Self-Assembled TiO2–Graphene Hybrid Nanostructures for Enhanced Li-Ion Insertion.* Acs Nano, 2009. **3**(4): p. 907-914.

[134] Wang, Z. and X.W. Lou, *TiO2 Nanocages: Fast Synthesis, Interior Functionalization and Improved Lithium Storage Properties.* Advanced Materials, 2012. **24**(30): p. 4124-4129.

[135] Liu, B., D. Deng, J.Y. Lee, and E.S. Aydil, *Oriented single-crystalline TiO(2) nanowires on titanium foil for lithium ion batteries.* Journal of Materials Research, 2010. **25**(8): p. 1588-1594.

[136] Li, F., Q.-Q. Zou, and Y.-Y. Xia, *CoO-loaded graphitable carbon hollow spheres as anode materials for lithium-ion battery.* Journal of Power Sources, 2008. **177**(2): p. 546-552.

[137] Wang, B., X.-L. Wu, C.-Y. Shu, Y.-G. Guo, and C.-R. Wang, *Synthesis of CuO/graphene nanocomposite as a high-performance anode material for lithium-ion batteries.* Journal of Materials Chemistry, 2010. **20**(47): p. 10661-10664.

[138] Sun, Y., X. Hu, W. Luo, and Y. Huang, *Self-Assembled Hierarchical MoO2/Graphene Nanoarchitectures and Their Application as a High-Performance Anode Material for Lithium-Ion Batteries.* Acs Nano, 2011. **5**(9): p. 7100-7107.

[139] Lee, S.-H., Y.-H. Kim, R. Deshpande, P.A. Parilla, E. Whitney, D.T. Gillaspie, K.M. Jones, A.H. Mahan, S. Zhang, and A.C. Dillon, *Reversible Lithium-Ion Insertion in Molybdenum Oxide Nanoparticles.* Advanced Materials, 2008. **20**(19): p. 3627-3632.

[140] Taberna, P.L., S. Mitra, P. Poizot, P. Simon, and J.M. Tarascon, *High rate capabilities Fe3O4-based Cu nano-architectured electrodes for lithium-ion battery applications.* Nat Mater, 2006. **5**(7): p. 567-573.

[141] Xu, X., R. Cao, S. Jeong, and J. Cho, *Spindle-like Mesoporous α-Fe2O3 Anode Material Prepared from MOF Template for High-Rate Lithium Batteries.* Nano Letters, 2012. **12**(9): p. 4988-4991.

[142] Lin, Y.-M., P.R. Abel, A. Heller, and C.B. Mullins, *α-Fe2O3 Nanorods as Anode Material for Lithium Ion Batteries.* The Journal of Physical Chemistry Letters, 2011. **2**(22): p. 2885-2891.

[143] Han, F., D. Li, W.-C. Li, C. Lei, Q. Sun, and A.-H. Lu, *Nanoengineered Polypyrrole-Coated Fe2O3@C Multifunctional Composites with an Improved Cycle Stability as Lithium-Ion Anodes.* Advanced Functional Materials, 2013. **23**(13): p. 1692-1700.

[144] Zhong, L., A. Xie, and L. Mangolini, *Silicon Quantum Dots-Carbon Nanotube Composite as Anode Material for Lithium Ion Battery.* MRS Online Proceedings Library, 2013. **1540**: p. null-null.

[145] Obrovac, M.N. and V.L. Chevrier, *Alloy Negative Electrodes for Li-Ion Batteries.* Chemical Reviews, 2014. **114**(23): p. 11444-11502.

[146] Nguyen, B.P.N., S. Chazelle, M. Cerbelaud, W. Porcher, and B. Lestriez, *Manufacturing of industry-relevant silicon negative composite electrodes for lithium ion-cells.* Journal of Power Sources, 2014. **262**(0): p. 112-122

[147] Pillot, C., *The rechargeable battery market and main trends 2012-2025*, in *30th International Battery Seminar & Exhibit*2013, Avicenne Energy.

[148] Li, X., Y. He, S.S. Talukdar, and M.T. Swihart, *Process for preparing macroscopic quantities of brightly photoluminescent silicon nanoparticles with emission spanning the visible spectrum.* Langmuir, 2003. **19**: p. 8490-8496.

[149] Kortshagen, U., R.J. Anthony, R. Gresback, Z. Holman, R.K. Ligman, C.-Y. Liu, L. Mangolini, and S.A. Campbell, *Plasma synthesis of group IV quantum dots for luminescence and photovoltaic applications.* Pure & Appl. Chem., 2008. **80**(9): p. 1901-1908.

[150] Mangolini, L., E. Thimsen, and U. Kortshagen, *High-yield plasma synthesis of luminescent silicon nanocrystals.* Nano Letters, 2005. **5**(4): p. 655-659.

[151] Rosenband, V., A. Garbar, C. Sokolinsky, D. Lekhtman, F. De La Vega, and T. Zak, *Process for producing ultra-fine powder of crystalline silicon*, 2009, Cima Nanotech.

[152] Johnson, D., J. Tudor, A.W. Kynaston-Pearson, and A.B. Godfrey, *Purification method*, 2008, Qinetiq Nanomaterials.

[153] Chockla, A.M., K.C. Klavetter, C.B. Mullins, and B.A. Korgel, *Tin-Seeded Silicon Nanowires for High Capacity Li-Ion Batteries.* Chemistry of Materials, 2012. **24**(19): p. 3738-3745.

[154] Chockla, A.M., J.T. Harris, V.A. Akhavan, T.D. Bogart, V.C. Holmberg, C. Steinhagen, C.B. Mullins, K.J. Stevenson, and B.A. Korgel, *Silicon Nanowire Fabric as a Lithium Ion Battery Electrode Material.* Journal of the American Chemical Society, 2011. **133**(51): p. 20914-20921.

[155] Maranchi, J. P., A. F. Hepp, A. G. Evans, N. T. Nuhfer, and P. N. Kumta, "*Interfacial properties of the a-Si/Cu: active–inactive thin-film anode system for lithium-ion batteries.*" Journal of the Electrochemical Society, 2006, **153**, no. 6: p. 1246-1253.

Chapter 2. Spray Pyrolysis of Yolk–Shell Particles and Their Use as Anode Materials

ABSTRACT:

We demonstrate the synthesis of yolk–shell particles using spray-pyrolysis, a technique with proven scalability to industrial production level. Nickel oxide (shell)–silicon (yolk) particles are produced using a single-step aerosol reaction from a mixture of commercial, off-the-shelf precursors. After coating and annealing in the presence of polyvinylpyrrolidone, the nickel oxide shell is converted into a porous nickel cage enclosing the silicon particles. The polymer decomposition leads to the formation of an amorphous carbon layer surrounding the nickel cage. This structure maintains a high specific discharge capacity after more than 100 cycles (~ 1400 mAh/g at the 110th cycle with a 0.5 C discharge rate, on a silicon basis) when used as anode for lithium-ion batteries.

2.1 Introduction

As discussed in Chapter 1, silicon presents many challenges to its utilization for energy storage applications due to its structural instability upon lithiation, its low electrical conductivity and its tendency to form a mechanically unstable and electrically insulating solid electrolyte interphase (SEI) [1]. Some of these problems can be addressed by reducing the size of the silicon particles [2] and

[3], by combining it with conductive materials [4], [5], [6], [7], [8], [9] and [10] and by using additives to the electrolyte such as fluoroethylene or vinylene carbonate (FEC, VC), which help forming a thinner and more stable SEI [11], [12] and [13]. A silicon-containing yolk–shell structure addresses these issues simultaneously by accommodating the volume expansion of the core during lithiation, by enhancing the electrical conductivity of the material and by preventing the direct contact between silicon and the electrolyte [14]. Yolk–shell structures are typically realized using processes that require precise experimental conditions and whose scalability remains to be demonstrated. Under the appropriate conditions spray-pyrolysis reactors can produce hollow nanoparticles [15] and [16]. For instance nickel-oxide shells are easily produced by spray pyrolysis [17]. The simple addition of commercial silicon particles to the nickel oxide precursor mixture allows encasing the silicon particles into a nickel oxide shell. We have found that the nickel oxide shell can be easily reduced to metallic nickel using thermal annealing in the presence of a polymer precursor. Thermal annealing enhances the electrical conductivity of the structure and leads to the decomposition of the polymer and to the formation of an amorphous carbon layer surrounding the nickel shell which improves the anode stability.

2.2 Materials and Methods

A mixture of 500 mg of $NiCl_2 \cdot 6H_2O$ (Sigma-Aldrich 31462-1KG-R) and 100 mg of Si nanopowders (< 100 nm, Sigma-Aldrich 633097-25G) are dissolved in 60 ml

of DI water by probe sonication. The solution is aerosolized using a collision nebulizer from BGI, Inc. Argon is used as carrier gas. The aerosol is carried through a 2″ quartz tube placed in a tube furnace set at a temperature of 800 °C. The residence time in the furnace is ~ 1 s. NiO (shell)–Si (yolk) particles form during the high-temperature treatment. The nanoparticles are first removed from the gas stream using multiple bubblers containing DI water, then washed three times in ethanol and vacuum dried.

The NiO–Si particles are dispersed in ethanol via sonication and drop cast onto copper foil, resulting in ~ 10 μm thick layers. These coatings have been tested directly in a half-cell battery. Alternatively, the coatings are treated with two different approaches before testing. In a first approach, the coated substrate is annealed at 190 °C under hydrogen flow for 45 min at a pressure of 0.2 Torr to reduce nickel oxide to metallic nickel [18]. In a second approach, polyvinylpyrrolidone (PVP) (Sigma-Aldrich PVP-40) is dissolved in ethanol and added to the NiO–Si solution before coating. The coating is annealed at 500 °C for 30 min under argon flow.

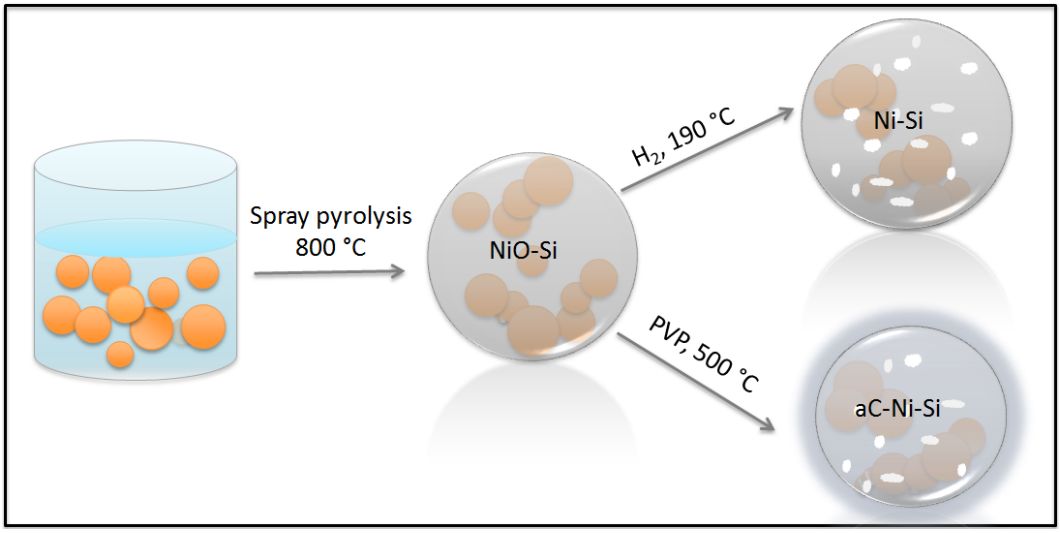

Figure 2.1 Schematic illustration of the synthesis route of NiO@Si, Ni@Si, aC@Ni@Si, white dots represent empty space while, yellow spheres represent silicon nanoparticles.

Material characterization has been performed via scanning (SEM, Nova NanoSEM 450) and transmission (Philips CM300 300 kV with EDS system) electron microscopy, Raman (Horiba LabRam, 532 nm excitation) and X-ray diffraction (PANalytical EMPYREAN with CuKα source). The anodes are assembled into CR2032 coin cell batteries with lithium foil as counter electrode. No other binder is added. The typical weight loading is 0.3–0.5 mg/cm^2. 1 M LiPF6 in ethylene carbonate/diethyl carbonate (1:1 v/v) is used as the electrolyte (MTI, part number: EQ-Be-LiPF6). 10 wt.% of FEC (Solvay S.A., Belgium) is added to the electrolyte for selected batteries. The separator film is purchased from MTI. All cells are cycled between 0.01 V and 1.5 V using an Arbin potentiostat. Cyclic voltammetry (CV) is performed at a sweeping rate of 0.05 mV/s.

2.3 Results and Discussion

Figure 2.2.a and b respectively shows nanoparticles synthesized using nickel chloride (a) and a mixture of nickel chloride and silicon particles (b) as precursors. The NiO particle size is below 500 nm and it appears to be empty with a shell thickness of roughly 20 nm. Structural characterization confirms that the shell is composed of nickel oxide. Figure 2.2b indicates that some other particle is present within the shell. The elemental mapping shown in Figure 2.2c through Figure 2.2e confirms that there is a silicon particle trapped within a nickel oxide shell and suggests that there is an empty buffer volume between the core and the shell materials, i.e. the particle has a yolk–shell structure.

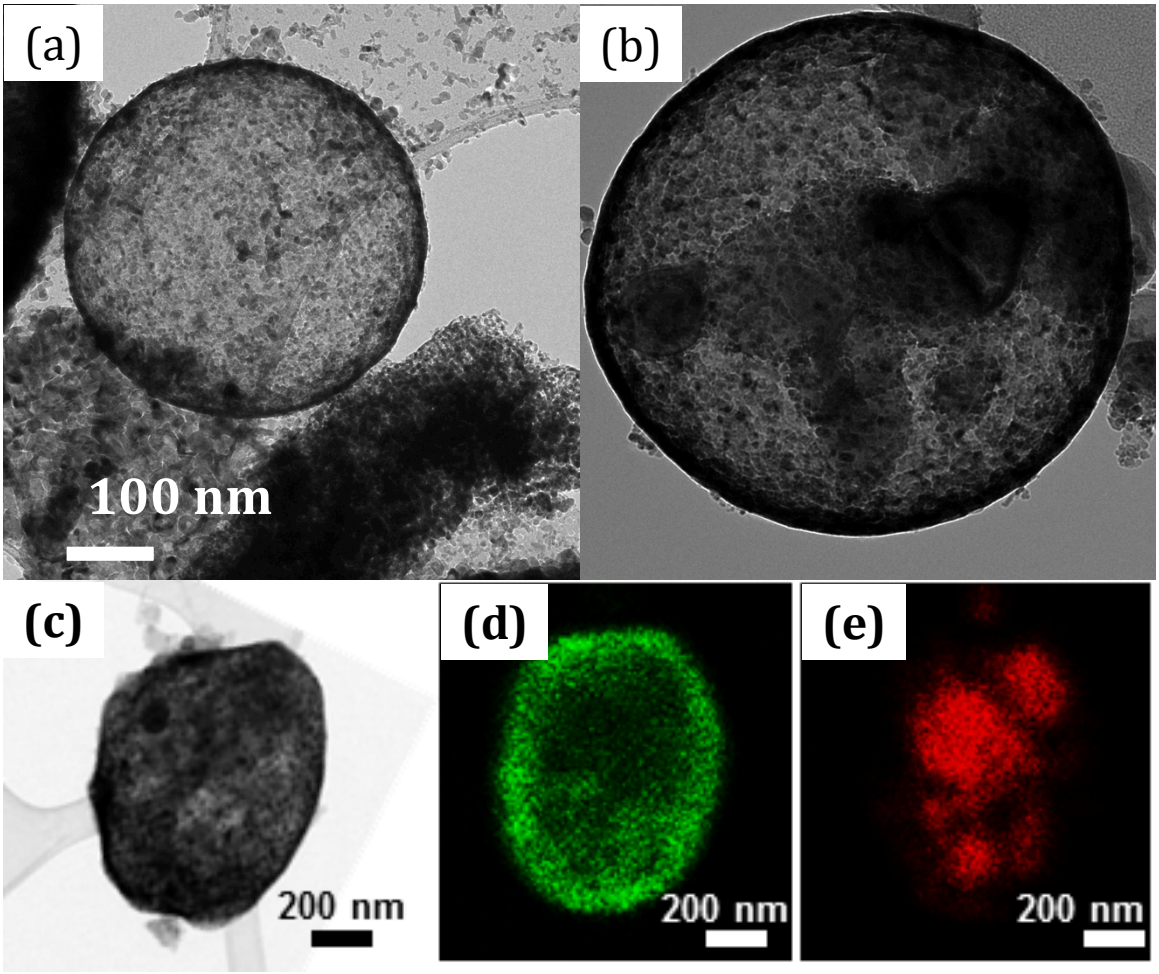

Figure 2.2 TEM of (a) an empty NiO nanoshell and of (b) a yolk–shell silicon–nickel oxide nanoparticle. (c) TEM of a yolk–shell particle with corresponding elemental mapping for nickel (d) and silicon (e).

After synthesis, the particles are coated onto a copper substrate and annealed using the techniques described above. In Figure 2.3a) we show the SEM of nanoparticles reduced in hydrogen. The outer shell appears to be porous and a smaller particle is distinguishable within this cage. When reduction is performed in the presence of PVP additive, the outer layer is not porous, as shown in Figure 2.3b. We have performed a gentle mechanical treatment (via mortar and pestle) on the sample shown in Figure 2.3b to crack the particles and inspect their inner

structure (see Figure 2.3c). After thermal reduction, an empty buffer volume is still present between the silicon core and the nickel shell. Figure 2.3d is the morphology of typical electrode materials. The electrode materials are uniformly distributed and there are porous.

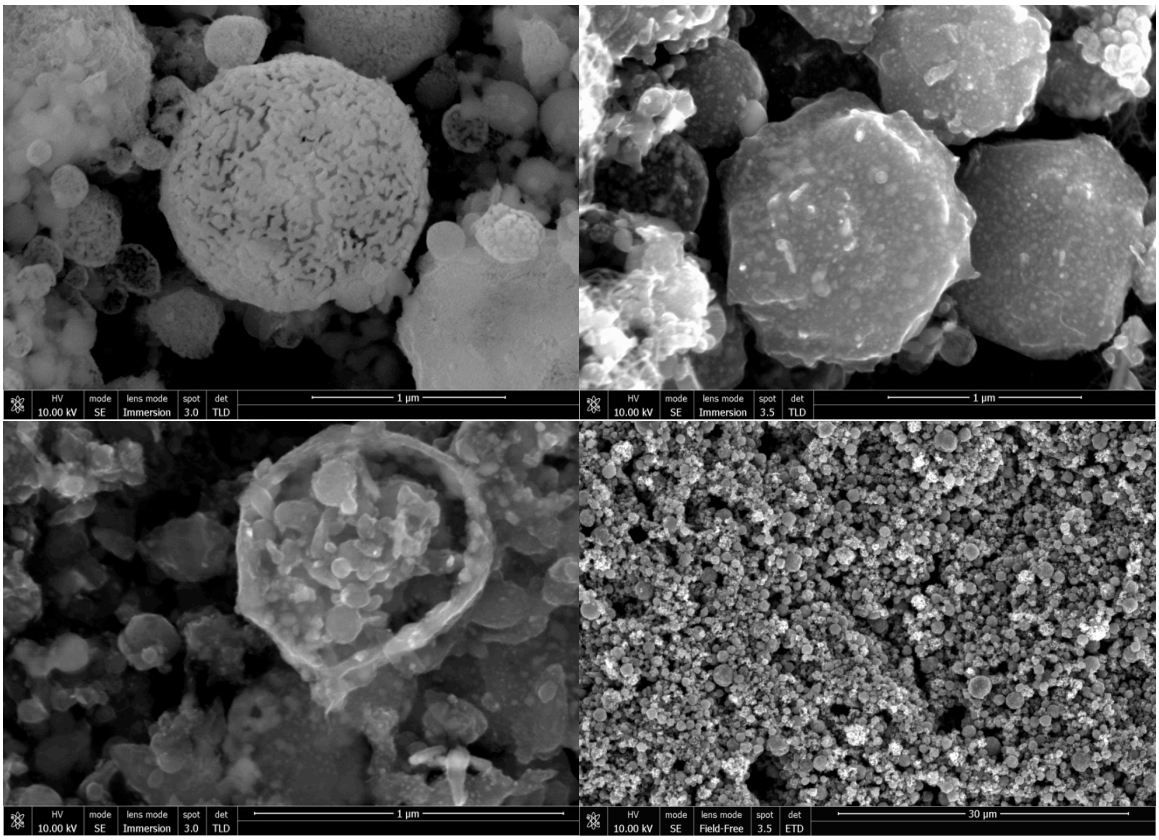

Figure 2.3 (a) SEM of nanoparticle reduced in hydrogen (Ni–Si nanoparticles). (b) SEM of nanoparticles reduced in the presence of PVP (aC–Ni–Si nanoparticles). (c) SEM image of a gentle mechanical treated aC-Ni-Si nanoparticles. (d) zoom out of (b) uniform distribution of the electrode morphology.

XRD spectra for the particles before annealing (NiO–Si), after annealing in hydrogen (Ni–Si) and after annealing in the presence of PVP (aC–Ni–Si) are shown in Figure 2.4 a). The peak assignment is based on the Inorganic Crystal Structure Database (FIZ Karlsruhe). These spectra confirm that NiO is reduced

to nickel metal in both cases. Thermal annealing in the presence of PVP leads to both the reduction of the nickel oxide and the concurrent decomposition of the polymer into an amorphous carbon layer. This conclusion is supported by Raman characterization, shown Figure 2.4b, which confirms the presence of two amorphous carbon peaks in the 1300~1600 cm-1 range [19]. Figure 2.4b suggests that the carbon layer clogs the holes in the nickel shell effectively sealing the cage structure. Additional SEM characterization performed after cycling indicates that the particles are uniformly coated by the SEI layer without any indication of cracking of the shell.

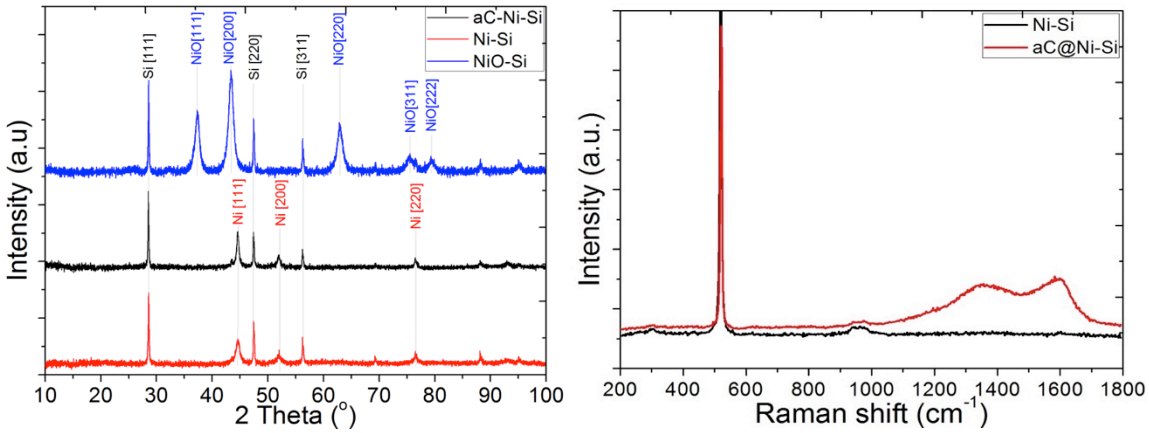

Figure 2.4 (left) XRD of NiO–Si, Ni–Si and aC–Ni–Si nanoparticles. (right) Raman spectrum for these particle

The results of the electrochemical testing on the NiO–Si, Ni–Si and aC–Ni–Si structures are shown in Figure 2.5 For the NiO–Si case, the capacity is calculated using the total coating weight since both nickel oxide and silicon undergo lithiation [20]. For the case of Ni–Si and aC–Ni–Si, the capacities are calculated using the silicon weight only, since nickel does not participate in the lithiation reaction. The silicon weight is calculated using a 4:3 weight ratio for Ni:Si, as determined via SEM–EDS. This weight fraction is consistent with the precursor weight ratio of 5:1 for $NiCl_2$·6H2O:SiNPs, under the assumption of full precursor consumption (which gives a 1.56:1 NiO:Si ratio and a 1.22:1 Ni:Si ratio after reduction). The amorphous carbon layer for the aC–Ni–Si structure contributes to ~ 10% of the coated material weight, as determined by carefully measuring the weight of the active layer with and without PVP addition to the coating. To fully clarify the role of the amorphous carbon layer on the device performance, we have also prepared an additional structure based on a dispersion of silicon nanoparticles and PVP, which has been annealed after coating onto copper foil using the same procedure as for the aC–Ni–Si structure.

There are literatures shown TGA curve for PVP annealed in an insert environment which may not applicable in our case. Thus, we carefully measured PVP residue weight ratio in our electrode: a) a piece of copper foil substrate was weighted, weight is given in Table 2.1; b) 3:1 weight ratio PVP:NiO-Si was drop-casted on the same piece of copper foil and dried at 100 °C, copper foil +

PVP:NiO-Si was weighted; c) annealed at 500 °C in argon for 30 minutes, weighted.

Table 2. 1 Typical weight (in miligram) for materials used in the electrode preparation.

	Cu Foil	Cu foil + PVP:NiO-Si	Cu foil + aC-Ni-Si	PVP	NiO-Si	Si	Ni	Amorphous Carbon
Weight (mg)	111.9	128.2	116.1	12.2	4.1	1.52	2.02	0.66

Calculation is done as following. Briefly, weight of PVP and NiO-Si can be calculated based on their 3:1 weight ratio. We get weight of PVP is 12.2 mg, and NiO-Si weight is 4.1 mg. From EDS data shown in Figure S1, Ni:Si element weight ratio is ~4:3, thus, NiO:Si weight ratio is 5.1:3 (NiO:Ni atomic weight 74:58). In 4.1 mg of NiO-Si, silicon weight is calculated to be 1.52 mg, while NiO is 2.58 mg. Assume there is no wasting during annealing, then metal nickel weight is 2.02 mg. As measured, the total weight for aC-Ni-Si is 4.2mg, which 2.02 mg from nickel and 1.52 mg from silicon, the rest 0.66 mg is attribution of amorphous carbon from PVP residue. Finally, we computed the weight ratio of PVP residue out of PVP after annealing is (0.66/12.2)*100% = 5.41%.

In Figure 2.5a, we show the results of galvanostatic charging and discharging at 0.1 C. The material annealed in the presence of PVP shows the best specific capacity and stability, while the decay is faster for both the Ni–Si anode and for the anode based on the NiO–Si structure. The poor performance of the NiO–Si electrode is likely due to the fact that the oxide shell hinders charge collection to

the external circuit. Moreover, NiO undergoes expansion and fragmentation during cycling [21]. We attribute the fast capacity decaying for the case of the Ni–Si anode to the fact that the electrolyte penetrates inside the nickel cage directly exposing the silicon particles. SEM performed on a Ni–Si battery which has been disassembled after the first cycle shows small holes on the particle surface, confirming that the electrolyte penetrates through the holes and is in direct contact with the silicon particles. The aC–Ni–Si structure has the best discharge capacity and stability performance. We attribute this to the excellent electrical conductivity provided by the nickel cage, to the presence of an amorphous carbon layer which prevents the direct contact between the silicon and the electrolyte, and to the presence of a buffer volume between the silicon particle and the nickel cage. The best structure has a first cycle discharge capacity of 3360 mAh/g with a 26% capacity loss after the first cycle. The discharge capacity at the 50th cycle is 2150 mAh/g. The battery realized using a dispersion containing only silicon particle and PVP shows fast capacity decay, suggesting that the presence of amorphous carbon alone is not sufficient at improving the anode performance. Figure 2.5b shows the results of cyclic voltammetry measurements for the first and the second cycle of aC–Ni–Si battery. The lithiation peak at 0.18 V is more obvious in the 2nd cycle, a behavior which has been correlated with structural changes in the silicon particles [22] and [23]. Typical delithiation peaks at 0.36 V and 0.53 V are clearly observed [24]. Figure 2.5(e) depicts the 1^{st} and 2^{nd} Galvanostatic charge/discharge profiles of Ni-Si,

NiO-Si, aC-Ni-Si cells. The plateau around 0.2V is due silicon lithiation, while plateau ~0.5V reflects silicon delithiation. One things worth mention is: in NiO-Si electrode, NiO can be lithiated and form Li_2O and Ni with a plateau (green line) at ~0.6V. The reason that this plateau disappeared in 2^{nd} cycle is due to Li_2O, Ni delithiation peak is at 2.1V when the battery is tested in a range of 0.01V-1.5V. Our focus is not focus on NiO-Li system in this case. Figure 2.5c shows the battery performance for the aC–Ni–Si material cycled at higher rate. The initial discharge capacity is 3240 mAh/g, and the average discharge capacity is 2560 mAh/g during the first 10 cycles at 0.1 C and 1400 mAh/g for the next 100 cycles at 0.5 C.

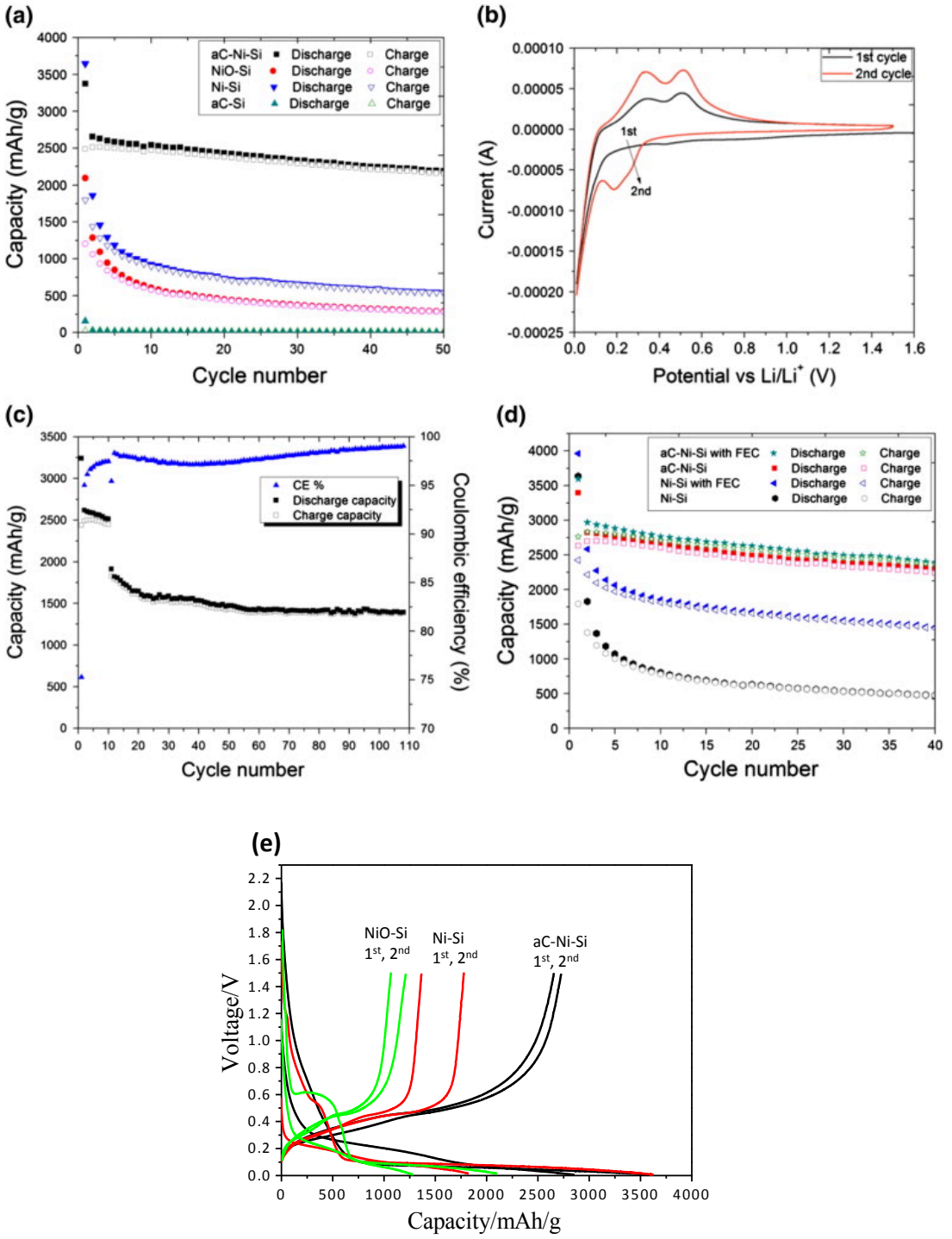

Figure 2.5 (a) Discharge and charge capacities for the aC–Si, NiO–Si, Ni–Si and aC–Ni–Si particles. (b) CV measurement for the aC–Ni–Si battery. (c) Discharge and charge capacities and coulombic efficiency for the aC–Ni–Si nanoparticles with a cycling rate of 0.1 C for the first 10 cycles and with a 0.5 C for the next 100 cycles. (d) Role of FEC addition on the capacities of the Ni–Si and aC–Ni–Si structures. (e) 1st and 2nd Galvanostatic charge/discharge profile for NiO-Si (green lines), Ni-Si (red lines), aC-Ni-Si cells (black lines).

The addition of FEC to the electrolyte improves the stability of silicon-based anodes by forming a thinner and more stable SEI layer on the silicon surface [11], [12] and [13]. For example, Nguyen et.al reported 15% FEC additive to the electrolyte help formed thinner SEI layer without crack after more than 20 cycles[26]. We have added FEC to our electrolyte formulation for the Ni–Si and the aC–Ni–Si structures. As shown in Figure 2.5d, at the 40th cycle the discharge capacities for the Ni–Si anode are ~ 1450 mAh/g with FEC and ~ 500 mAh/g without FEC. However, in the case of aC–Ni–Si anode the discharge capacity shows little to no change (~ 2300 mAh/g at the 40th cycle) upon FEC addition. This behavior is consistent with the fact that the electrolyte is not in direct contact with silicon for the aC–Ni–Si structure.

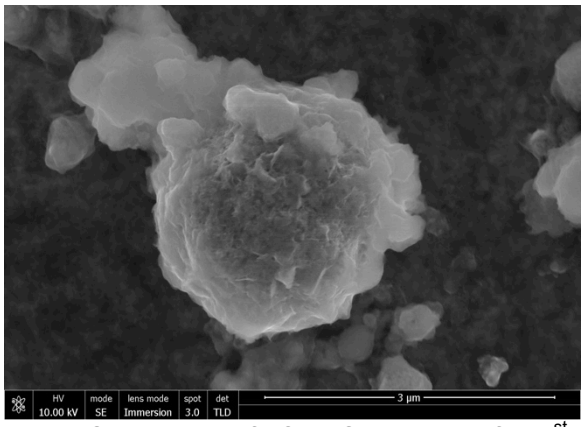

Figure 2.6 SEM image of aC-Ni-Si particles after 1st cyle.

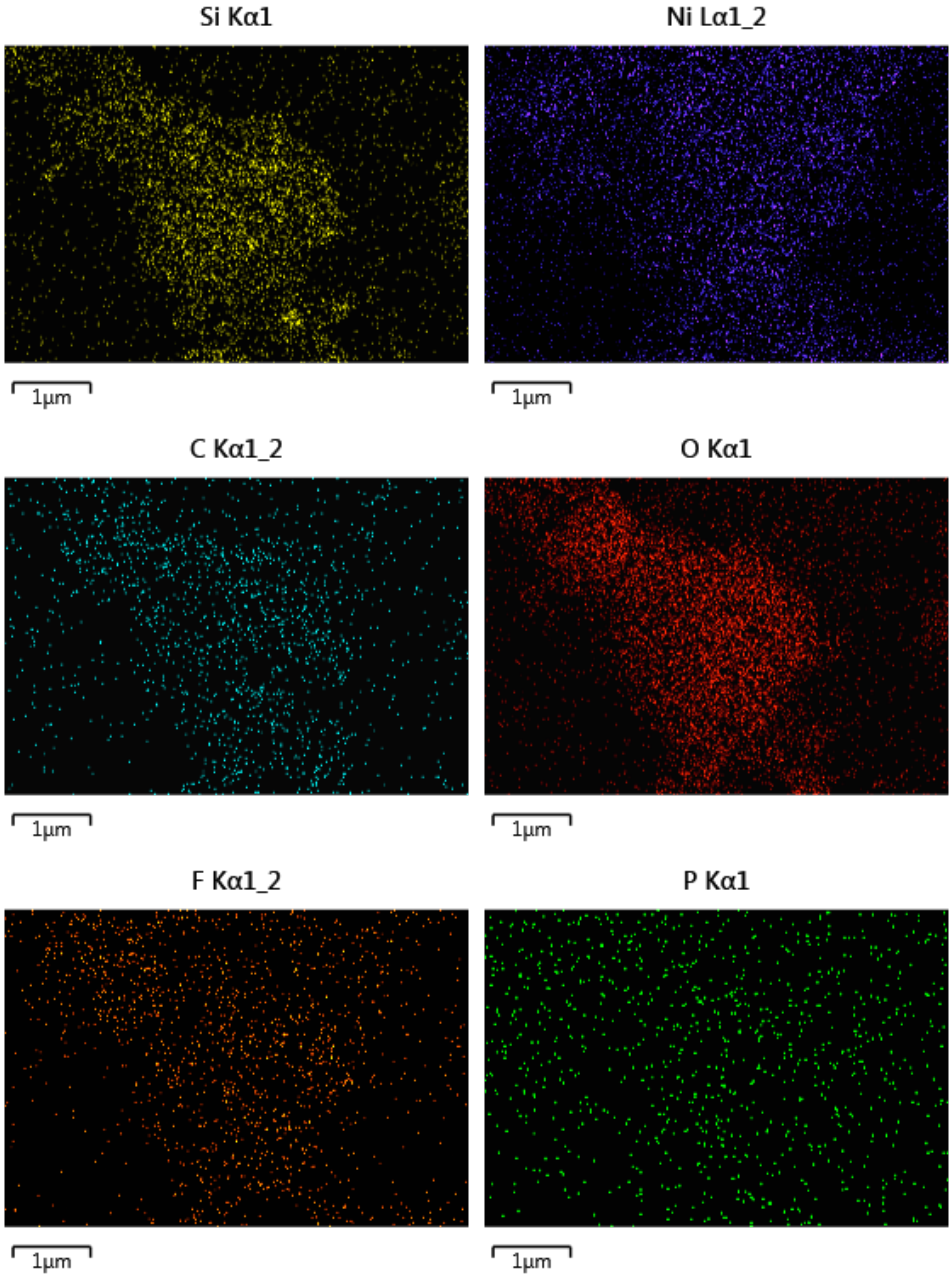

Figure 2.7 Elemental mapping for the aC-Ni-Si particle shown in Figure 2.6.

We performed SEM and EDS on electrodes after 1 cyles, as shown in Figure 2.6. and Figure 2.7. The battery was opened in an argon filled glove-box, the electrode was washed with acetonitrile for 3 times. Figure 2.6 SEM image potray

the ~2um size aC-Ni-Si was maitaining its shape without cracking and SEI residue is outside the particle. Besides, EDS elemental mappings for this particle were exhibited in Figure 2.7. EDS mapping indicates that silicon nanoparticles are inside of aC-Ni shell. And the SEI indicator, in this case fluoride, is mainly distributed around nickel and it's the SEI residue.

For aC–Ni–Si electrode shown in Figure 2.5c, the first cycle discharge capacity value of 3360 mAh/g on a silicon basis corresponds to 1630 mAh/g on a total mass basis. The capacity at the 50th cycle (2150 mAh/g on a silicon basis) is 810 mAh/g on a total mass basis. Even when accounting for the total coated weight, the capacity is comparable to that obtained from other silicon-containing anode structures [25]. Moreover, the high conductivity of nickel may allow using this material in combination with light-weight, flexible substrates with less stringent conductivity requirement compared to copper foil, leading to improvements in battery energy density. While these results are promising, we should point out that the encapsulation process during the spray pyrolysis step is not perfect. When performing TEM and SEM analysis it is possible to find silicon particles which are not protected by a nickel oxide shell and empty nickel oxide shells as well. Future optimization efforts, which go beyond the scope of this contribution, will target this issue and explore its influence on device performance.

2.4 Conclusion

We have demonstrated that spray pyrolysis, which is well-known to be scalable to large production levels, can be used for the direct synthesis of yolk–shell nanoparticles. We have shown that nickel oxide–silicon particles can be produced using off-the-shelf precursors and post-processed via thermal annealing to give an amorphous carbon–nickel–silicon shell–shell–yolk structure. The combination of the amorphous carbon layer with the nickel cage greatly enhances the stability of the structure upon electrochemical cycling. We expect this approach to be applicable to other materials and to be relevant to any material that experiences large volume changes during electrochemical energy storage. This work suggest that even complex structures such as yolk-shell nanoparticles can be produced via scalable techniques, which is important for the development of an economically viable alternative anode structure.

Reference

[1] H.Wu,G.Chan,J.W.Choi,I.Ryu,Y.Yao,M.T.McDowell,S.W.Lee,A.Jackson,Y.Yang, L.B. Hu, Y. Cui, Stable cycling of double-walled silicon nanotube battery anodes through solid-electrolyte interphase control, Nat. Nanotechnol. 7 (2012) 309–314.

[2] J.P. Maranchi, A.F. Hepp, P.N. Kumta, High capacity, reversible silicon thin-film anodes for lithium-ion batteries, Electrochem. Solid-State Lett. 6 (2003) A198–A201.

[3] X.H.Liu, L.Zhong,S.Huang,S.X.Mao,T.Zhu,J.Y.Huang,Size-dependentfractureof silicon nanoparticles during lithiation, ACS Nano 6 (2012) 1522–1531.

[4] B. Johansson. A broadened typology on energy and security. Energy,53, (2013) 199-205.

[5] Y.H.Zhu,W.Liu,X.Y.Zhang,J.C.He,J.T.Chen,Y.P.Wang,T.B.Cao,Directingsilicon- graphene self-assembly as a core/shell anode for high-performance lithium-ion batteries, Langmuir 29 (2013) 744–749.

[6] L. Luo, J. Wu, J. Luo, J. Huang, V.P. Dravid, Dynamics of electrochemical lithiation delithiation of graphene-encapsulated silicon nanoparticles studied by in-situ TEM, Sci. Rep. 4 (2014) 1–4.

[7] W. Wang, P.N. Kumta, Nanostructured hybrid silicon/carbon nanotube heterostructures: reversible high-capacity lithium-ion anodes, ACS Nano 4 (2010) 2233–2241.

[8] S.L. Chou, Y. Zhao, J.Z. Wang, Z.X. Chen, H.K. Liu, S.X. Dou, Silicon/single-walled carbon nanotube composite paper as a flexible anode material for lithium ion batteries, J. Phys. Chem. C 114 (2010) 15862–15867.

[9] L.F. Cui, L.B. Hu, J.W. Choi, Y. Cui, Light-weight free-standing carbon nanotube- silicon films for anodes of lithium ion batteries, ACS Nano 4 (2010) 3671–3678.

[10] K. Evanoff, J. Benson, M. Schauer, I. Kovalenko, D. Lashmore, W.J. Ready, G. Yushin, Ultra strong silicon-coated carbon nanotube nonwoven fabric as a multifunctional lithium-ion battery anode, ACS Nano 6 (2012) 9837–9845.

[11] C.C. Nguyen, B.L. Lucht, Comparative study of fluoroethylene carbonate and vinylene carbonate for silicon anodes in lithium ion batteries, J. Electrochem. Soc. 161 (2014) A1933–A1938

[12] N.-S. Choi, K.H. Yew, K.Y. Lee, M. Sung, H. Kim, S.-S. Kim, Effect of fluoroethylene carbonate additive on interfacial properties of silicon thin-film electrode, J. Power Sources 161 (2006) 1254–1259

[13] Y.-M. Lin, K.C. Klavetter, P.R. Abel, N.C. Davy, J.L. Snider, A. Heller, C.B. Mullins, High performance silicon nanoparticle anode in fluoroethylene carbonate-based electro- lyte for Li-ion batteries, Chem. Commun. 48 (2012) 7268–7270.

[14] N. Liu, H. Wu, M.T. McDowell, Y. Yao, C.M. Wang, Y. Cui, A yolk–shell design for stabilized and scalable Li-ion battery alloy anodes, Nano Lett. 12 (2012) 3315–3321.

[15] S.C. Zhang, G.L. Messing, M. Borden, Synthesis of solid, spherical zirconia particles by spray pyrolysis, J. Am. Ceram. Soc. 73 (1990) 61–67.

[16] G.L. Messing, S.C. Zhang, G.V. Jayanthi, Ceramic powder synthesis by spray-pyrolysis, J. Am. Ceram. Soc. 76 (1993) 2707–2726.

[17] S.H.Choi, Y.C.Kang,Ultrafastsynthesisofyolk–shellandcubicNiOnanopowdersand application

in lithium ion batteries, ACS Appl. Mater. Interfaces 6 (2014) 2312–2316.

[18] J.T. Richardson, R. Scates, M.V. Twigg, X-ray diffraction study of nickel oxide reduction by hydrogen, Appl. Catal. A Gen. 246 (2003) 137–150.

[19] A.C. Ferrari, J. Robertson, Interpretation of Raman spectra of disordered and amorphous carbon, Phys. Rev. B 61 (2000) 14095–14107.

[20] P. Poizot, S. Laruelle, S. Grugeon, L. Dupont, J.M. Tarascon, Nano-sized transition- metal oxides as negative-electrode materials for lithium-ion batteries, Nature 407 (2000) 496–499.

[21] X.H. Huang, J.P. Tu, C.Q. Zhang, F. Zhou, Hollow microspheres of NiO as anode materials for lithium-ion batteries, Electrochim. Acta 55 (2010) 8981–8985.

[22] A. Magasinski, P. Dixon, B. Hertzberg, A. Kvit, J. Ayala, G. Yushin, High-performance lithium-ion anodes using a hierarchical bottom-up approach, Nat. Mater. 9 (2010) 353–358.

[23] X. Feng, J. Yang, P. Gao, J. Wang, Y. Nuli, Facile approach to an advanced nanoporous silicon/carbon composite anode material for lithium ion batteries, RSC Adv. 2 (2012) 5701–5706.

[24] C.K. Chan, H.L. Peng, G. Liu, K. McIlwrath, X.F. Zhang, R.A. Huggins, Y. Cui, High-performance lithium battery anodes using silicon nanowires, Nat. Nanotechnol. 3(2008) 31–35.

[25] L. Zhong, J. Guo, L. Mangolini, A stable silicon anode based on the uniform dispersion of quantum dots in a polymer matrix, J. Power Sources 273 (2015) 638–644.

[26] Nguyen, Cao Cuong, and Brett L. Lucht., Journal of The Electrochemical Society 161.12 (2014): A1933-A1938.

Chapter 3. A stable silicon anode based on the uniform dispersion of quantum dots in a polymer matrix

ABSTRACT:

We propose a novel approach to the fabrication of silicon-containing anodes for lithium-ion batteries. Our approach is based on a liquid dispersion comprising of silicon quantum dots, carbon nanotubes and polyvinylpirrolidone (PVP) as a polymer additive. Coating of this dispersion onto copper foil followed by annealing in inert atmosphere allows the realization of a structure with good electrical conductivity and with a carbon-based coating preventing the direct contact between the silicon particles and the electrolyte. This structure maintains a specific charge capacity of approximately 1000 mAh/g^{-1} for 200 cycles and reaches a coulombic efficiency of 99.8%. The addition of PVP is a simple and scalable way of realizing, after annealing, a carbon-based matrix which surrounds the silicon particles and which greatly enhances the stability of the battery. The proposed process is based on commercially available carbon nanotubes, on silicon quantum dots which are produced using a scalable plasma-enhanced chemical vapor deposition technique, and is compatible with

large area coating and processing techniques. The fabrication protocol described in this contribution represents a step towards the successful commercial utilization of silicon-based nanomaterials for energy storage applications.

3.1 Introduction

As described in Chapter 1, continuous improvements in lithium ion battery performance are highly desired especially to enable their use in automotive applications. Silicon as anode material has been extensively studied in the last few years. Several factors still prevent its utilization in commercial batteries. Silicon has poor electrical transport properties compared to graphite, thus it needs to be used in combination with electrical conductive additives. It experiences large volume variations during battery charge/discharge resulting in pulverization of the active layer [2], leading to poor cycling stability and rapid capacity fading. The chemical stability of silicon with typical electrolyte formulations is poorly understood, and in particular the formation of a solid electrolyte interface (SEI) with poor mechanical stability [3] and with poor lithium ion transport properties [4-6] is believed to negatively affect the cyclability of silicon-containing structures. The loss of electrical contact between active materials and the current collector [4,7,8] is also a crucial problem, considering that the contact must be capable of accommodating for the large volume change of silicon.

The issue of the pulverization of the active material upon cycling can be resolved by using nanostructured silicon, such as nanowires [9-12], nanotubes [13] and nanoparticles [14-15] as discussed in Chapter 1. For the case of nanoparticles, keeping the size below 150 nm has been found to prevent particle fracturing during lithiation/delithiation [15]. In order to maintain a good electrical conductivity, the addition of conductive additives is necessary. Graphite [16-20], graphene [21-25], carbon nanotubes [3, 7, 26, 27] have been used for this purpose. Finally, several reports suggest that over coating the silicon surface with a carbon-based layer is a promising strategy to enhance the stability of the anode [12,13,28].

To summarize, a critical analysis of the vast literature on this topic suggests that a viable silicon-based anode requires the use of small silicon nanostructures which are firmly in contact with a current-carrying element (typically a carbon-based structure) and which are protected with a carbon-based coating. Moreover, the scalability of the fabrication method with which this structure is realized is important, given the large-scale requirements of the energy-storage market. With this study we propose a fabrication approach that is scalable, compatible with large-scale manufacturing requirements and that achieves a structure that satisfies the conditions summarized above. Our fabrication protocol is based on the non-thermal plasma synthesis of silicon nanoparticles [29,30], a technique which has emerged as a promising candidate for the high-rate

production of high-quality, freestanding silicon nanoparticles. This technique is capable of producing up to hundreds of milligram per hour of silicon particles smaller than 10 nm, with a narrow size distribution (all particles are below 10 nm in size) and with precursor utilization that approaches unity when silane (SiH_4) is used as precursor, and that exceeds 50% when silicon tetrachloride is used as precursor [30]. We functionalize the silicon particle surface and combine it with commercially available carbon nanotubes and a common polymer (polyvinylpyrrolidone, or PVP) to form a liquid dispersion that can then be applied using standard coating techniques to the desired surface, such as copper foil. The liquid dispersion approach is compatible with large-volume coating techniques such as roll-to-roll slot die coating. Annealing at a temperature of 500-550°C leads to the decomposition of the polymer additive and to the formation of a carbonaceous structure which is responsible for a significant improvement in battery stability compared to the structure without any PVP additive.

The chapter is organized as following: the synthesis and processing protocol is first discussed, followed by a description of the techniques used for materials characterization and for the measurement of the electrochemical half-cell performance. The results for our proposed structure and for carefully designed control experiments are then presented and discussed.

3.2 Experiment

3.2.1 Si QDs synthesis and surface chemical modification

Crystalline silicon nanoparticles with a narrow size distribution were produced using the non- thermal plasma technique described in [29]. The process is easily scalable and converts the precursor (silane) into nanoparticles with a utilization rate that can approach unity with an optimized reactor design [30]. For this study, silicon quantum dots (SiQDs) were prepared in a 1/2" outer diameter Pyrex reactor with a flow rate of 150sccm of 1.37% SiH4 in argon. The reactor pressure was 3.0 Torr. 100 sccm of H_2 were added at the exit of the plasma volume via a side gas inlet to increase the surface coverage with hydrogen [31]. This additional exposure to hydrogen enhances the reactivity of the surface with ligands such as alkenes [31]. The electrical 9iupower supplied by the radio frequency (RF) generator was 35 Watts, sufficient to create particles with a crystalline structure. The <10 nm silicon nanoparticles are collected at the exhaust of the plasma reactor via filtering and transferred into a glove box while carefully avoiding oxygen exposure. Surface modification with 12-carbon long chains is performed with the goal of preventing oxidation and of stabilizing the SiQDs in organic solvents such as chloroform or toluene. Organic aliphatic chains are grafted on the surface of silicon nanoparticles by refluxing the nanoparticles in a 1-dodocene / mesitylene (1:4 v%) mixture. Before reaction,

high purity argon was bubbled through all solvents and reactants to minimize the oxygen level, and molecular sieve were used to remove water traces. The alkylation reaction typically lasts for 4 hours at the solvent boiling point (164.7°C). After surface modification the particles are separated by evaporating the solvent with mild heat under vacuum. Fourier transform infrared spectroscopy (FTIR) measurements shown in Figure 3.1 Indicates that the surface modification reaction is successful, peaks at 2900cm^{-1} ~3000cm^{-1} indicate the C-Hx bond. The dried, surface modified particles are silicon quantum dots forms clear dispersion in organic solvents THF, chloroform and toluene etc., while non-functionalized nanocrystals flocculate. Figure 3.2 is the image of SiQDs disperse in chloroform before (left) and after (right) surface modification.

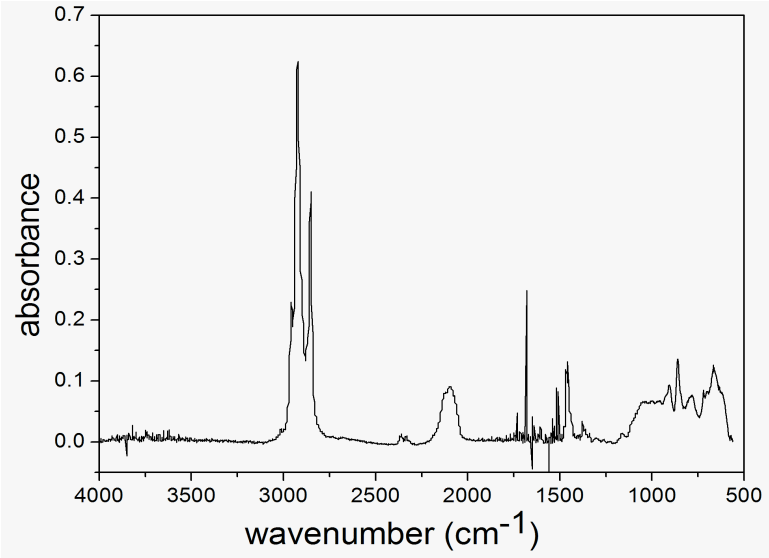

Figure 3.1 Fourier transform infrared spectroscopy (FTIR) spectrum of functionalized SiQDs.

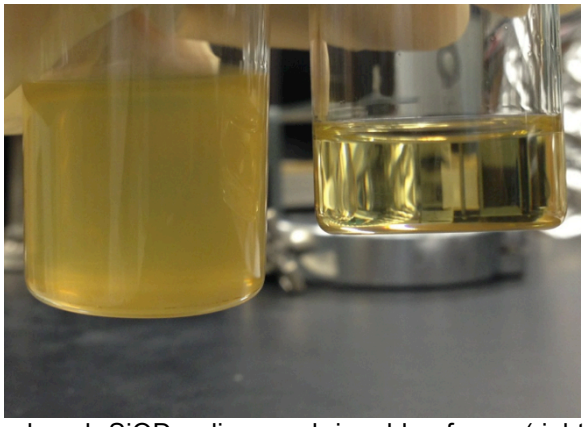

Figure 3.2 (left) as-produced SiQDs dispersed in chloroform; (right) functionalized SiQDs dispersed in chloroform.

To use a scalable, environmental friendly and non-wet chemical method, in non-thermal plasma synthesis of functionalized SiQDs was applied. The mechanism is explained in [56]. Figure 3.3 portrays the schematic set up of non-thermal plasma synthesis of functionalized SiQDs. The process is easily scalable and converts the precursor (silane) into nanoparticles with a very high utilization rate. Silicon quantum dots (SiQDs) were prepared in a 1 inch outer diameter, 12 inches long quartz tube reactor with a flow rate of 200sccm of 1.37% SiH_4 in argon. The reactor pressure was 1.5 Torr. The copper ring electrode is 1 inch wide, and kept at a distance of 5 cm from the nearest metal flange. 1-dodecene is supplied from a bubble system designed to control independently flowing through the bubbler. Typically, 140 sccm of argon gas was flow to the bubbler and the 1-dodocene flow rate can be calculated using this equation [30]:

$$Q_d = Q_{Ar} * P_{vapor}[\text{dodocene}] / (P_{bubbler} - P_{vapor}[\text{dodocene}])$$

The 1-dodocene vapor was added via a counter-direction gas inlet (3 inches from the plasma electrode) to cover the SiQDs surface with 12 carbon long chains.

The electrical power supplied by the radio frequency (RF) generator was 50 Watts, sufficient to create particles with a crystalline structure. The surface functionalized ~5 nm silicon nanoparticles are collected at the exhaust of the plasma reactor via filtering and the particles can form clear dispersion in nonpolar organic solvents, eg. chloroform. These silicon nanocrystals are robust in oxygen exposure. Figure 3.4 (right) indicates SiQDs collected from this set up can uniformly disperse in chloroform solution. The production rate is ~170mg/hr. By increasing SiH_4 flow, 1-dodocene flow, the reactor diameter and 1-dodocene gas inlet numbers, the production rate can be scalable to industrial mass production level.

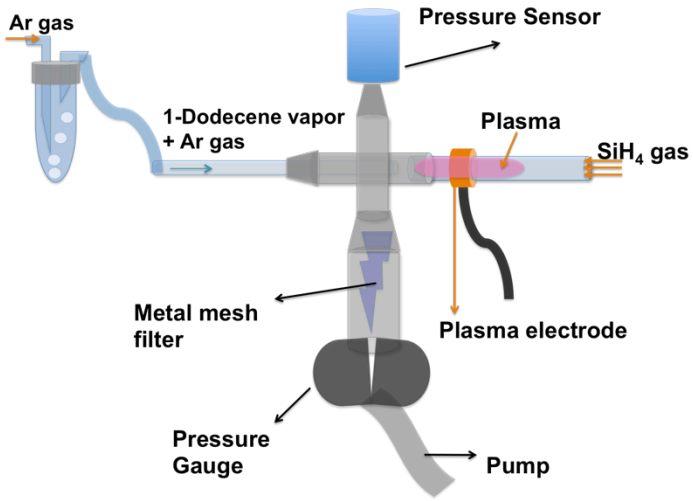

Figure 3.3 Schematic of non-thermal plasma synthesis of functionalized SiQDs

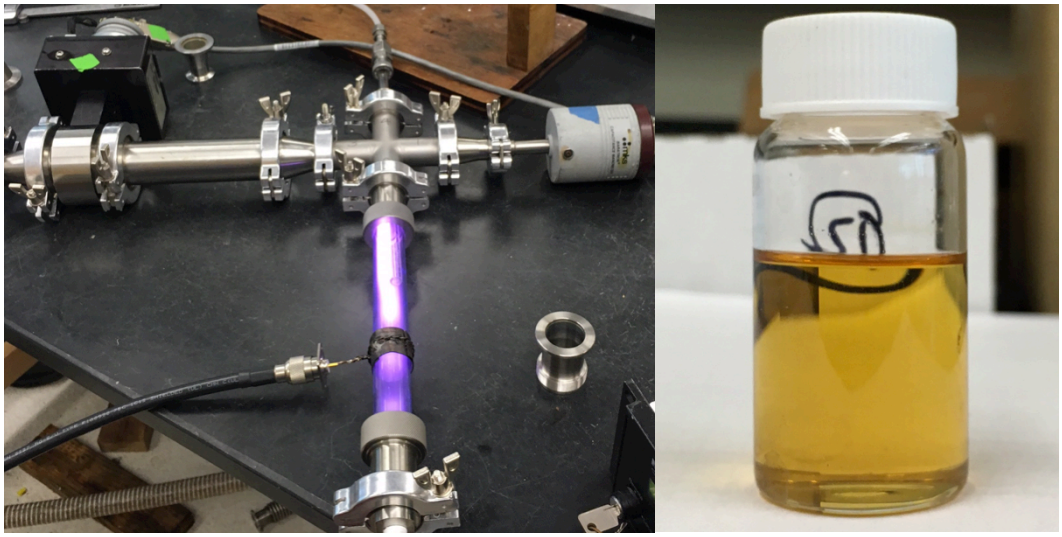

Figure 3.4 (left) image of non-thermal plasma synthesis of functionalized SiQDs, purple-bright color with plasma on; (right) SiQDs synthesized using the left set up, uniformly disperse in chloroform.

3.2.2 Si-QDs-PVP-CNTs composites fabrication

Multiwall carbon nanotubes (part number 724769 from Sigma Aldrich, OD x L 6-9 nm x 5 um) and polyvinylpyrrolidone (PVP), (part number PVP-40 from Sigma Aldrich, 40000 molecular weight) were used as received. In a typical preparation procedure, 10 mg of functionalized Si QDs and 10 mg of PVP are disperse in chloroform and bath sonicated for 5 minutes. 2.5 mg of CNTs are then added to this solution and the mixture is probe sonicated for 5 minutes. Figure 2. Shown the image of f-SiQDs:CNT:PVP solution in a small vial. The solution looks like uniform black ink. The weight distribution of active elements in the dispersion is thus 4:1:4 of SiQDs:CNT:PVP. The same procedure is followed for the preparation of control samples without additives such as PVP. The dispersion is then applied to copper foil by drop-casting. The coating is then dried and baked

in a tube furnace under a continuous flow of argon (25 sccm) at a pressure of 0.21 Torr. The leakage rate of the annealing apparatus is below 0.03 Torr/minute. The temperature is ramped up from 50 °C to 550 °C with increments of 100 °C, holding the temperature for 10 minutes at each step.

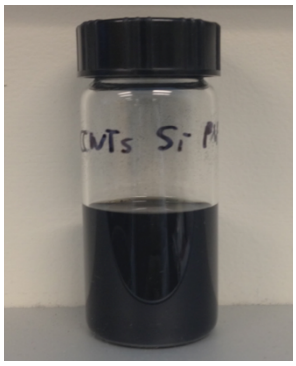

Figure 3.5 f-SiQDs:CNT:PVP in chloroform ink.

3.2.3 Electrode preparation and electrochemical testing

After annealing, the copper foil with silicon-based coating is assembled into a coin cell battery which uses lithium foil as counter electrode. We use commercially available separator from MTI (Li-ion Battery Separator Film, Part number: EQ-bsf-0025-60C). 1 M LiPF6 in ethylene carbonate/diethyl carbonate (1:1 v/v) was used as the electrolyte (from MTI, Electrolyte LiPF6, part number: EQ-Be-LiPF6). All cells are cycled between 0V and 1.5V. The charge capacity is measured at a using a potentiostat from Arbin Instruments. Cyclic voltammetry (CV) is performed at a sweeping rate of 0.1 mV/s using modelVMP3 from BioLogic Science.

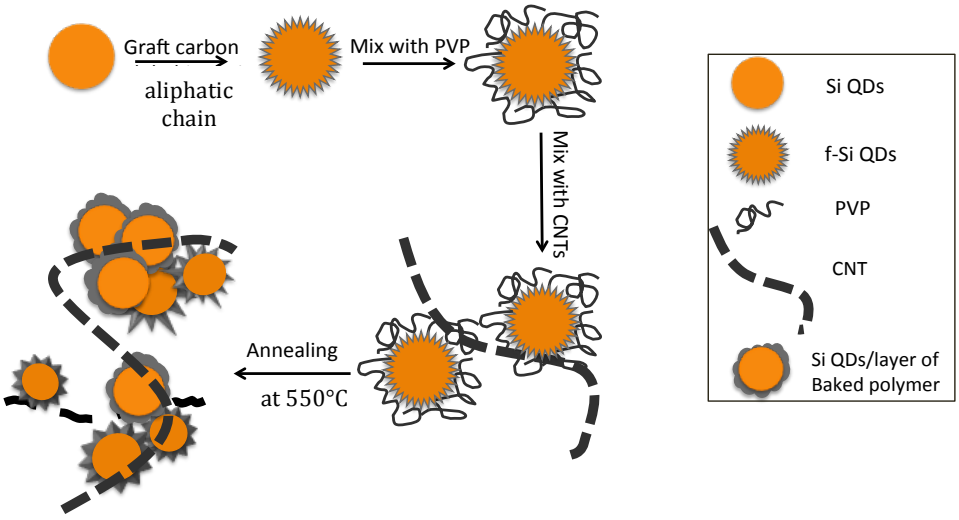

Figure 3.6 Schematic illustration of the whole fabrication procedure.

3.2.4 Materials characterization

We use a variety of techniques to characterize the material under investigation. Scanning electron microscopy (SEM) is performed on a Nova NanoSEM 450. Transmission electron microscopy is performed by scratching some of the active layer onto a lacey carbon TEM grid (from Ted Pella, product number: 01895-F) and by analysing it using a Tecnai T12 120 kV instrument. Raman is performed using a Horiba LabRam system with a 532 nm laser source. X-ray diffraction (XRD) is performed on a PANalytical EMPYREAN instrument with a CuKa source. Thermal gravimetric analysis is conducted by using a Seiko 220U TG-DTA instrument. Fourier Transform Infrared (FTIR) spectroscopy is done using a modular spectrometer from Newport-Oriel. Samples for FTIR are prepared either by drop-casting a dispersion onto a reflective surface and by performing diffuse reflective (DRIFT) measurements, or by using a zinc selenice ATR crystal.

3.3 Results and Discussion

Figure 3.7 (a) show a top-down SEM micrograph of a coating obtained by drop-casting a SiQDs- PVP-CNT dispersion onto copper foil. The carbon nanotubes appear to be uniformly coated with a nanostructured layer. Figure 3.7 (b) has been obtained by drop-casting the same dispersion onto a TEM grid. The carbon nanotube backbone is coated with a layer whose thickness (around 10 nm) is consistent with the size of the silicon particles. For comparison, we also show in Figure 3.7 (c) a top-down SEM micrograph of a coating obtained using a dispersion of carbon nanotubes alone. The clear difference with respect of figure 3.7 (a) further supports the conclusion that a uniform coating of silicon particles is obtained around the carbon nanotubes. Without any additional processing this structure has poor electrochemical performance, most likely because of the poor electrical contact between the particles and the nanotubes. This is due to the presence of relatively long aliphatic chains grafted to the particle surface, and by the presence of the polymer additive. The device functionality is enabled by annealing at moderately high temperatures in an inert atmosphere. Our best performance has been observed for an annealing temperature of 550°C. During thermal annealing we observe significant restructuring of the anode. In figure 2.7 (d) we show the top- down SEM micrograph of the coating shown in figure 1a after thermal annealing at 550°C. The silicon particles tend to agglomerate into clumps with a size of few tens to hundreds of nanometers. At this point we have been unable to avoid this restructuring, which is probably due to the

decomposition of the polymer additive during the annealing process. We have performed TEM on the resulting structure by scratching some material off the surface of the annealed coating and by then applying it onto a lacey carbon TEM grid. The individual quantum dots are still clearly distinguishable in the large agglomerates, as shown in figure 3.7 (e). A combination of dark field imaging and selected area diffraction (figure 3.7 (f) and its inset, respectively) leads to the conclusion that the agglomerates are comprised of silicon nanocrystals. The particles do not coalesce into large crystals or denser agglomerates. A series of higher magnification TEM images confirms the presence of nanocrystals within the large agglomerates will be discussed in later part. Analysis of the higher magnification images confirms that the lattice fringes have a spacing corresponding to that of [111] silicon planes.

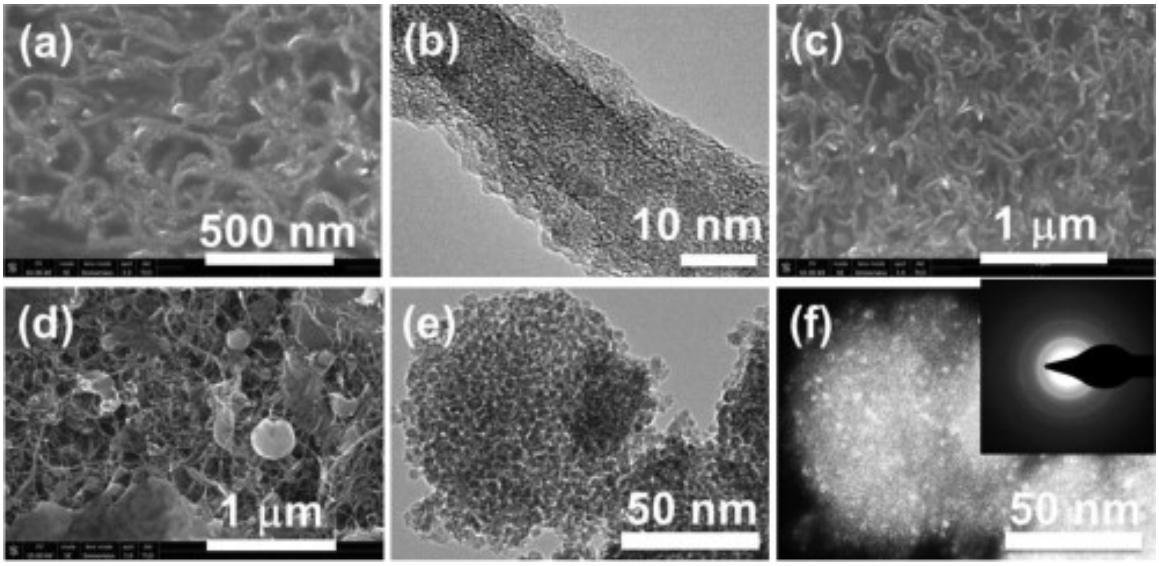

Figure 3.7 (a) SEM of a coating generated by drop-casting a dispersion of silicon quantum dots, carbon nanotubes and PVP onto a copper film. (b) TEM of silicon quantum dots and PVP coating a multi-walled carbon nanotube. (c) Same as (a) but without the silicon quantum dots. (d) Same as (a) but after annealing at 550 °C in argon. Restructuring of the coating takes place during the annealing process. In particular, the silicon particles agglomerate into larger clumps. (e) TEM of a clump of silicon particles resulting from the annealing process. The sample is prepared by gently scratching the sample shown in (d), by dispersing the material in methanol and by drop-casting onto the TEM grid. (f) Dark field of (e) confirming the presence of nanocrystals. In the inset of (f) the selected area diffraction pattern for the particles shown in (e) and (f) is shown. An area including a large number of particles is selected to generate the pattern.

Lower magnification SEM image for as f-SiQDs-PVP-CNTs electrode after annealing at 550 °C in argon is depicted in Figure 3.8. Large SiQDs-aC agglomerations can be observed. Agglomerations spheres diamter range from a few hundred nanometers to 2μm, and in direct contact with very conductive carbon nanotubes. The formation mechanism can be determined by the following: The electrode is annealed to 550°C in argon for 30mins. PVP melts and decomposites to amorphous carbon from 300°C to 550°C, it physically experience moving and large volume “shrinking”. Since each f-SiQD was tightly bound by PVP polymers attribute to its aliphatic chains, thus during PVP convert to amorphous carbon process at high temperature, light-weighted SiQDs can be

moved by the force created by this moment and volume shrinking and lead to large agglomerations of SiQDs with amorphous carbon around each quantum dots. Details of the amorphous carbon will be discussed in the TEM image section.

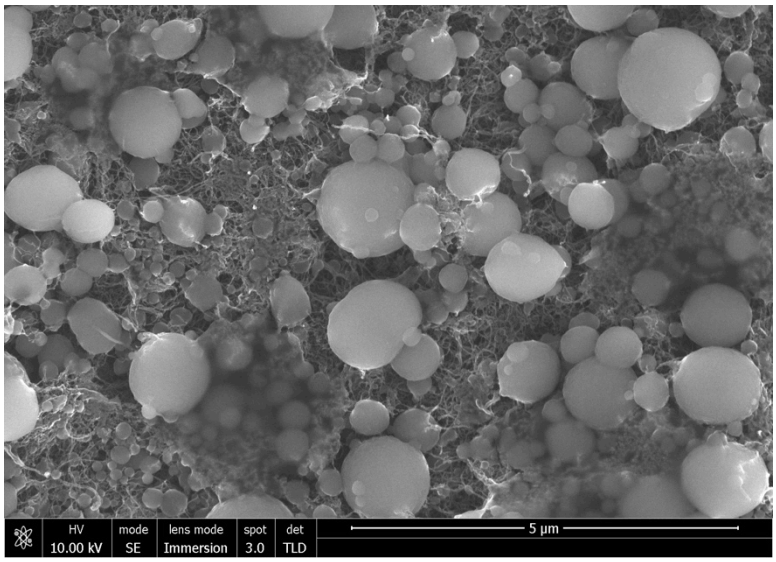

Figure 3.8 Lower magnification SEM image for as f-SiQDs-PVP-CNTs electrode after annealing at 550 °C in argon; Scale bar 5µm.

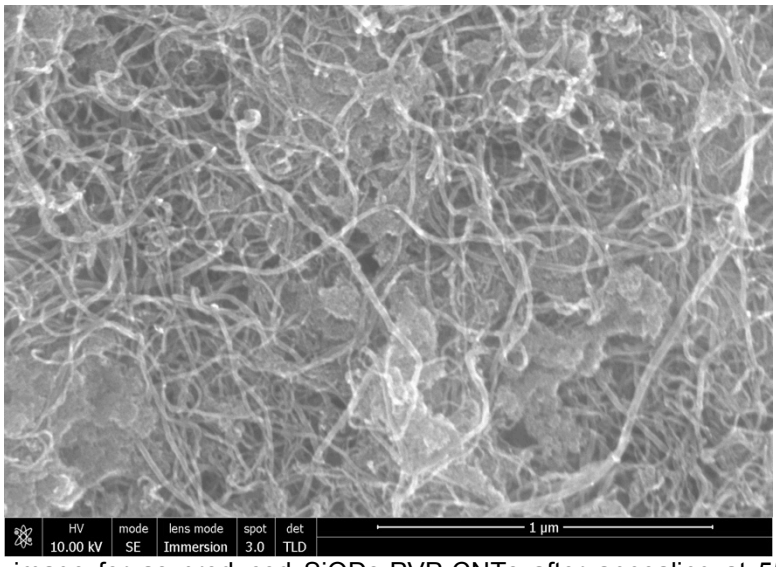

Figure3.9 SEM image for as produced SiQDs-PVP-CNTs after annealing at 550 °C in argon; Scale bar 1µm.

Figure 3.9 shown the SEM image of control experiment as produced SiQDs-PVP-CNTs after annealing at 550 °C in argon. The morphology is dramatically different while compare with functionalized SiQDs. SiQDs aggregates, yet, not in sphere shape due to the different surface binding mechanism with PVP. The different morphology gave distinctive battery performances, which will be discussed in later sections.

Despite the spatial rearrangement of the silicon particles during annealing, this structure achieves a very promising electrochemical performance. After annealing, the weight loading is around 0.2 mg/cm^2 for this battery. In Figure 3.10 we show the discharge capacity plotted against the number of charge-discharge cycles. The first discharge cycle achieve a capacity of 1600 mAh/g, which quickly decays to 1000 mAh/g. This value is then maintained for 200 cycles. The Coulombic efficiency, while being low for the first few cycles, reaches a stable value of 99.8% before starting to decrease close to the 200th cycle.

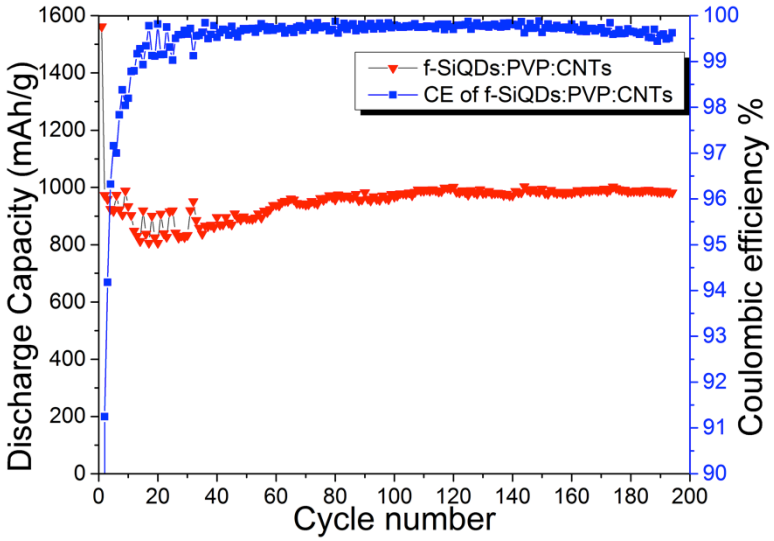

Figure 3.10 Discharge capacity (mAh/g) and coulombic efficiency over number of charge–discharge cycles for the sample shown in Fig. 1(d). Weight loading 0.2mg/cm^2

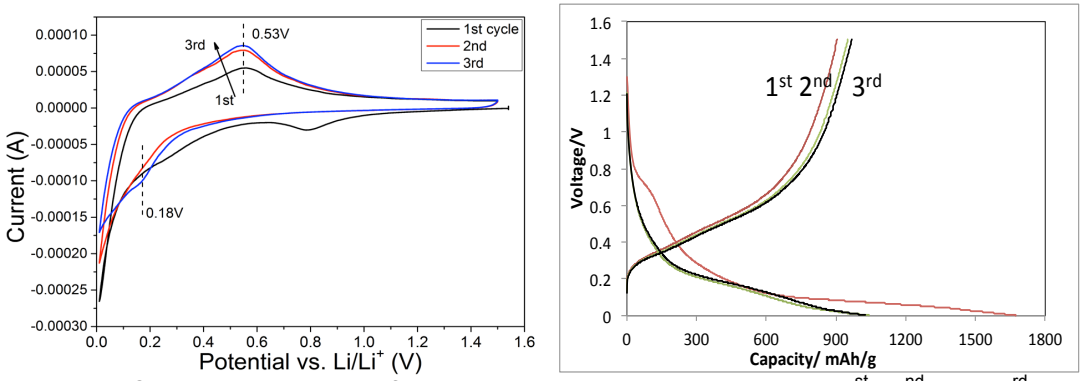

Figure 3.11 Cyclic voltammetry of the sample shown in Fig. 2.7(d). 1st, 2nd and 3rd cycles Galvanostatic charge/discharge profile.

In Figure 3.11 we show the results of the cyclic voltammetry measurements for the first through third cycles. Broad delithiation and lithiation peaks at 0.6 V and 0.18 V respectively are observed, consistent with previous studies on silicon-based anodes. The half-cell capacity measurement has been performed at a charge and discharge rate of 0.1C, calculated based on the sum weight of the silicon quantum dots and carbon nanotubes coated onto the copper substrate. This approximation would be correct under the assumption that the polymer is

completely removed from the coating during the annealing process. Our temperature-controlled gravimetric analysis (TGA) measurements show that PVP is not completely removed during the annealing process, although the error introduced into the calculation of the specific charge capacity is small.

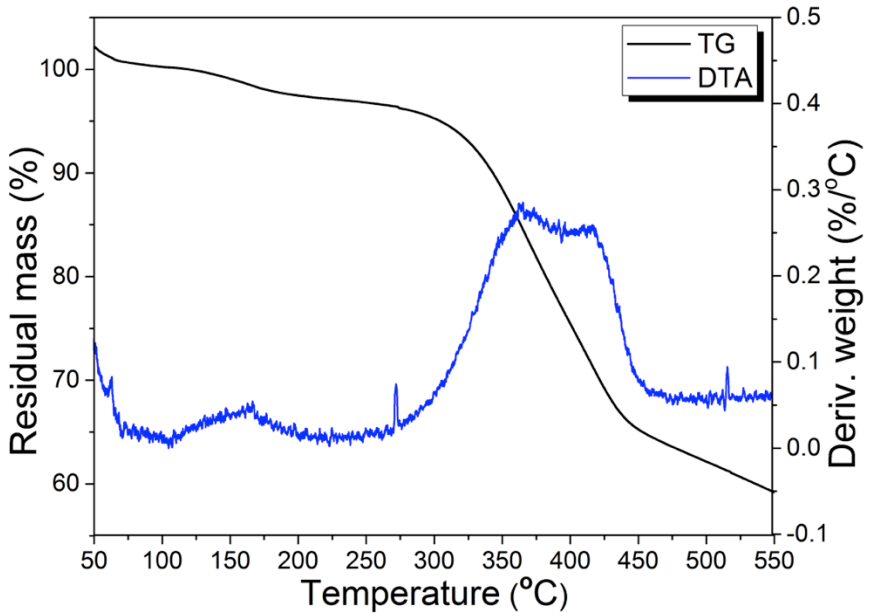

Figure 3.12 TGA of the coating prepared from the 4:1:4 liquid dispersion of SiQDs:CNT:PVP. The negative of the differential of the TGA scan is also shown to highlight the decomposition temperature.

The TGA scan for our SiQDs:CNT:PVP sample, together with the corresponding differential (DTGA) analysis, is shown in figure 4. We have normalized the data so that the weight fraction is 100% at 100°C, i.e. after an initial weight loss due to the removal of residual solvent from the film. Weight loss occurs around 150°C and at 350°C. Both these peaks are consistent with TGA data reported in the literature for PVP [34,35]. Based on the initial weight distribution in the dispersion of 4:1:4 of SiQDs:CNT:PVP, we find that the decomposition of PVP at high temperature leads to the presence of a residue in the annealed structure. This is

to be expected for the case of PVP, which is known to decompose into a carbonaceous structure with a mass yield between 4% and 15% depending on the annealing conditions and on the presence of other additives mixed with the PVP [34]. Based on the TGA measurement we estimate a final composition of 4:1:0.4 of SiQDs:CNT:(PVP decomposition product), corresponding to ~10% mass yield from the PVP decomposition. This does not account for the weight change due to reaction between the PVP and the silicon particles during the annealing reaction, which may lead to the formation of silicon carbide (as it will be more extensively discussed). If we correct the specific charge capacity data to account for the carbon residue from the PVP decomposition, we find that the battery maintains a reversible capacity of 925 mAh/g for up to 200 cycles. Under the assumption that the charge storage is performed by silicon only (consistently with the voltammetry data), we calculate that silicon achieves a reversible charge capacity of 1250 mAh/g for up to 200 cycles.

In order to get higher energy density per area, we also increased the weight loading to 1mg/cm^2, the electrode were prepared with the same method as the battery shown in Figure 3.13. The first cycle columbic efficiency is 57% and increased to 99.5% after a few cycles. An average discharge capacity of 850mAh/g were obtained for 80 cycles. This encouraging results proved that these SiQDs-aC agglomerates are very promising active materials for high energy density LIBs.

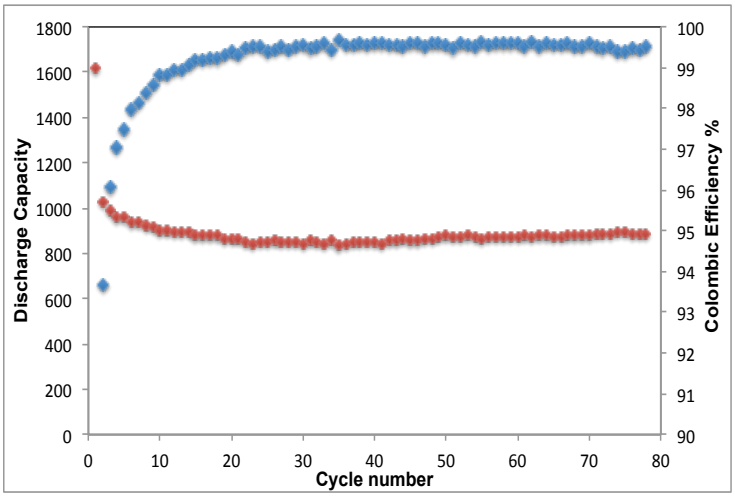

Figure 3.13 Discharge capacity (mAh/g) and coulombic efficiency over number of cycles. Weight loading 1.0 mg/cm^2.

We point out that we selected PVP as an additive because of the good compatibility between PVP and carbon nanotubes [36,37] and because of PVP is soluble in chloroform, which is compatible with the functionalized silicon quantum dots. Figure 1a confirms the compatibility of these components. We have found that PVP is not only necessary at obtaining a conformal coating of silicon nanoparticles onto the carbon nanotubes, but it also acts a precursor for the formation of a carbonaceous layer that entraps the silicon particles. A detailed discussion of the nature of this carbonaceous layer is now presented.

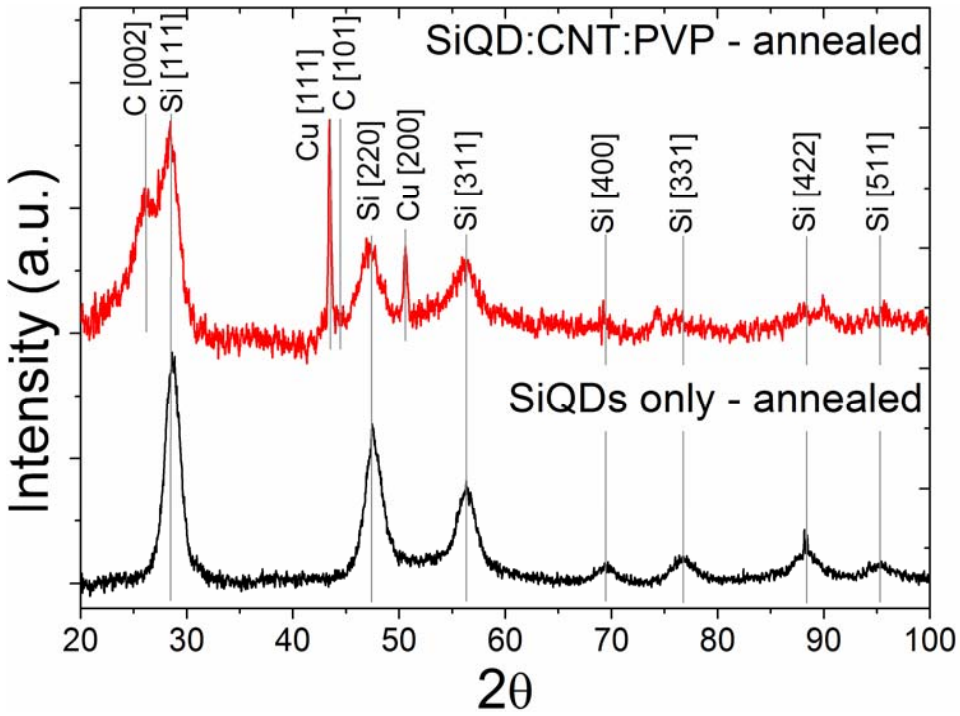

Figure 3.14 X-ray diffraction for the sample obtained by annealing the dispersion of SiQDs:CNT:PVP. Clear peaks from crystalline silicon, from graphite and from the copper substrate are distinguishable (top spectrum). As a reference we also show the x-ray diffraction spectrum for silicon nanoparticles only (bottom spectrum), annealed using the same procedure.

We have first performed x-ray diffraction (XRD) on the annealed coating and on a control sample in which only silicon nanoparticles are present in the coated layer. After thermal annealing, XRD analysis of the full SiQDs:CNT:PVP coating (see Figure 3.14 (a) shows peaks due to the carbon nanotubes (26.5° for the [002] plane and 44.6° for the [101] plane) and to the silicon nanocrystals ([111] at 28.4°, [220] at 47.3°, [311] at 56.1°, [400] at 69.1°, [331] at 76.4°, [422] at 88.1° and [511] at 95°). The [111] and [200] peaks from the copper substrate at 43.3° and 50.5° respectively are also clearly distinguishable. The peak assignment is based on the ICSD databse (Inorganic crystal structure database FIZ Karlsruhe). We could not resolve any contribution from crystalline silicon carbide. Analysis of

the grain size using Scherrer's formula returns a value of 3.9 nm for the silicon particle size after annealing. The control experiment, i.e. the case of silicon nanoparticles only, is shown in Figure 3.14 (b). For this case the particles are annealed on a quartz slide using the same annealing cycle followed for the sample shown in figure 5a, but without any carbon nanotubes, without any PVP and without functionalizing the particle surface. The particle size in this case, calculated using Scherrer's formula, is 5.4 nm. This suggests that the presence of PVP and of the 12-carbon long chains at the particle surface is effective at preventing grain growth. Regarding silicon carbide, the absence of peaks in the XRD spectrum does not rule out that the reaction between silicon and the combination of 12-carbon long chains grafted at the particle surface and of the PVP leads to the formation of silicon carbide with an amorphous structure.

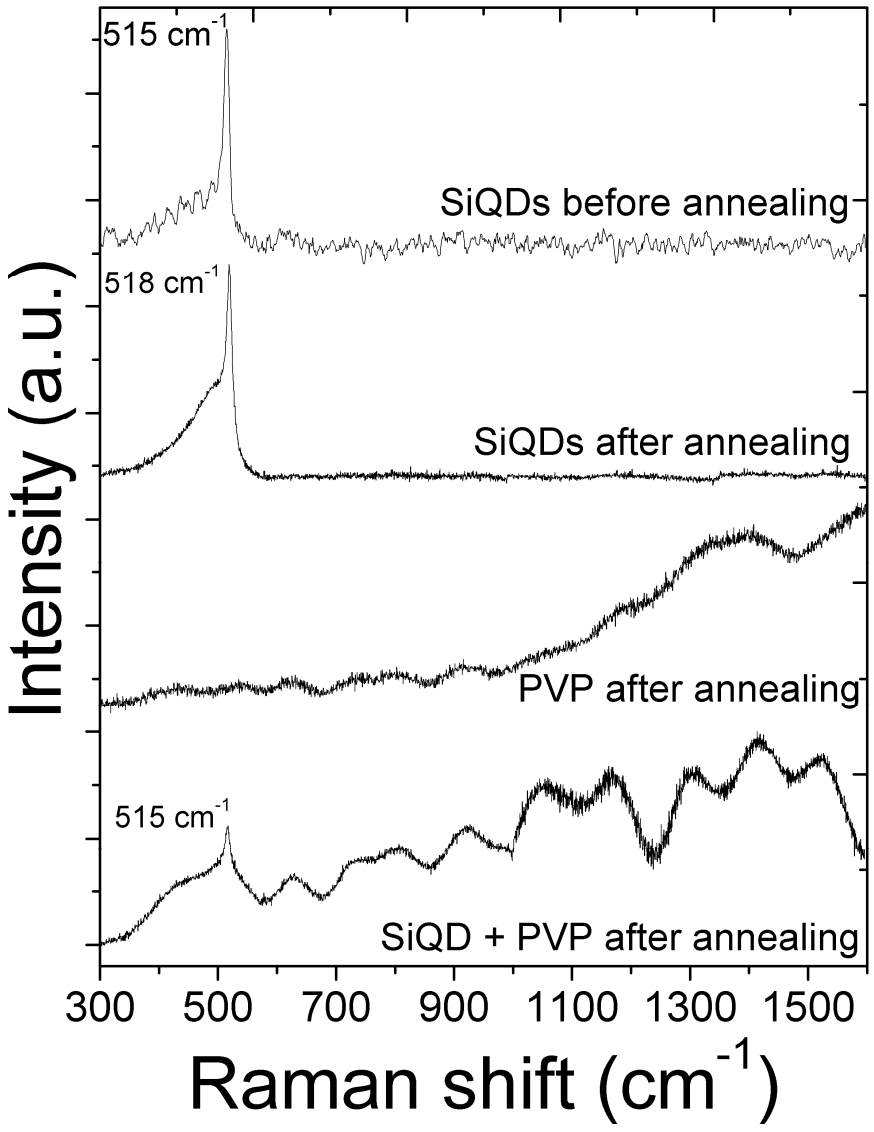

Figure 3.15 Raman analysis of the materials under study. (a) Raman of functionalized silicon quantum dots before annealing. (b) Raman for silicon quantum dots after annealing. (c) Raman of 1-dodecene functionalized silicon quantum dots after annealing. The main feature related to the silicon nanocrystals is visible in (a), (b) and (c). A small broad peak around 900 cm−1 is distinguishable in (c) and attributable to amorphous silicon carbide (see text for complete discussion). (d) Raman of the product of decomposition of PVP, annealed using the same procedure used for the anode structure. Clear signature of graphitic carbon is present. (e) Raman of functionalized silicon quantum dots and PVP, after annealing. Features due to crystalline silicon, graphitic and amorphous carbon, and amorphous silicon carbide are distinguishable (please see text for complete discussion). Carbon nanotubes are not added to this sample to simplify the data interpretation.

Extensive Raman characterization, shown in Figure 3.15, supports the conclusion that the presence of a carbon precursor in the coating leads to the formation of both an amorphous carbon phase and of amorphous silicon carbide in the final structure. In Figure 3.15a we show the Raman spectra for the as-produced silicon quantum dots, functionalized with 1-dodecene. The particles were drop-cast onto a quartz slide, and due to the low thermal conductivity of the nanoparticle coating it is necessary to acquire this data using very low laser power, reducing the signal-to-noise ratio. Laser-induced heating introduces a shift in the crystalline silicon peak position to lower wave numbers. We have made sure that no heating-induced shift is present for this sample, and we find the expected silicon peak at a position of 515 cm^{-1}. The shift compared to the bulk value of 521 cm^{-1} and the appearance of a shoulder at lower wavenumbers are well-known to be induced by the small size of the crystal [38-41]. For the case of non-functionalized silicon particles annealed using the same profile as for the anode (Figure 3.15b) we also obtain only one feature corresponding to nanostructured silicon. The shift in the peak position to 518cm^{-1} is consistent with a growth in crystallite size. In Figure 3.15c we show the Raman spectrum for the decomposition product of PVP, under the same annealing conditions. The broad features at 1350 cm-1 and 1580 cm-1 correspond to the D and G peaks from sp^2 carbon respectively [42-44]. Finally in figure 6d we show the spectrum for a mixture of functionalized silicon quantum dots and PVP, after annealing at 550°C. The carbon nanotubes are not added to this mixture, since their expected

contribution to the signal between 1300 cm-1 and 1600 cm-1 would make the interpretation of the spectrum more difficult. The peak corresponding to crystalline silicon is still present although its peak position is at 515 cm^{-1}. This is consistent with the previous XRD observation that the presence of the carbon precursor prevents crystal agglomeration and growth during annealing. A significant shoulder is also present at lower wavenumber between 400 cm-1 and 450 cm-1, consistent with the contribution which has been observed at low wavenumbers in various amorphous carbon structures [45-47]. The shape of the Raman spectrum in the 1100 cm-1 to 1600 cm-1 range is also significantly different than that of the spectrum shown in figure 6c. Raman analysis of carbon-based structures is known to be very sensitive to the degree of ordering in the film and to the ratio of sp2 to sp3 bonding [42-44]. The shift of the G band to lower wavenumber compared to the case shown in figure 6c can be attributed to a decrease in the fraction of graphite-like carbon in the film and to an increase in the presence of amorphous, sp3 bonded carbon. The additional peaks at 1150 cm-1 and 1450 cm-1 present in Figure 3.15d compared to Figure 3.15c have been assigned to transpolyacetylene chains [48]. Overall, these data suggests that the presence of silicon nanoparticles dispersed within the PVP matrix leads to the formation of a carbon-based structure which is significantly different than what is obtained without silicon particles, following an identical annealing procedure. The authors in [44] also point out that a shift of the G peak to lower wavenumbers is observed for increasing silicon fraction for the case of

amorphous silicon carbide alloys. This is consistent with an increase in the broad Raman scattering signal in the 600 cm-1 to 900 cm-1 range, which has been observed in amorphous silicon carbide films grown by plasma-enhanced chemical vapor deposition [49-50], in super-lattices of silicon particles precipitated in an amorphous silicon carbide matrix [51-52], and has also been predicted by several theoretical studies (see for instance [53]). The data set strongly suggests that amorphous silicon carbide is formed during the annealing of the silicon nanoparticles in presence of PVP. Additional measurements of control samples confirm that the 1-dodecene functionalization alone is not conducive to the formation of the carbon matrix. The polymer not only helps dispersing the carbon nanotube in the desired solvent, but also acts as precursor for the formation of a carbon-based matrix.

The conclusion drawn from Raman spectrums are also convinced by more careful TEM studies. As shown in Figure 3.16.

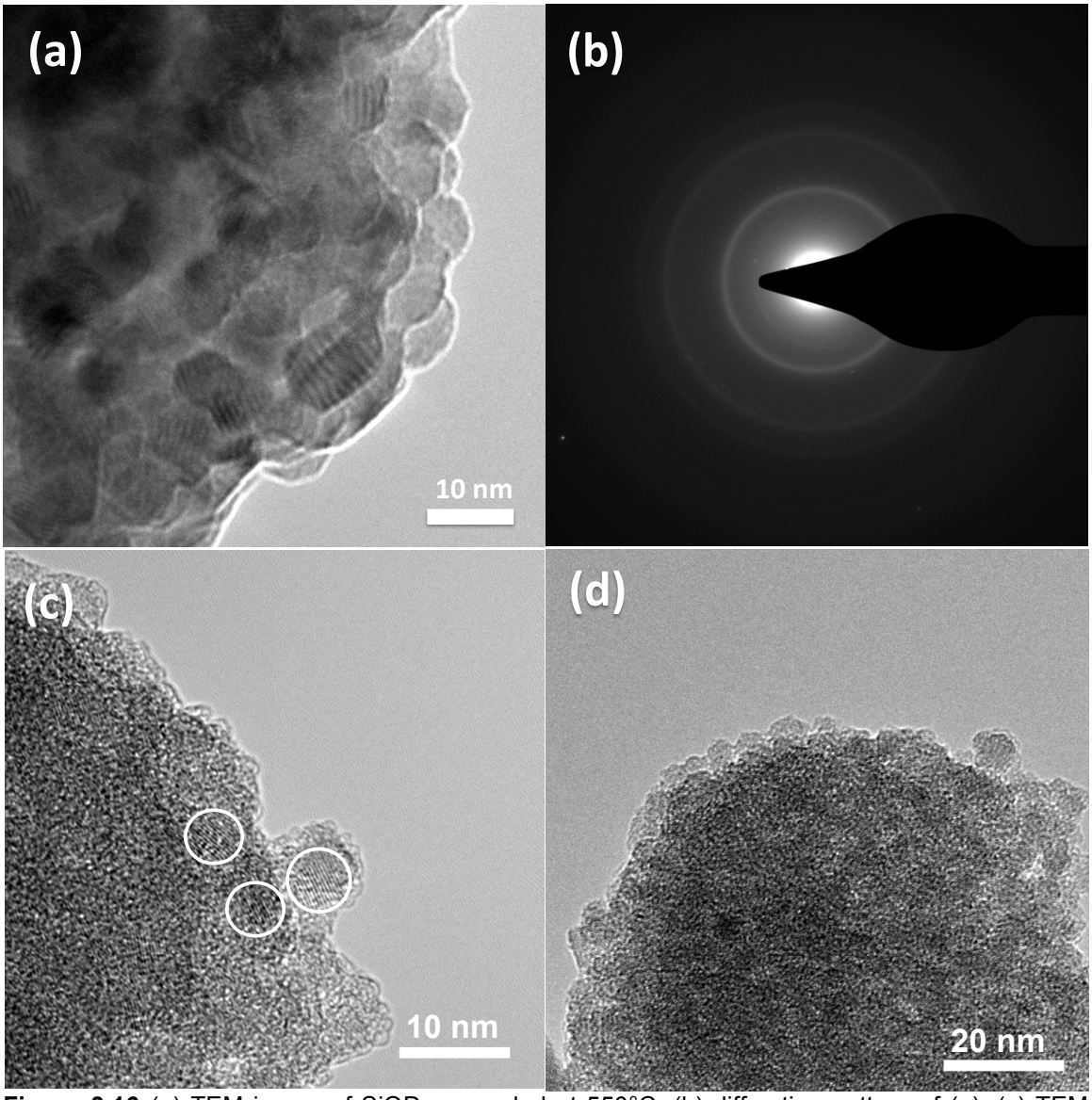

Figure 3.16 (a) TEM image of SiQDs annealed at 550°C; (b) diffraction pattern of (a); (c) TEM image of f-SiQDs-PVP annealed at 550°C, silicon crystal lattice in white circle; (d) TEM image of another agglomeration.

TEM image of SiQDs annealed at 550°C is shown in Figure 3.16a). Obviously, silicon quantum dots agglomerate and crystal size grown, roughly ~6nm. Moreover, their boundary is clear. Figure 3.16c) presents the TEM image for annealed f-SiQDs-PVP. These high magnification images suggest that silicon quantum dots maintain their crystal lattices, see lattice inside the white circles.

The size is ~4nm, which is consistent with XRD Scherrer's formula calculations. The image also suggests that the silicon quantum dots are surrounded by a uniform layer of amorphous material, whose properties are going to be discussed in details later in this contribution. High resolution TEM images verify the Raman conclusion that the grafting of aliphatic chains and coating of PVP increased effectively prevent silicon quantum dots from being grow in grain size and result an amorphous carbon layer around each quantum dots after annealing at 550 °C under argon.

Finally, in Figure 3.17 we show the influence of the addition of PVP and of the functionalization of the silicon nanoparticles to the dispersion on the half-cell stability. We compare the performance of silicon-based anodes for the case of a structure based on the SiQD:CNT:PVP dispersion (same as the data shown in figure 2) with that of a structure based on a SiQD:CNT dispersion. For this control anode, PVP is not added to the dispersion and the silicon nanoparticles are not functionalized with the 12-carbon long aliphatic chains. The control anode achieves a significantly smaller capacity and also shows a faster degredation in its performance. The SEM image of as-produced SiQDs-CNTs anode shown in Figure 3.9 indicates that SiQDs aggregated without a certain shape, more and more SiQDs will loose contact with carbon nanotubes upon cycling. By the 200th cycle, the control anode capacity has decayed to 400 mAh/g. Based on the data shown here, we reach the following conclusions:

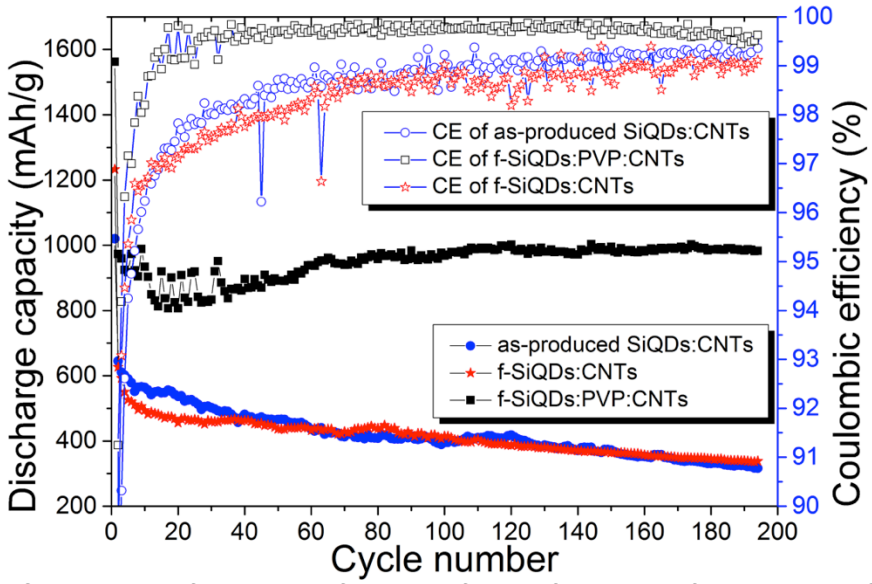

Figure 3.17 Comparison of battery performance for the full anode (functionalized SiQDs-PVP-CNTs) with two control structures. The first control samples is realized using non-functionalized silicon particles and CNT, the second using functionalized silicon particles and CNT. For both the control structures PVP is not added to the liquid dispersion formulation.

Solid Electrolyte Interface (SEI) Study

In order to better understanding the mechanism for this type of electrode, battries after cycling were opened and electrodes were analyzed by utilizing SEM and EDS. Figure 3.18 present the SEM images for electrode collected after 1st cycle at fully lithiation stage. The electrode was opened in an argon filled glove-box, washed in clean acetonitrile for 3 times. Figure 3.18 (a) indicates agglomerations is uniformly distributed and not cracked. However, in Figure 3.18 (b) SEM image, we found that SiQDs-aC agglomerations with size < 5μm expanded but did not crack, while particles > 5μm crack. Thus the agglomeration size boundary is 5 μm for this type of secondary SiQDs-aC particles.

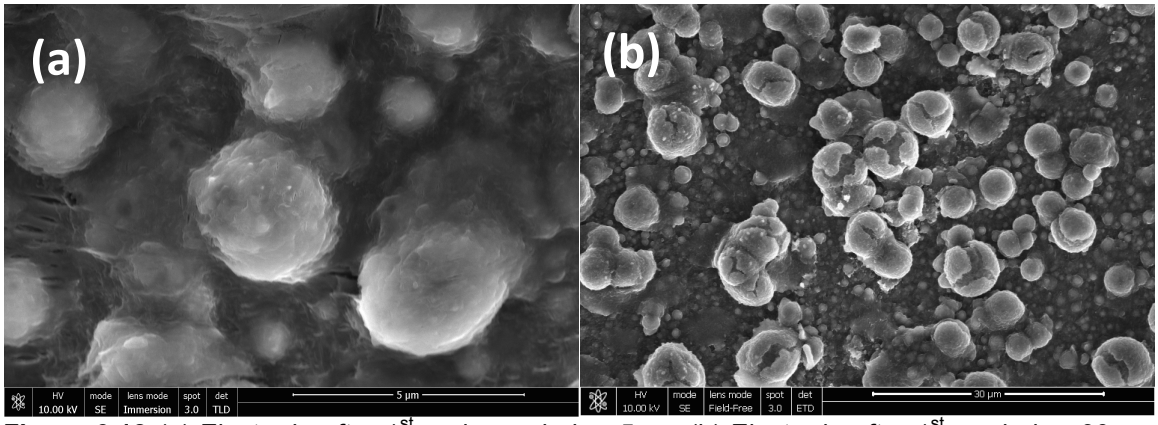

Figure 3.18 (a) Electrode after 1st cycle, scale bar 5µm; (b) Electrode after 1st, scale bar 30µm. Samples collected at fully lithiated stage.

Figure 3.19 are SEM images for electrode after 5 cycles collected at fully delithiated stage. The 1~2µm SiQDs-aC agglomerations sounded by carbon nanotubes still maintain their shape after 5th delithiation (Figure 3.19a). There are spaces between the particles and carbon nanotubes near them. We believe the spaces were for volume expansion during lithium ions insertion. This kind of agglomeration which contain a large number of small SiQDs expand and shrink as one big particle upon cycling. Figure 3.19b indicates when this kind agglomerations is larger than 5 µm, which is consistent with Figure 2.b. Figure 2 (c) (d) (e) (f) are EDS elemental mapping of Figure 3.19(b). The big agglomeration cracked into two pieces after cycling. Silicon (d) can be seen inside this big agglomeration. Fluoride (f) can be seen as an indicator of SEI, it distributed on the surface of this big particle.

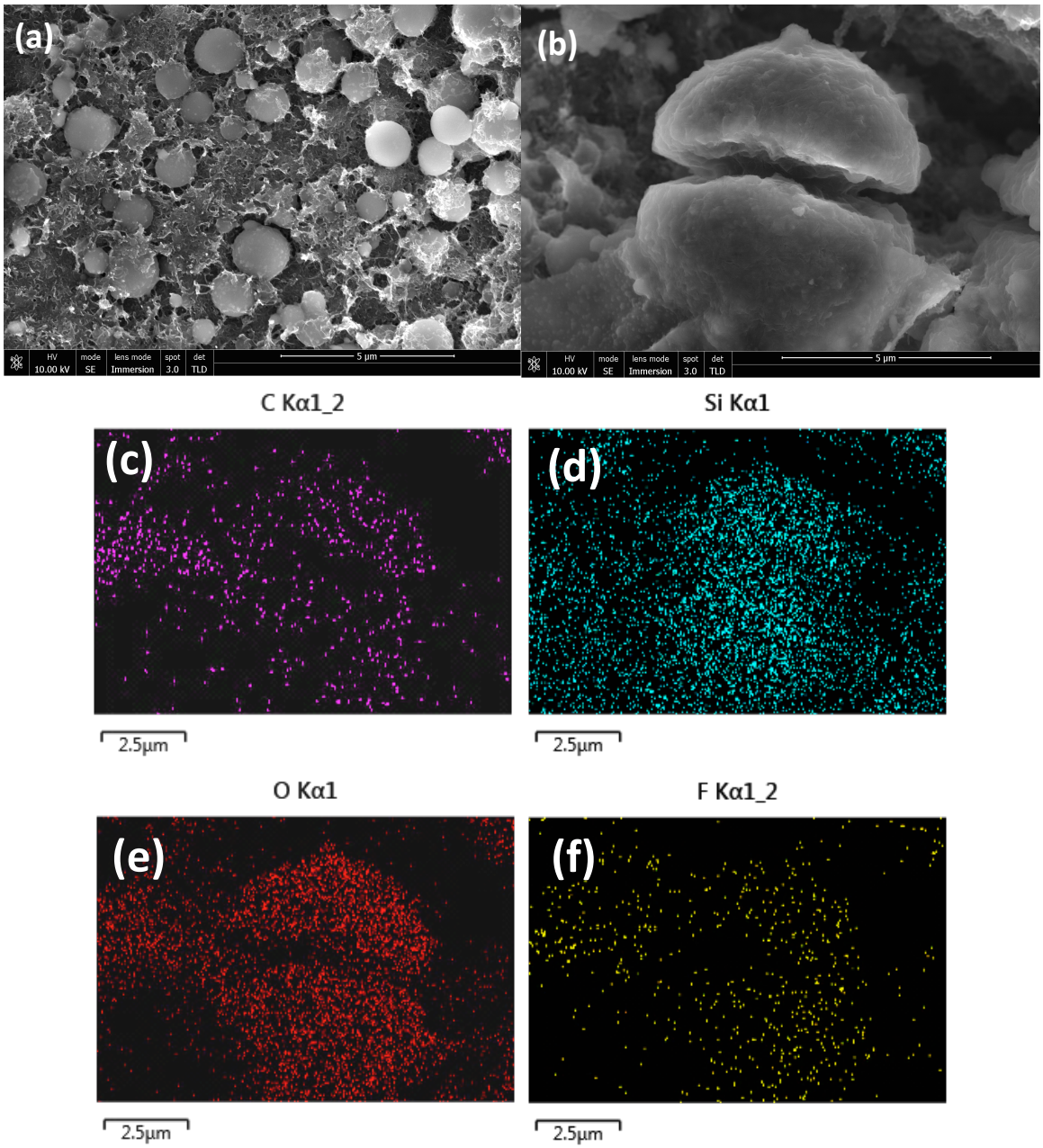

Figure 3.19 (a) Electrode after 5th cycles, scale bar 5µm; (b) Electrode after 5th cycles, scale bar 5µm; (c) carbon (d) silicon (e) oxygen (f) fluoride, EDS elemental mapping of (b). Sample collected at fully lithiated stage.

Battery after its 10th cycle were also opened and examined at its fully lithiated stage. Figure 3.20a depicts that SiQDs-aC agglomerations were still maintain their shape. Figure 3.20b another area on the same electrode, SEI can be found

everywhere. SEI is on the surface of carbon nanotubes as well. This could be a explanation of why the first cycle columbic efficiency is only ~50%. We should minimize surface area not only by aggregating SiQDs together, but also by reducing carbon nanotube amount or replacing carbon nanotubes with another small surface area conductive materials such as carbon black.

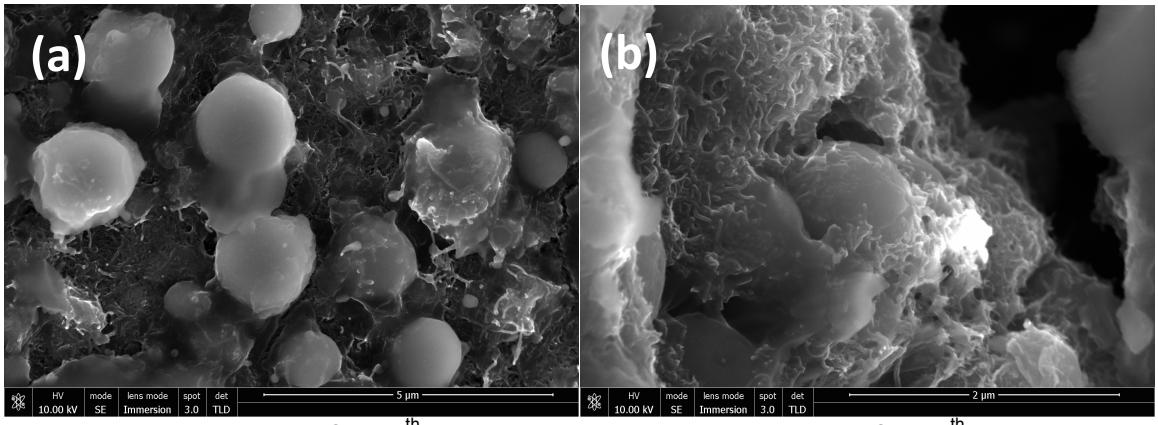

Figure 3.20 (a) Electrode after 10th cycles, scale bar 5µm; (b) Electrode after 10th, scale bar 2µm. Samples collected at fully lithiated stage.

Our silicon quantum dots is as small as 4nm, which allows the effective escape of many vacancies to the surface, minimizing the formation of macroscopic voids or cracks during the cyclic charge and discharge. SiQDs agglomerated particles with a size less than 5µm can “survive” upon cycling; In the future, agglomerations size has to be controlled bellow 5 µm in order to avoid cracks; SEI grow on the surface of agglomerated particles and CNTs surfaces. Carbon nanotubes should be replaced with another conductive materials to increase initial columbic efficiency. After a few cycles, the f-Si-PVP-CNTs anode presents higher columbic efficiency (99.7%) than SiNPs anode (~99%) indicates that the electrolyte is not in direct contact with SiQDs inside of the agglomerations. The

outside amorphous carbon layer is not only functioning as conducting framework, but also an electrolyte-block layer. The interior amorphous carbon can conduct Li^+ and e^- in/out of inner SiQDs.

3.4 Conclusion

· The addition of the PVP to the dispersion formulation is critical for stabilizing the anode performance.

· The presence of the surface functionalization and of the PVP clearly slows the coalescence of the silicon particles, so that after thermal annealing agglomerates with small grain size are produced (see figure 1e). XRD and Raman results are consistent with this interpretation. The decreased grain size may contribute to the enhancement in the structural stability of the particles during cycling. The presence of carbon dispersed within the agglomerates may also enhance the charge transport kinetics, although further investigation is necessary to substantiate this hypothesis.

· Annealing of the PVP-containing coatings leads to the formation of a carbon-based phase. This conclusion is supported by TGA and Raman data. Raman also suggests that amorphous silicon carbide is formed during the annealing step. This is due to the inevitable reaction between the silicon particles and the polymer during the high- temperature annealing. Nevertheless, the presence of

this carbon-based phase in the final structure seems to provide a clear improvement with respect of cycling stability.

· The formation of silicon carbide may also explain the relatively low first cycle capacity of the structure (~1600 mAh/g). Silicon carbide is inactive during the lithiation process [54,55]. The data discussed here suggest that some of the silicon is converted into silicon carbide during the annealing procedure, making a fraction of the silicon material effectively inactive. This problem is exacerbated by the small size of the particles. We are currently investigated the role of particle size on capacity and stability of the anode, and a future contribution will summarize our findings.

Our findings are consistent with those of several other groups that report that protecting the silicon surface with a carbon-based layer is effective at improving the anode lifetime [12,13,28]. The exact mechanism of stabilization is under investigation. The authors in [12] suggest that a carbon layer enhances the mechanical stability of the SEI while preventing the full lithiation of the silicon structure, thus limiting its capacity. The relatively small capacity of our structure may be partially explained by this argument, although (as already mentioned) a significant fraction of the particle volume may be converted into amorphous silicon carbide during annealing, further reducing charge capacity.

Our major finding is that the addition of a polymer additive (PVP) to the silicon nanoparticle and carbon nanotube dispersion is effective at improving the half-cell stability. The combination of TGA, Raman and TEM analysis presented here confirms that the PVP acts as a precursor for the formation of a carbon-containing phase which is beneficial to the battery performance. This represents a simple strategy that could be implemented in large-scale manufacturing protocols. Further optimization is currently ongoing and is focusing on optimizing the battery energy density and stability by varying nanoparticle size and weight loading and by testing different polymer additives.

To summarize, we have developed an ink formulation based on functionalized silicon quantum dots, PVP and carbon nanotubes. Printing of the ink followed by the appropriate annealing cycle leads to the formation of a well-dispered heterojunction of silicon particles and carbon nanotubes. When utilized as an anode for lithium ion batteries, this structure maintains a capacity of approximately 1000 mAh/g for 200 cycles. The silicon particles utilized in this study are produced using a scalable plasma-based synthesis technique which effectively converts silane into particles and that is expected to be scalable to large production rates.

Reference

[1] M. N. Obrovac and L. Christensen, *Electrochemical and Solid State Letters* **2004**, *7*, A93- A96.

[2] J. P. Maranchi, A. F. Hepp and P. N. Kumar, *Electrochemical and solid-state letters* **2003**, *6*, A198-A201.

[3] H. Wu, G. Chan, J. W. Choi, I. Ryu, Y. Yao, M. T. McDowell, S. W. Lee, A. Jackson, Y. Yang, L. B. Hu and Y. Cui, *Nature Nanotechnology* **2012**, *7*, 309-314.

[4] J. C. Guo, A. Sun, X. L. Chen, C. S. Wang and A. Manivannan, *Electrochimica Acta* **2011**, *56*, 3981-3987;

[5] C. K. Chan, R. Ruffo, S. S. Hong and Y. Cui, *Journal of Power Sources* **2009**, *189*, 1132-1140;

[6] M. Nie, D. P. Abraham, Y. Chen, A. Bose and B. L. Lucht, *The Journal of Physical Chemistry C* **2013**, *117*, 13403-13412.

[7] C. Martin, O. Crosnier, R. Retoux, D. Belanger, D. M. Schleich and T. Brousse, *Advanced Functional Materials* **2011**, *21*, 3524-3530;

[8] J. H. Ryu, J. W. Kim, Y. E. Sung and S. M. Oh, *Electrochemical and Solid State Letters* **2004**, *7*, A306-A309.

[9] C. K. Chan, H. L. Peng, G. Liu, K. McIlwrath, X. F. Zhang, R. A. Huggins and Y. Cui, *Nature nanotechnology* **2008**, *3*, 31-35;

[10] C. K. Chan, R. N. Patel, M. J. O'Connell, B. A. Korgel and Y. Cui, *Acs Nano* **2010**, *4*, 1443-1450;

[11] L. F. Cui, R. Ruffo, C. K. Chan, H. Peng and Y. Cui, *Nano Letters* **2009**, *9*, 491-495;

[12] T. D. Bogart, D. Oka, X. T. Lu, M. Gu, C. M. Wang and B. A. Korgel, *Acs Nano* **2014**, *8*, 915-922.

[13] M. H. Park, M. G. Kim, J. Joo, K. Kim, J. Kim, S. Ahn, Y. Cui and J. Cho, *Nano Letters* **2009**, *9*, 3844-3847.

[14] a) C. Erk, T. Brezesinski, H. Sommer, R. Schneider and J. Janek, *Acs Applied Materials & Interfaces* **2013**, *5*, 7299-7307;

[15] X. H. Liu, L. Zhong, S. Huang, S. X. Mao, T. Zhu and J. Y. Huang, *Acs Nano* **2012**, *6*, 1522-1531.

[16] N. Dimov, S. Kugino and M. Yoshio, *Journal of Power Sources* **2004**, *136*, 108-114;

[17] M. H. Kong, J. H. Noh, D. J. Byun and J. K. Lee, *Journal of Electroceramics* **2009**, *23*, 376-381;

[18] V. G. Khomenko, V. Z. Barsukov, J. E. Doninger and I. V. Barsukov, *Journal of Power Sources* **2007**, *165*, 598-608;

[19] M. Alias, O. Crosnier, I. Sandu, G. Jestin, A. Papadimopoulos, F. Le Cras, D. M. Schleich and T. Brousse, *Journal of Power Sources* **2007**, *174*, 900-904;

[20] C. Martin, M. Alias, F. Christien, O. Crosnier, D. Belanger and T. Brousse, *Advanced Materials* **2009**, *21*, 1-7.

[21] J. K. Lee, K. B. Smith, C. M. Hayner and H. H. Kung, *Chemical Communications* **2010**, *46*, 2025-2027;

[22] K. Evanoff, A. Magasinski, J. B. Yang and G. Yushin, *Advanced Energy Materials* **2011**, *1*, 495-498;

[23] X. Zhou, Y.-X. Yin, L.-J. Wan and Y.-G. Guo, *Chemical Communications* **2012**, *48*;

[24] Y. H. Zhu, W. Liu, X. Y. Zhang, J. C. He, J. T. Chen, Y. P. Wang and T. B. Cao, *Langmuir* **2013**, *29*, 744-749

[25] L. Luo, J. Wu, J. Luo, J. Huang and V. P. Dravid, *Sci. Rep.* **2014**, *4*.

[26] W. Wang and P. N. Kumta, *ACS Nano* **2010**, *4*, 2233-2241

[27] S. L. Chou, Y. Zhao, J. Z. Wang, Z. X. Chen, H. K. Liu and S. X. Dou, *Journal of Physical Chemistry C* **2010**, *114*, 15862-15867

[28] K. Evanoff, J. Khan, A. A. Balandin, A. Magasinski, W. J. Ready, T. F. Fuller and G. Yushin, *Advanced Materials* **2012**, *24*, 533-+.

[29] L. Mangolini, E. Thimsen and U. Kortshagen, *Nano Letters* **2005**, *5*, 655-659;

[30] O. Yasar-Inceoglu, T. Lopez, E. Farshihagro and L. Mangolini, *Nanotechnology* **2012**, *23*, 255604.

[31] R. J. Anthony, D. J. Rowe, M. Stein, J. Yang and U. Kortshagen, *Advanced Functional Materials* **2011**, *21*, 4042-4046.

[32] L. Mangolini, D. Jurbergs, E. Rogojina and U. Kortshagen, *physica status solidi (c)* **2006**, *3*, 3975-3978;

[33] X. Li, Y. He and M. T. Swihart, *Langmuir* **2004**, *20*, 4720-4727.

[34] Y. K. Du, P. Yang, Z. G. Mou, N. P. Hua and L. Jiang, *Journal of Applied Polymer Science* **2006**, *99*, 23-26;

[35] M. F. Silva, C. A. da Silva, F. C. Fogo, E. A. G. Pineda and A. A. W. Hechenleitner, *Journal of Thermal Analysis and Calorimetry* **2005**, *79*, 367-370.

[36] M. J. O'Connell, P. Boul, L. M. Ericson, C. Huffman, Y. H. Wang, E. Haroz, C. Kuper, J. Tour, K. D. Ausman and R. E. Smalley, *Chemical Physics Letters* **2001**, *342*, 265-271;

[37] J. B. Gao, A. P. Yu, M. E. Itkis, E. Bekyarova, B. Zhao, S. Niyogi and R. C. Haddon, *Journal of the American Chemical Society* **2004**, *126*, 16698-16699.

[38] H. Richter, Z. P. Wang and L. Ley, *Solid State Communications* **1981**, *39*, 625-629;

[39] V. Paillard, P. Puech, M. A. Laguna, R. Carles, B. Kohn and F. Huisken, *Journal of Applied Physics* **1999**, *86*, 1921-1924;

[40] Z. Iqbal and S. Veprek, *Journal of Physics C-Solid State Physics* **1982**, *15*, 377-392;

[41] C. M. Hessel, J. Wei, D. Reid, H. Fujii, M. C. Downer and B. A. Korgel, *The Journal of Physical Chemistry Letters* **2012**, *3*, 1089-1093.

[42] A. C. Ferrari and J. Robertson, *Physical Review B* **2000**, *61*, 14095-14107;

[43] A. C. Ferrari and J. Robertson, *Physical Review B* **2001**, *64*;

[44] A. C. Ferrari and J. Robertson, *Philosophical Transactions of the Royal Society of London. Series A: Mathematical, Physical and Engineering Sciences* **2004**, *362*, 2477-2512.

[45] W. S. Bacsa, J. S. Lannin, D. L. Pappas and J. J. Cuomo, *Physical Review B* **1993**, *47*, 10931-10934;

[46] F. Li and J. S. Lannin, *Applied Physics Letters* **1992**, *61*, 2116-2118;

[47] C. S. Casari, A. L. Bassi, A. Baserga, L. Ravagnan, P. Piseri, C. Lenardi, M. Tommasini, A. Milani, D. Fazzi, C. E. Bottani and P. Milani, *Physical Review B* **2008**, *77*.

[48] A. C. Ferrari and J. Robertson, *Physical Review B* **2001**, *63*.

[49] Z. Hu, X. Liao, H. Diao, G. Kong, X. Zeng and Y. Xu, *Journal of Crystal Growth* **2004**, *264*, 7-12;

[50] T. Rajagopalan, X. Wang, B. Lahlouh, C. Ramkumar and P. Dutta, *Journal of Applied Physics* **2003**, *94*, 5252-5260.

[51] D. Song, E. C. Cho, Y. H. Cho, G. Conibeer, Y. Huang, S. Huang and M. A. Green, *Thin Solid Films* **2008**, *516*, 3824-3830;

[52] D. Y. Song, E. C. Cho, G. Conibeer, C. Flynn, Y. D. Huang and M. A. Green, *Solar Energy Materials and Solar Cells* **2008**, *92*, 474-481.

[53] M. H. Brodsky and M. Cardona, *Journal of Non-Crystalline Solids* **1978**, *31*, 81-108.

[54] U. Kasavajjula, C. S. Wang and A. J. Appleby, *Journal of Power Sources* **2007**, *163*, 1003-1039;

[55] I. S. Kim, G. E. Blomgren and P. N. Kumta, *Journal of Power Sources* **2004**, *130*, 275-280.

[56] L. Mangolini, and U.Kortshagen, *Advanced Materials* 19.18 **2007**, 2513-2519.

Chapter 4. Si/Sn Nanoparticles Composite as Anode Materials

4.1 Introduction

As described in previous chapters, carbon has been widely used as conductive materials for silicon in literature and our earlier stage studies. Yet, 1) amorphous carbon electric conductivity is not ideal; at the same time the carbon additive lower the overall specific capacity [1-5]. We want to find a conductive material which also presents high lithium specific capacity. In this contribution, we describe a novel and promising approach that may bring materials such as silicon and tin closer to commercial utilization. Tin has good electrical conductivity but a theoretical capacity (994mAh/g) [5] that is lower than that of silicon (3579 mAh/g). We have therefore designed and tested a silicon-tin composite structure which overcomes the limitations of each of these two materials. These metal tin nanoparticles can increase the current density in active materials and ensured electrochemical reaction. The anode was realized by mixing commercially available silicon nanoparticles, tin oxide nanoparticles and polyvynilpyrrolidone (PVP). An ethanol-based slurry was produced and coated onto copper foils via Mayer rod, followed by a single annealing step for reduction and carbonization. The thermal decomposition of PVP leads to the

reduction of tin oxide to metallic tin. SEM and XRD analysis confirm that a uniform mixture of silicon and tin particles embedded into an amorphous carbon matrix is obtained. This electrode exhibits a stable storage capacity exceeding 1000mAh/g with nearly 80% first cycle coulombic efficiency. This performance is superior to that of the control samples produced using silicon nanoparticles alone and tin nanoparticles alone. Delithiation and lithiation peaks for both tin and silicon were observed, confirming that both components contribute to the device performance. Weight loadings as high as 1 mg/cm^2 have been tested with little variation in specific capacities.

4.2 Experiments

Silicon nanoparticles (<100nm), SnO_2 (<100nm) and $SnCl_2.2H_2O$ were obtained from Sigma-Aldrich, and used as received. For SiNPs-SnNPs-aC electrode, the preparation procedure is: 1) The Si NPs and SnO_2 NPs with a weight ratio of 1:1.27 (Si:Sn wt% 1:1) were thoroughly mixed by ball-milled for 24 hours. The mixed power were collected and weighted (typically 150mg) in a small beaker for later use. PVP were weighted (3X weight of Si+SnO_2 particles, typically 450mg) and dispersed in 5ml of ethanol formed a clear and sticky solution. The PVP-ethanol solution was piped into the beaker, which contains thoroughly mixed Si-SnO_2 nanoparticles. The mixture was probe-sonicated for 10mins, later, an uniform, thick and sticky slurry was formed. The slurry was coated on a 4.5*4.5 cm^2 carbon coated copper foil (from MTI) via Mayer rod technique and ethanol

was evaporated in about 5mins. The dried electrode is shown in Figure 4.1, the brownish electrode material coating is very uniform.

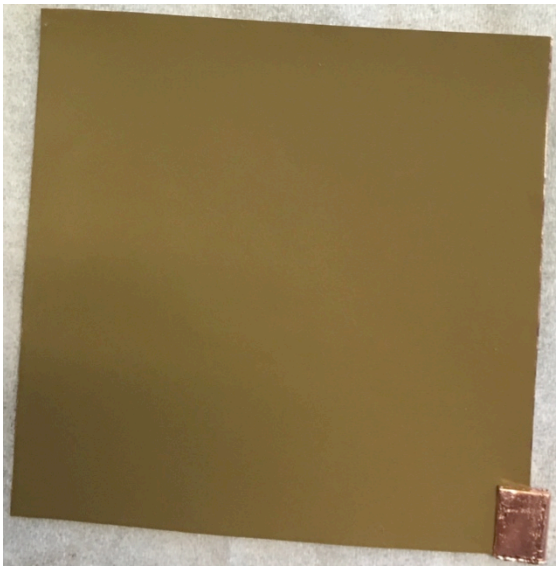

Figure 4.1 As prepared electrode: commercial SiNPs-SnO_2NPs-PVP

2) The Si NPs and $SnCl_2$.2HO powder with a weight ratio of 1:2.08 (Si:Sn wt% 1:1, typically 100mg silicon, 220mg $SnCl_2$.2H2O) were weighted. PVP were weighted (3X weight of Si+Sn particles, typically 600mg) and dispersed in 7.5ml of ethanol formed a clear and sticky solution. The PVP solution was piped into the powers via 10mins probe-sonication to obtain a uniform dispersion. Similar method as 1) was used for coating on copper foil substrate. Preparation of SiNPs-PVP electrode: SnO_2NPs-PVP electrode was prepared by probe sonicating the particles and 3X weight PVP and coated on copper foil via Mayer rod technique.

For the electrochemical test: 1 M Voltammetry in ethylene carbonate/diethyl carbonate (1:1 v/v) is used as the electrolyte (MTI, part number: EQ-Be-LiPF6). 10 wt.% of FEC (Solvay S.A., Belgium) is added to the electrolyte for selected batteries. The separator film is purchased from MTI. All cells are cycled between 0.01 V and 1.5 V using an Arbin potentiostat. Cyclic voltammetry (CV) is performed at a sweeping rate of 0.1 mV/s.

4.2.1 Converting of SnO_2 NPs to SnNPs:

In order to convert SnO_2 NPs to Sn NPs, the electrode was annealed under argon environment for 15mins at 675 °C. The following reactions took placed [6]:

$$SnO_2\ (s) + 2C\ (s) \text{ --- } Sn\ (liquid) + 2CO\ (g),\ \text{at } T=655.8°C$$

The electrode were cool down to room temperature with a cooling rate of 10°C/min. The liquid phase metal tin transform to solid phase at 231.9°C. Since tin were liquid phase before the electrode cool down to 231.9°C, the liquid could have formed into big Sn particles. Yet, we observed from XRD and SEM images (Figure 4.2 and Figure 4.3) metal Sn existing in sphere morphology with an average diameter of only ~30nm. Our explanation is: Liquid metal Sn condensed to solid phase during cooling process. As described in electrode preparation section, PVP were uniformly wrapped around all the particles as coated. Thus after annealing at 675 °C, the carbon residue from PVP degradation [7] were wrapped around the liquid tin and preventing tin from flowing together. Carbon coated copper foil was chose to prevent copper and Sn reaction at the contacting

boundary. The amorphous carbon act as framework for liquid Sn, each “spot” hold a certain amount of liquid Sn. After cooling process, solid SnNPs were homogenously dispersed in amorphous carbon framework.

4.3 Results and Discussion

XRD spectrum indicates the Sn nanoparticle with an average diameter of 30nm calculated via Scheder equation. $D = K\lambda / \beta\cos\theta$. Where: D is the mean size of the nanoparticles; K is a dimensionless shape factor, the value used here is 0.9; λ is the X-ray wavelength (0.154nm); β is half of the maximum intensity. θ is the Bragg angle.

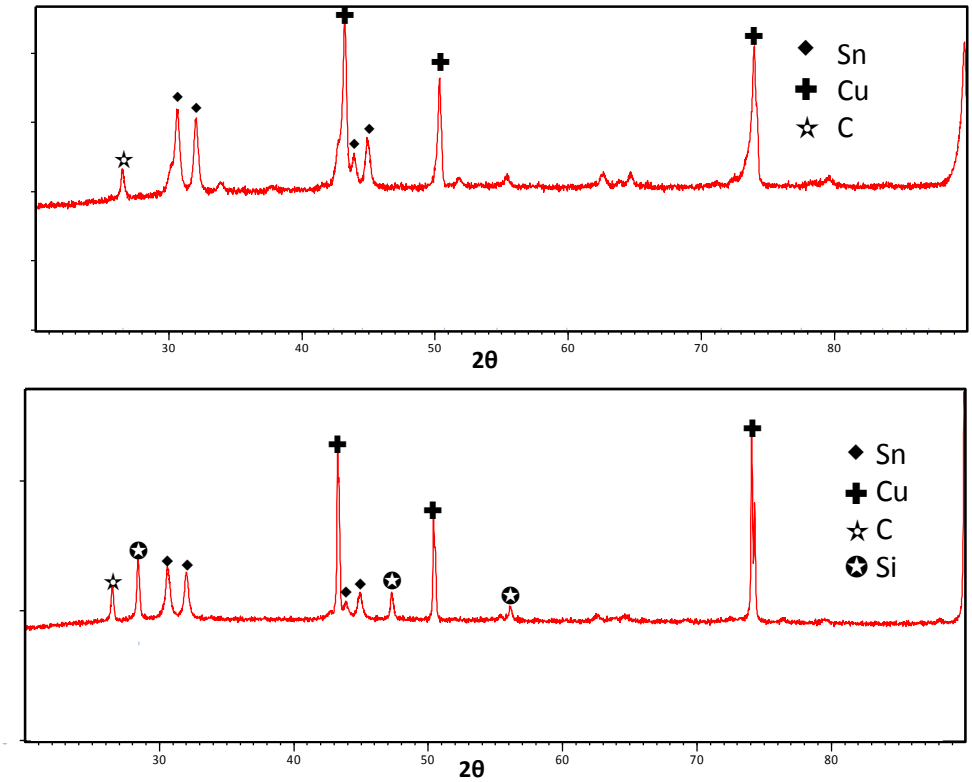

Figure 4.2 (top) XRD spectrum for SnO_2-PVP on carbon coated copper substrate (after annealing); (down) XRD spectrum for SiNPs-SnO_2-PVP on carbon coated copper substrate (after annealing).

After thermal annealing, XRD analysis of SnO_2-PVP on carbon coated copper substrate after annealing at 675°C (see figure 4.2 top) shows peaks due to the metal Sn nanocrystals ([200] at 30.5°, [101] at 32°, [220] at 44°, [211] at 45° and [301] at 56°). The peak assignment is based on the ICSD databse (Inorganic crystal structure database FIZ Karlsruhe). We could resolve contribution from crystalline carbon at 26.5°, which is from the commercial carbon coating on copper foil. Peaks at 43°, 50.5°, 75° are corresponding copper [111], [200], [220] which come from the copper substrate. Analysis of the grain size using Scherrer's formula returns a value of ~30 nm for the tin particle size after annealing. This suggests that the presence of PVP is effective at reducing SnO_2 to Sn. At the same time PVP residue helped with controlling Sn nanoparticles size. Similarly, ~29nm diameter Sn nanoparticles peaks were identified in XRD spectrum of SiNPs-SnO_2-PVP on carbon coated copper substrate after annealing. Beside Sn, copper, carbon, there are peaks at 28°, 47°, 56°, which can be assign to silicon nanoparticles. The XRD analysis indicates that SiNPs-SnO2-PVP anode become SiNPs-SnNPs-aC after annealing at 675°C.

The same conclusion can be made from the SEM images, as shown in Figure 4.3. The zoom in image of SiNPs-SnNPs-aC electrode (inset of top) also indicates uniformly distributed silicon and tin nanoparticles covered by a layer of carbon material (dark gray). SnNPs size is around ~30nm. EDS indicates Si:Sn:C wt% is roughly 1:1:1. Top morphology of SnO_2-PVP after annealing

electrode is shown Figure 4.3 (middle). The brighter dots is SnNPs while the dark gray matrix is amorphous carbon reducing from PVP. We can see that SnNPs are uniform in size and the carbon matrix is separating each of them.

SnNPs embedded in amorphous carbon matrix electrode shown a relatively stable discharge capacity for the first 40 cycles at 0.1C rate. Average discharge capacity is ~510 mAh/g (Sn wt% roughly 70%). The high electrical conductivity (Sn metal: $8.7*10^6$ S·m) and the uniform distribution of tin nanoparticles are the main contribution to the stable battery performance. The low initial coulombic efficiency is may attribute to the large surface area of the amorphous carbon matrix and the SnNPs. In a contrast, SiNPs-PVP electrode barely shows any discharge capacity. First of all, commercial silicon nanoparticles are not as uniform distribution as Sn nanoparticles due to the different formation mechanism. Silicon it self has a very low electrical conductivity of 4.3×10^{-4} S·m. Take the surface insulating SiO_2 oxidation layer into account, the overall conductivity is too low for the electrode to perform normally as depicted in Figure 4.4 (bottom).

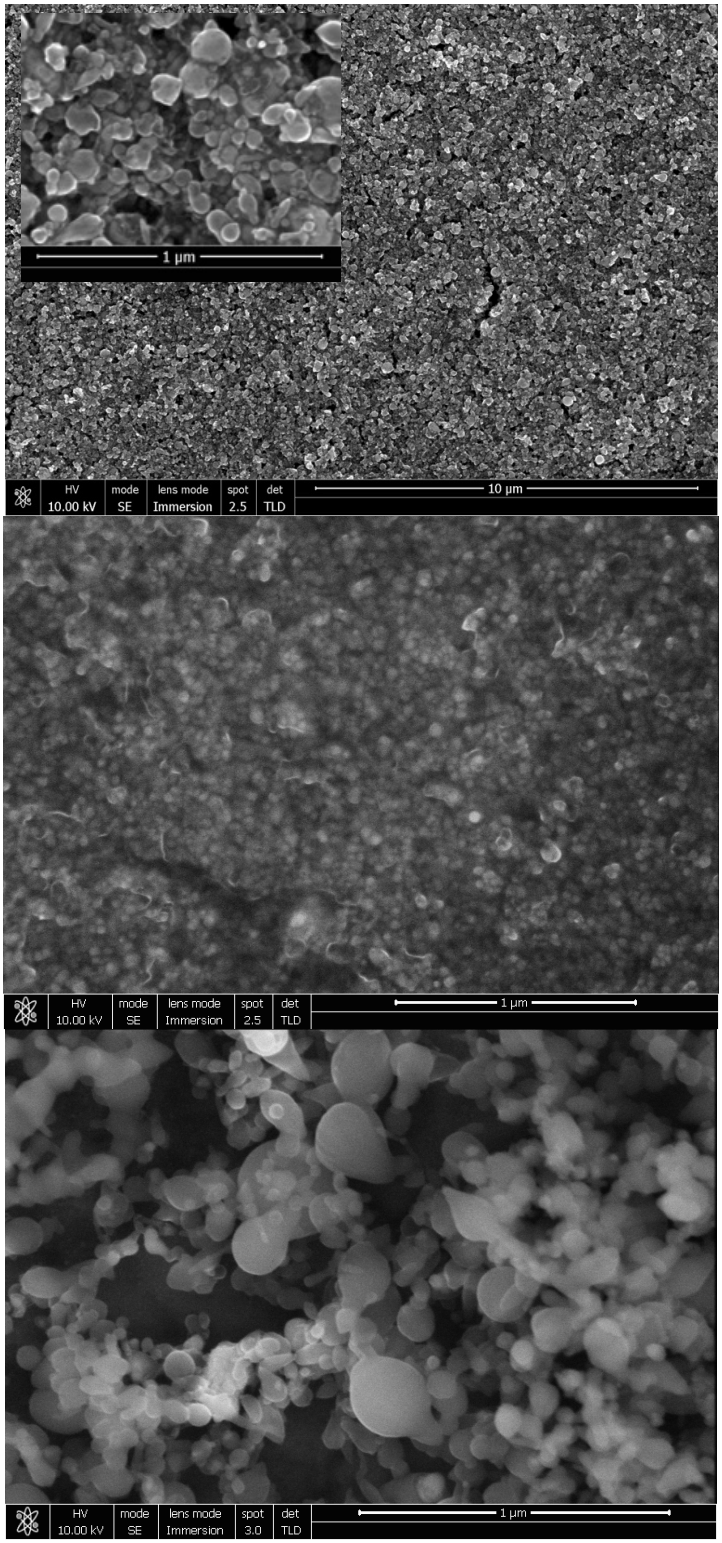

Figure 4.3 (top) SEM image of annealed SiNPs-SnO_2-PVP on copper substrate, inset: zoom-in image of the same electrode. (middle) SEM image of annealed SnO_2-PVP on copper. (Bottom) SEM image of annealed SiNPs-PVP on copper.

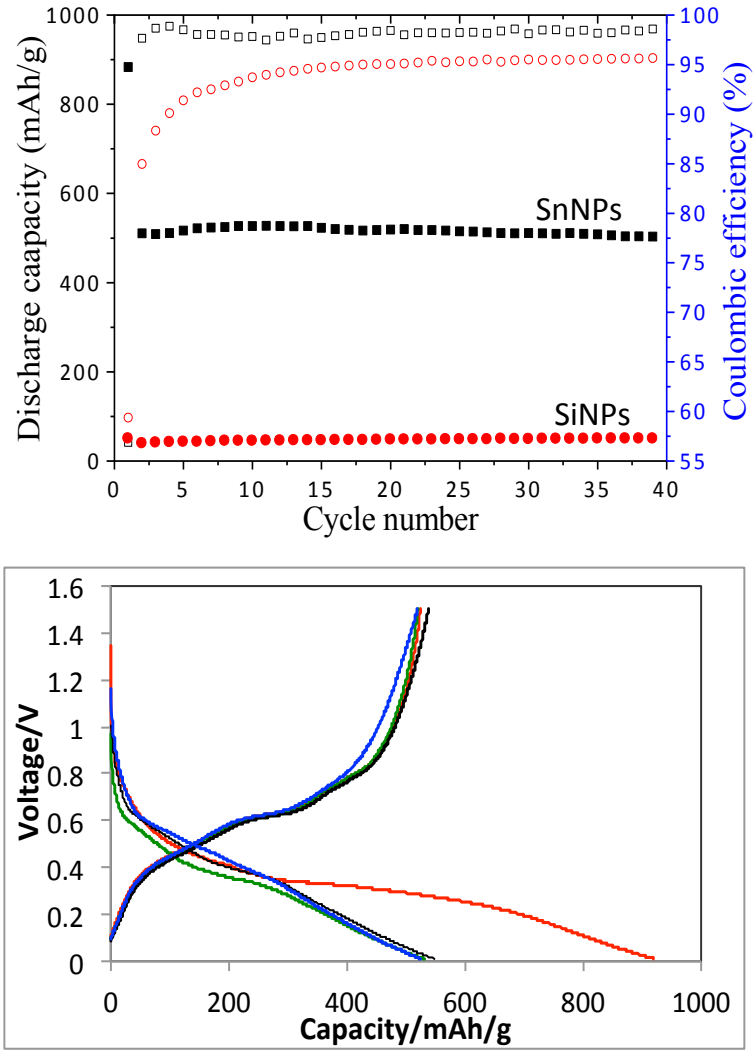

Figure 4.4 (black) Discharge capacity (mAh/g) and coulombic efficiency of SnO_2-PVP electrode over number of cycles; (red) Discharge capacity (mAh/g) and coulombic efficiency of annealed SiNPs-PVP electrode over number of cycles. (red) 1st , (green) 2nd, (blue) 10th, (black) 40th Glavanostatic charge/discharge profile of the SnO_2-PVP annealed electrode.

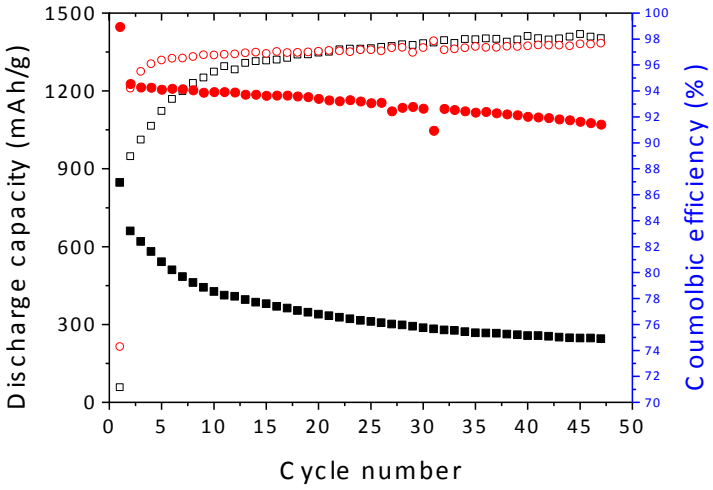

Figure 4.5 Discharge capacity (red dots) and coulombic efficiency (empty red dots) of SiNPs-SnO_2-PVP electrode over number of cycles; Discharge capacity (black dots) and coulombic efficiency (empty black dots) of SiNPs-CB-PVP electrode over number of cycles;

Carbon black helped in improving silicon nanoparticles inter-particle connections to some extend drawn from depiction of Figure 4.5 (black dots). However, the effect of carbon black as conductive materials and framework for silicon nanoparticles is limited. Figure 4.5 (black dots) depicts the fast capacity fading. The cumulative cell inefficiency corresponds to the following two causes: electrochemical sintering which refer to silicon nanoparticles dispersed within carbon black media have agglomerated into dense blocks during cycling; increasing in the SEI thickness. Resulting in decreasing of electrical conductivity and more “dead spot”, where lithium ions cannot be taken out from silicon nanoparticles due to the poor electron conductivity. Simply mixing of carbon black and SiNPs as active materials is not an effective way of obtaining stable galvanostatic cyclability. This is consistent with previous studies in literature [8-10].

The galvanostatic discharge capacity performance of SiNPs-SnNPs-PVP electrode is obviously better from SiNPs-CB-PVP as plotted in Figure 4.5 (red dots). For the former electrode, the first cycle delithiation capacity and coulombic efficiency are 1440mAh/g and 79%, respectively; The later one is 847mAh/g and 71%, respectively. The higher capacity is expected, for metal Sn also has a theoretical capacity of 994mAh/g while the theoretical capacity of carbon black is negligible. For the later cycles, SiNPs-SnNPs-PVP electrode exhibits a smaller discharge capacity fading step (average 2.8mAh/g per cycle) compare with 25mAh/g capacity fading per cycle in SiNPs-CB-PVP electrode. As explained in earlier section, both electrode were prepared in exactly the same conditions except carbon black were used to replace SnNPs with the same volume ratio. The different behaviors of the two above described electrodes are likely due to a combination of the following factors. First, lithium ions insertion in both silicon and tin nanoparticles during lithiation process and both particles experience volume expansion which build closer contacts between each particles and lead to better electron conductivity; Second, it is well know during cycling silicon nanoparticles sintering and agglomerated into dense blocks [10, 11] when silicon is not covered or being put in a stable frame work. In the case of SiNP-SnNPs-PVP electrode, SiNPs-SnNPs are very likely agglomerated in dense blocks together which forms bigger particles with SiNPs and SnNPs inside. This does not necessarily lead to battery failure as long as good conductivity is maintained

between particles. Take the tin nanoparticle's high electrical conductivity into account, the electron conductivity of these newly formed bigger agglomerations are not going to be much lower than the initial particles which allow lithium ions insertion/extraction from silicon nanoparticles inside the agglomeration. These metal tin nanoparticles can increase the current density in active materials and ensured electrochemical reaction. These could be a possibility of why Si-Sn-PVP electrode behaves much better than Si-CB-PVP. One thing worth mention is: the columbic efficiency in later cycles for SiNPs-SnNPs-PVP anode is around 98%. This inefficiency largely corresponds to increases in electrolyte decomposition and subsequent increases in the SEI thickness. Although both SiNPs and SnNPs will expand but not crack, yet SEI can be deformed during delithiation, thus lead to the increases in the SEI thickness. Consequently, SEI resistance increases since the SEI is a good ion conductor but poor electrical conductor.

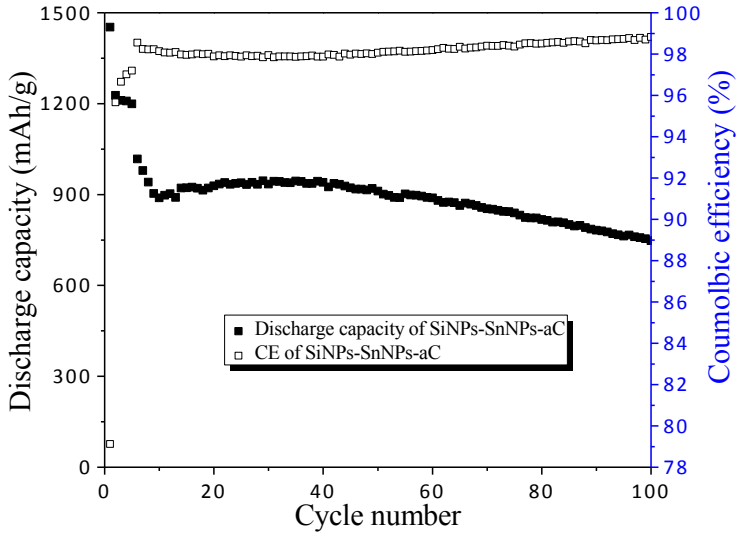

Figure 4.6 Discharge capacity and coulombic efficiency of Si-SnO2-PVP annealed at 775°C; 1.1mg/cm^2, cycled at 0.1C (first 5 cycles), 0.5C for later cycles.

Electrode with higher weight loading (1.1mg/cm^2), higher annealing temperature (775°C) was performed as well. Figure 4.6 depicts the discharge capacity of Si-SnO2-PVP electrode cycled at 0.1C and 0.5C. The discharge capacity is ~1200mAh/g at 0.1C, while this number drop to 850mAh/g when cycled at 0.5C. This that higher weight loading is not going to affect the over all capacity, this is due to the overall high electric conductivity attribution from uniformly distributed SnNPs. The initial coulombic efficiency is 79%. The battery is stabled for about 100 cycles.

Figure 4.7 depicts the results of the cyclic voltammetry measurements from the 1st cycle to the 10th cycle. Delithiation peaks are 0.62 V, 0.37V and 0.18 V; and four oxidation peaks are 0.33V, 0.52V, 0.67V and 0.8V. The lithiation peak at 0.18V and oxidation peaks at 0.33V, 0.52V are corresponding to lithium ions insertion and extraction from silicon nanoparticles, respectively. Lithiation peak at 0.37V and 0.62V is attributed to LixSn formation, while oxidation peaks at 0.67V and 0.8V are delithiation reaction of LixSn alloy [12]. These are consistent with previous studies on silicon-based/tin-based anodes. The CV curve indicates the coexistence of both silicon and Sn nanoparticles. Upon cycling, the coulombic efficiency gets higher. The bottom figure is 1st, 2nd, 10th and 40th Galvanostatic charge/discharge profile, The plateaus are consistent with CV results.

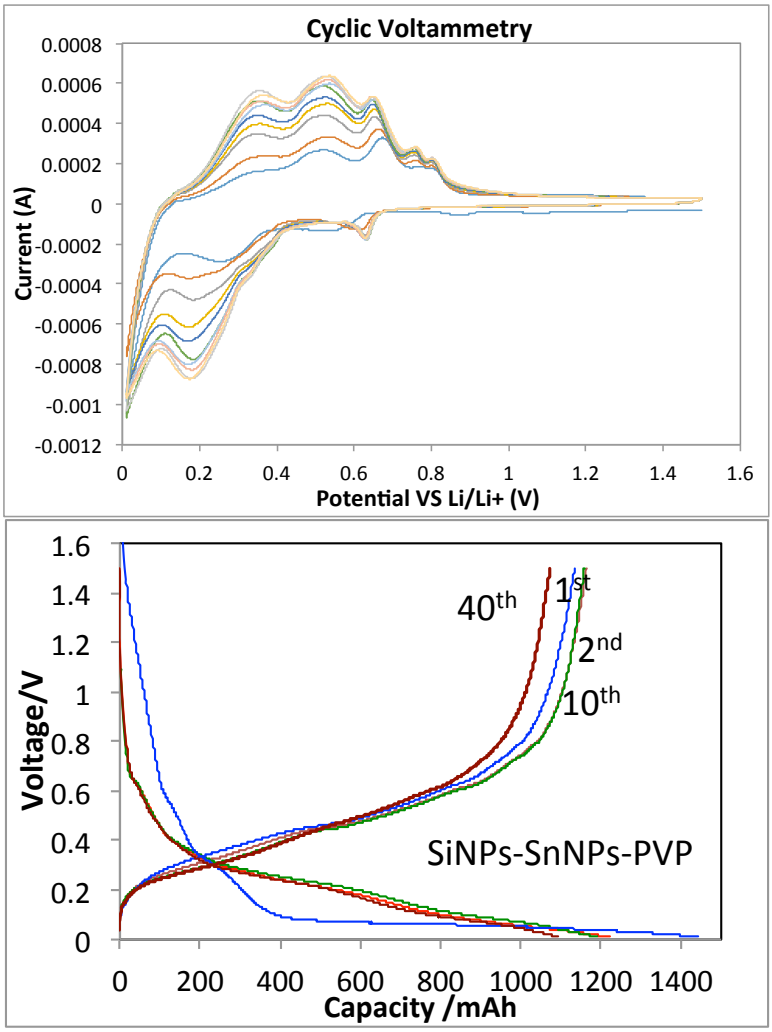

Figure 4.7 (Top) Cyclic Voltammetry of SiNPs-SnNPs-PVP electrode (first 10 cycles), sweep rate: 0.1mV/s. (Bottom) 1st, 2nd, 10th, 40th Galvanostatic charge/discharge profile of the same material electrode.

$SnCl_2.2H_2O$ was also used as tin nanoparticle precursor. SiNPs-$SnCl_2$-PVP annealed at 775 degree C was also tested. SEM images shown in Figure 4.8 described SnNPs were more uniform than SnO_2 reduced SnNPs in SiNPs-SnO_2-PVP system. $SnCl_2.2H_2O$ were solution phase when mixing with SiNPs, thus naturally they disperse better around SiNPs after reducing to SnNPs. All the particles were covered in a layer of amorphous carbon. The galvonstatic

cyclability were performed for SiNPs-$SnCl_2$-PVP. Similar discharge capacity and coulombic efficiency were obtained compare with SiNPs-SnO_2-PVP electrode. After 60 cycles, it more stable than SiNPs-SnO_2-PVP electrode. We attribute it to the more uniformity of SnNPs in the electrode.

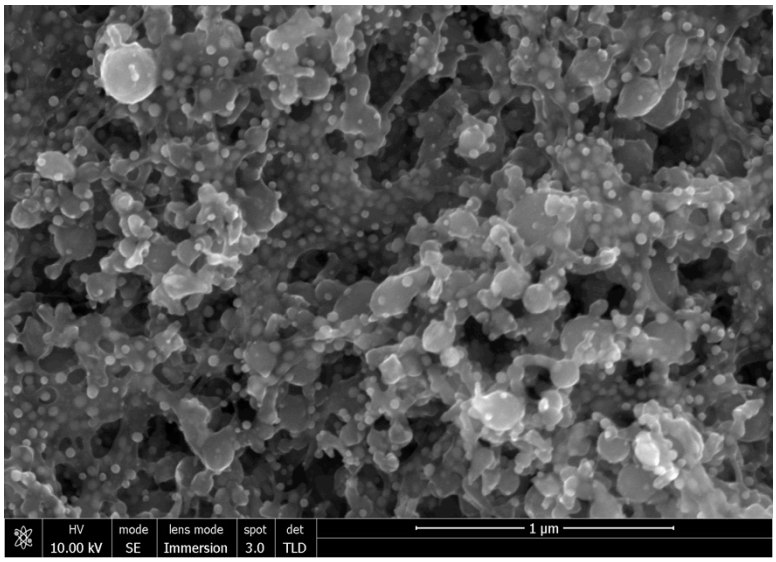

Figure 4.8 SEM image of annealed SiNPs-$SnCl_2$-PVP electrode

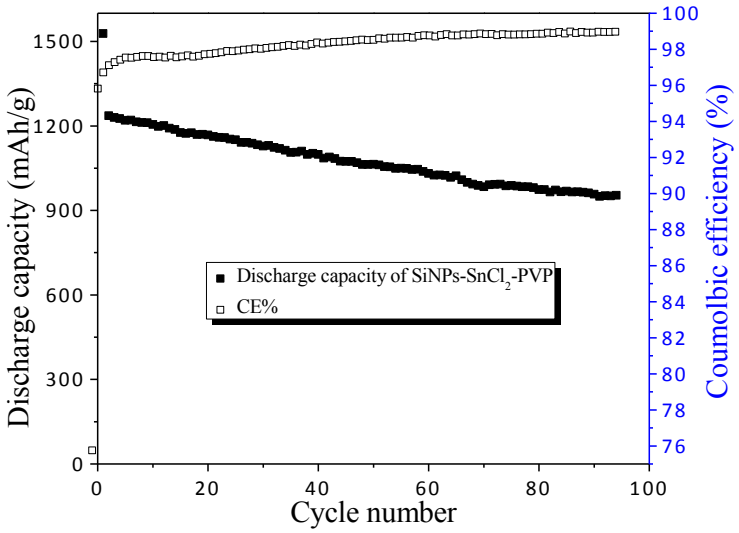

Figure 4.9 Discharge capacity and coulombic efficiency of annealed Si-$SnCl_2$-PVP electrode. C rate: 0.1C

4.4 Conclusion

SiNPs-SnNPs-aC were successfully fabricated. SnNPs are reduction from SnO_2 or $SnCl_2$. The uniform mixture exhibit more stable cycleability and higher specific energy compare with the anode made of SiNPs-CB-aC, SnNPs-aC and SiNP-aC. SnNPs has high electrical conductivity, which can increase the current density in active materials to ensure electrochemical reaction. Upon cycling, both SiNPs and SnNPs expand, yet the conductivity would be keep at a high level which assure the electrode maintain a high (~1100mAh/g at 0.1C) capacity and relatively stable galvonstatic cyclability performance. The result shows that besides carbon materials, conductive materials with high lithium ion specific capacity could be good candidates to use in silicon-based anode. This work also indicates Si/Sn alloy particles may work even better as next generation anode material.

Reference

[1] Liu, Y., K. Hanai, J. Yang, N. Imanishi, A. Hirano, and Y. Takeda, *Silicon/Carbon Composites as Anode Materials for Li-Ion Batteries.* Electrochemical and Solid-State Letters, 2004. **7**(10): p. A369-A372

[2] Shu, J., H. Li, R. Yang, Y. Shi, and X. Huang, *Cage-like carbon nanotubes/Si composite as anode material for lithium ion batteries.* Electrochemistry Communications, 2006. **8**(1): p. 51-54.

[3] Martin, C., M. Alias, F. Christien, O. Crosnier, D. Belanger, and T. Brousse, *Graphite-grafted silicon nanocomposite as a negative electrode for lithium-ion batteris.* Advanced Materials, 2009. **21**: p. 1-7.

[4] Liu, N., Z. Lu, J. Zhao, M.T. McDowell, H.-W. Lee, W. Zhao, and Y. Cui, *A pomegranate-inspired nanoscale design for large-volume-change lithium battery anodes.* Nat Nano, 2014. **9**(3): p. 187-192.

[5] Winter, M. and J.O. Besenhard, *Electrochemical lithiation of tin and tin-based intermetallics and composites.* Electrochimica Acta, 1999. **45**(1–2): p. 31-50.

[6] Mitchell, A. R., & Parker, R. H. (1988). The reduction of SnO 2 and Fe 2 O 3 by solid carbon. *Minerals Engineering*, *1*(1), 53-66.

[7] Zhong, L., Guo, J., & Mangolini, L. (2015). A stable silicon anode based on the uniform dispersion of quantum dots in a polymer matrix. *Journal of Power Sources*, *273*, 638-644.

[8] Yang, X. Q., McBreen, J., Yoon, W. S., Yoshio, M., Wang, H., Fukuda, K., & Umeno, T. (2002). Structural studies of the new carbon-coated silicon anode materials using synchrotron-based in situ XRD. *Electrochemistry communications*, *4*(11), 893-897.

[9] Wen, Z. S., Yang, J., Wang, B. F., Wang, K., & Liu, Y. (2003). High capacity silicon/carbon composite anode materials for lithium ion batteries.*Electrochemistry Communications*, *5*(2), 165-168.

[10] Yoshio, M., Tsumura, T., & Dimov, N. (2005). Electrochemical behaviors of silicon based anode material. *Journal of power sources*, *146*(1), 10-14.

[11] Dimov, N., Fukuda, K., Umeno, T., Kugino, S., & Yoshio, M. (2003). Characterization of carbon-coated silicon: structural evolution and possible limitations. *Journal of power sources*, *114*(1), 88-95.

[12] Xu, Y., Liu, Q., Zhu, Y., Liu, Y., Langrock, A., Zachariah, M. R., & Wang, C. (2013). Uniform nano-Sn/C composite anodes for lithium ion batteries. *Nano letters*, *13*(2), 470-474.

Chapter 5. Conclusions and Future Works

The objective of this doctoral work was to investigate high energy density anode materials for lithium ion batteries that can be used in both portable electronic devices and hybrid/electric vehicles. As the main affective factors, anode and cathode intensively investigated. Among all the possible solutions, it is important to use a non-toxic, scalable and low cost fabrication system. We have devoted our effort on one of the most promising next generation anode materials: silicon, tin based materials. We has been using scalable method to synthesis these materials. The materials synthesis, characterization, electrochemical performance-structure relationship have been investigated. This concluding chapter is going to summarize the findings in this dissertation and discuss the possible future studies.

Chapter 2 demonstrated that spray pyrolysis, which is well-known to be scalable to large production levels, can be used for the direct synthesis of yolk–shell nanoparticles. We have shown that nickel oxide–silicon particles can be produced using off-the-shelf precursors and post-processed via thermal annealing to give an aC-Ni-Si shell–yolk structure. Empty space and conductive outside layer were successfully engineered. The combination of the amorphous carbon layer with the nickel cage greatly enhances the stability of the structure

upon electrochemical cycling. We expect this approach to be applicable to other materials and to be relevant to any material that experiences large volume changes during electrochemical energy storage.

Chapter 3 uncovered the following conclusion: for the first time, silicon quantum dots synthesized using non-thermal plasma CVD have been utilized as anode materials. SiQDs were successfully synthesized using non-thermal PECVD and surface functionalized. These quantum dots, after specific structure engineering, are proven to be a step towards commercialization of silicon-based anode. SiQDs after wrapping by PVP polymer and experiencing agglomeration during annealing process formed a “pomegranate’ structure: PVP reduced amorphous carbon (aC) uniformly wrapped around each SiQDs and these aC wrapped SiQDs agglomerated formed this “pomegranate’ type of structure. With carbon nanotubes as additive, this type of anode materials can achieve a coulombic efficiency of 99.8% and can reach 200 cycles. The step of uniformly wrapping SiQDs with PVP is a simple but critical step for the successful of this structure design. CV, galvostatic performance and SEI studies show that upon cycling (volume expansion/shrinking) the SiQDs-aC pomegranate structures (<5μm) maintain their shape without cracking. In addition with the high CE%, we conclude that silicon quantum dots is not indirect contact with electrolyte, the interior amorphous carbon can conduct Li^+ and e^- in/out of inner SiQDs. The fabrication protocol described in this contribution represents a step towards the

successful commercial utilization of silicon-based nanomaterials for energy storage applications.

Chapter 4 studied the possibility of combining a high electrical conductive active material-tin nanoparticles with silicon nanoparticles. This material also presents a high lithium specific capacity. The synthesized SiNPs-SnNPs-aC uniform mixture exhibit more stable cycleability and higher specific energy compare with the anode made of SiNPs-Carbon Black-aC as show in chapter 4. SnNPs are reduced from SnO_2 or $SnCl_2$. SnNPs has higher electrical conductivity which can increase the current density in active materials to ensure electrochemical reaction, at the same time it's has a high specific capacity. Upon cycling, both SiNPs and SnNPs expand, yet the conductivity would be keep at a high level which assure the electrode maintain a >1000mAh/g capacity and relatively stable performance. The result also indicates Si/Sn particles may work even better as next generation anode material.

Our findings bring silicon containing anode materials closer to commercial utilization, especially the SiQDs-aC structure. We also think that to better utilizing the silicon containing anode materials in lithium ion batteries, combining with new elastic polymer binder [1,2] and additive added electrolyte [3-5] would lead the electrode to the market soon.

The future work can be done in the following aspect:

1) Using spray pyrolysis method to synthesize SiQDs-aC agglomerations
2) In the SiQDs-PVP-CNTs structure, replacing CNTs with a low surface area conductive materials such as carbon black
3) Investigate the mechanism of lithium ion transfer in Si-Sn NPs

References:

[1] Zhao, H., Zhou, X., Park, S. J., Shi, F., Fu, Y., Ling, M & Liu, G. (2014). A polymerized vinylene carbonate anode binder enhances performance of lithium-ion batteries. *Journal of Power Sources*, *263*, 288-295.

[2] Dai, K., Zhao, H., Wang, Z., Song, X., Battaglia, V., & Liu, G. (2014). Toward high specific capacity and high cycling stability of pure tin nanoparticles with conductive polymer binder for sodium ion batteries. *Journal of Power Sources*, *263*, 276-279.

[3] Etacheri, V., O. Haik, Y. Goffer, G.A. Roberts, I.C. Stefan, R. Fasching, and D. Aurbach. *Effect of Fluoroethylene Carbonate (FEC) on the Performance and Surface Chemistry of Si-Nanowire Li-Ion Battery Anodes.* Langmuir, 2012. **28**(1): p. 965-976.

[4] Lin, Y. M., Klavetter, K. C., Abel, P. R., Davy, N. C., Snider, J. L., Heller, A., & Mullins, C. B. (2012). High performance silicon nanoparticle anode in fluoroethylene carbonate-based electrolyte for Li-ion batteries. *Chemical communications*, *48*(58), 7268-7270.

[5] Zhang, B., Metzger, M., Solchenbach, S., Payne, M., Meini, S., Gasteiger, H. A & Lucht, B. L. (2015). Role of 1, 3-Propane Sultone and Vinylene Carbonate in Solid Electrolyte Interface (SEI) Formation and Gas Generation. *The Journal of Physical Chemistry C*.